

https://dspace.org/

Internal oxidation of a nickel-based superalloy TMS-75 at 900 degrees C

Bill, Oleary Moshe

2012-06-29
http://hdl.handle.net/10539/11565

Downloaded from a DSpace repository. https://dspace.org/

INTERNAL OXIDATION OF A NICKEL - BASED SUPERALLOY TMS-75 AT 900^{o}C

OLEARY MOSHE BILL

A dissertation submitted to the Faculty of Science, University of the Witwatersrand, Johannesburg, in fulfillment of the requirements for the degree of Master of Science.

Johannesburg

December, 2011

Declaration

I declare that this dissertation is my own, unaided work, and that all sources that I have used or quoted have been indicated and acknowledged by means of complete references. It is being submitted for the Degree of Master of Science at the University of the Witwatersrand, Johannesburg. It has not been submitted before for any degree or examination at any other University.



---------- (O. M. Bill)

23 December 2011

Abstract

Nickel-base superalloys have a wide range of use as high temperature materials of high mechanical integrity and good oxidation resistance. In most cases where a protective external adherent alumina scale does not develop, internal oxidation is prevalent. A study was undertaken to investigate the internal oxidation of an experimental, single crystal, nickel-based superalloy TMS-75 in air for 100h at 900^{o}C. Transmission electron microscopy (TEM), scanning electron microscopy (SEM) and X-ray diffraction (XRD) were employed to characterize the internal oxidation of this alloy. Internal oxidation was observed in the presence of a non-protective (Ni,Co)O outer scale. Immediately beneath and in contact with this scale was a thin layer of relatively fine grained spinel oxide inner scale. The internal oxidation or reaction zone was located below these two scales. This zone, of around 20 micrometres in thickness, was found to have had lost its original two phase γ-γ′ microstructure, this being replaced with a relatively course grained structure containing facetted precipitates. The precipitates were identified as being hexagonal AlN and rhombohedral α-Al_2O_3. A study was made of the orientation relationships between the different precipitates and matrix. None of the precipitates were found to exhibit an epitaxial relationship with the surrounding matrix material. The zone axes of the matrix and precipitates were typically misaligned from a minimum of 1.5^{o} up to about 5^{o}. The orientation relationships found between the AlN precipitates and the Ni-based solid solution matrix were:

1) $[013]_M$ // $[12\bar{3}0]_P$ with $(200)_M$ // $(0002)_P$ and $(0\bar{3}1)_M$ // $(2\bar{1}\bar{1}0)_P$

2) $[1\bar{1}0]_M$ // $[01\bar{1}0]_P$ with $(220)_M$ // $(\bar{1}012)_P$ within 2^{o}

3) $[011]_M$ // $[01\bar{1}0]_P$ with $(200)_M$ // $(0002)_P$ and $(3\bar{1}1)_M$ // $(\bar{1}010)_P$

while the orientation relationships found between the α-Al_2O_3 precipitates and the Ni-based solid solution matrix were:

1) $[1\bar{1}4]_M$ // $[2\bar{1}\bar{1}2]_P$ with $(1\bar{3}\bar{1})_M$ // $(\bar{1}011)_P$ within 2^{o}

2) $[1\bar{1}\bar{2}]_M$ // $[10\bar{1}\bar{1}]_P$ with $(15\bar{3})_M$ // $(11\bar{2}1)_P$

Dedications

To

My family,

Charmaine

And

In Memory Of My Beloved Brother

Malory Bill

(29-12-1983 to 27-10-2010)

Acknowledgements

I would like to express sincere gratitude to all those who made this work possible, it was through their dedication and guidance that this dissertation became successful. Grateful thanks to my supervisor Prof. K. Pruessner in the School of Physics for her initial supervisory guidance, and subsequently to Prof. M.J. Witcomb and Prof. L.A. Cornish of the DST/NRF Centre of Excellence in Strong Materials as acting co-supervisors for the completion of the research.

Thanks to Prof. D. Billing in the School of Chemistry for his support and help in X-ray diffraction, and Prof. M.J. Witcomb for his support and help in X-ray diffraction (he says it was a fun learning experience for him), transmission electron microscopy and sample preparation. Their help is greatly appreciated. Grateful thanks to Prof. J. Carter and Prof. J.A. Rodriguez for making the School of Physics a worthy ground for studies.

The DST/NRF Centre of Excellence in Strong Materials is acknowledged for rendering the financial support that made this work possible.

The National Institute for Materials Science in Japan is thanked for the provision of the alloy studied. Mintek is acknowledged for allowing us to their scanning electron microscope.

Also acknowledged is the University of Witwatersrand for the opportunity to study at such a prestigious university, and all the friends who made the time at Wits worthwhile through their moral support and Godly encouragements. These are Maxwell, Nkululeko, Maxwell Jingo, Wisdom, Hilary, Basimenye, Oscar, Makhosonke, Emily and Emmanuel, to name but a few.

Table of Contents

Declaration i
Abstract ii
Dedications iii
Acknowledgements iv
List of Figures v
List of Tables vi

CHAPTER 1 INTRODUCTION 1
1.1 Motivation 1
1.2 Outline of dissertation 3

CHAPTER 2 GENERAL BACKGROUND TO NICKEL-BASED ALLOY OXIDATION 4
2.1 Microstructure and composition of Ni-based superalloys 4
2.2 Alloy oxidation 6
2.3 Thermodynamics of oxidation 7
2.4 Kinetics of oxidation 9
2.5 General concepts of alloy oxidation 11
2.6 Oxidation in Ni-based alloys 14
2.6.1 Ni-Cr-Al alloys 16
2.6.2 Ni_3Al intermetallic compound 17
2.6.3 β-NiAl alloys 18
2.7 Oxidation in Ni-based superalloys 19
2.8 NiO and $NiAl_2O_4$ 22

CHAPTER 3 INTERNAL OXIDATION IN NICKEL-BASED SUPERALLOYS 23
3.1 Progression of internal oxidation 23
3.2 Variation of alloy composition with depth of internal oxidation 27

3.3 Internal oxide development and phase changes 28

CHAPTER 4 INSTRUMENTATION AND METHODS 30
4.1 The Scanning Electron Microscope (SEM) 30
4.2 The Transmission Electron Microscope (TEM) 32
4.3 Ion milling 35
4.4 Energy Dispersive X-ray Analysis (EDX) 37
4.5 X-Ray Diffraction (XRD) 38

CHAPTER 5 EXPERIMENTAL PROCEDURE 42
5.1 The material 42
5.2 Sample preparation for oxidation 42
5.2.1 Sectioning 42
5.2.2 Mechanical polishing 43
5.2.3 Sample oxidation 44
5.3.1 Sample preparation for transmission electron microscopy 44
5.3.2 Sample dimpling 45
5.3.3 Ion milling 47
5.4 Scanning electron microscopy 47
5.5 Transmission electron microscopy 47
5.6 X-ray diffraction 49

CHAPTER 6 RESULTS AND DISCUSSION 50
6.1 X-ray diffraction 50
6.2 TEM imaging and electron diffraction analyses 55
6.3 Overview of the XRD and TEM results 81

CHAPTER 7 CONCLUSIONS 86
POSSIBLE FUTURE WORK 87
REFERENCES 88

APPENDICES 97
Appendix A: Conference abstract published during the course of this project 97

Appendix B: Formulae for calculation of *d* spacings of the different structures [112]..... 100
Appendix C: Formulae for calculation of the angle ϕ between the plane ($h_1k_1l_1$), of spacings d_1 and the plane ($h_2k_2l_2$), of spacing d_2 for the different structures, as well as the zone axis formula [112] 101
Appendix D: Simulated diffraction patterns from the WebEMAPS software package [90] 102

List of Figures

2.1: Typical microstructure of a nickel-based superalloy [5] 5
2.2: Ellingham diagram of oxides plotted against partial pressure [12] 7
2.3: Schematic cross-section of an M-Al alloy concentrated in Al showing an an external layer of Al_2O_3. Modified from [9,10]. 12
2.4: Schematic cross-section of an M-Al dilute in Al showing internal oxidation of Al under an external layer of M_xO_y. Modified from [9,10] 13
2.5: Subgroup/supergroup symmetry relations between the $Fd\bar{3}m$ and C2/*m* space groups for the γ-$Al_2O_3 \rightarrow \theta$-$Al_2O_3$ transformations. Modified from [23] 14
2.6: Oxide map for ternary Ni-Cr-Al alloys at 1000°C [47] 16
2.7: Sequence of events during oxidation of nickel-based CMSX-4 single crystal superalloys at 900°C for 100h as proposed by Akhtar *et al*. [15] 20
2.8: Schematic model for scale and subscale growth on a single crystal Ni-based superalloy (with 6.3 wt. % Al, 6.0 wt. % Cr, some Co, Ti, Mo, W and Ta) at (a) 800°C and (b) 900°C [14] 21
3.1: Schematic view of a corroded sample: I, actual scale/gas interface; II, original alloy/gas interface; III, actual alloy/scale interface; IV, internal oxide precipitation front; (a) external scale (oxide AO); (b) internal oxide region; X, thickness of alloy consumed; ξ, position of the internal oxide front measured from the original alloy surface; (ξ-X), actual thickness of the internal oxide region [61] 23
3.2: Schematic view of advancement of an oxidation front during internal oxidation of a Ni-Ni_3Al alloy [64] 25
3.3: Schematic representation of internal-precipitate formation zones and concentration profiles in a Ni-Cr-Al alloy system [63] 28
4.1: Schematic diagram of a SEM [72] 30
4.2: Schematic diagram of the interaction of the electron beam with the specimen. The zones of the secondary and backscattered electron emission are shown with the primary excitation volume [73] 31
4.3: Comparison of backscattered electron and secondary electron coefficients as a function of atomic number for an accelerating voltage of 30 keV from the data of Wittry [74] and Heinrich [75]. Figure adopted from [76] 32
4.4: Ray diagram for a transmission electron microscope in (a) bright field imaging

mode and (b) selected area electron diffraction mode [77] 33
4.5: The Bragg equation. P, Q and R, are three successive parallel lattice planes (*hkl*) in a crystal. The incoming radiation of wavelength λ is incident on the planes of spacing d_{hkl} at an angle θ and is reflected by the planes at an angle θ. The path difference between the rays reflected by planes P and Q is λ, which by geometry is equal to $2d \sin\theta$ [78] 34
4.6: The TEM considered as a simple electron diffraction camera [79] 35
4.7: A schematic diagram of an ion beam TEM sample thinning device: Argon bleeds into an ionization chamber (ion gun) where a potential typically 2 - 6 keV creates an Ar ion beam incident onto an inclined rotating specimen [73] 36
4.8: Light micrographs of the TEM sample prepared from dimpling followed by ion milling to achieve a small hole and electron transparent regions around it (a) reflected light and (b) transmitted light [84] 36
4.9: Schematic diagram of the generation of a characteristic X-ray. (A) shows an impinging electron removing a sample electron from the innermost shell orbit (K-shell), and (B) shows the vacancy being filled by an electron from the next outer shell (L-shell) with the subsequent generation of an X-ray. The resultant X-ray would be a K_α X-ray [76] 37
4.10: Schematic diagram of the spectrum of X-rays that may be generated from a single element. Since each element actually compromises several energy levels, transitions are thus more numerous (and the nomenclature more complicated) than shown here [76] 38
4.11: Schematic diagram of some typical components and angles of the goniometer for a θ-2θ X-ray diffractometer. The flat specimen is at the centre of the goniometer circle, whose radius is typically 0.25 – 0.5 m [85] 39
4.12: Geometry of a Bragg-Brentano diffractometer. The two angles at the specimen are the same 180° - 2θ [85] 40
4.13: Schematic diagram showing Glancing Incidence X-ray Diffraction for surface films [86] 41
5.1: SEM electron backscattered image of a TMS-75 surface polished down to 0.25 mm prior to oxidation 43
5.2: Schematic diagram of the glued oxidized sample 44
5.3: Embedding of the sample into brass tubing. The two oxidized surfaces were glued and ground to fit into the 600 μm groove of the inner rod [88] 45

5.4: (a) Cutting of the sample embedded in the brass rod and tubing into thin discs (b) planar view of an embedded sample in a brass disc ready to be dimpled [88] 45
5.5: Sample dimpling in which both the dimple plate or wheel and the sample holder rotate [89] 46
5.6: Electron diffraction pattern from an aluminum thin foil showing the (600) ring G, the outer of the doublet, used as a standard to calculate for camera constant λL 48
6.1: Bragg-Brentano XRD diffraction pattern obtained from an unoxidized single crystal TMS-75 surface revealing a preferred (200) orientation which is identical to (001) orientation for a fcc structure..... 51
6.2: Bragg-Brentano XRD diffraction pattern obtained from the sample after oxidation in air for 100 h at 900°C 52
6.3: Comparison of the diffraction patterns observed from (a) the unoxidized TMS-75 alloy surface, (b) oxidized TMS-75 surface using GIXRD, and (c) the oxidized TMS-75 surface using Bragg-Brentano diffractometry 53
6.4: GIXRD diffractograms recorded after each nominal 6 μm depth of material had been removed by polishing from the TMS-75 alloy, previously oxidized for 100 h at 900°C, "a" was the first analysis on the as oxidized, unpolished surface 54
6.5: Expanded GIXRD diffractograms recorded after each nominal 6 μm depth of material has been removed by polishing from the TMS-75 alloy, previously oxidized for 100 h at 900°C, "a" was the first analysis on the as oxidized, unpolished surface 54
6.6: Cross-sectional bright field TEM image of the fine structure zone showing small oxide precipitate S and grains in the TMS-75 superalloy after 100 h oxidation in air at 900°C 55
6.7: EDX spectrum of the topmost region of the fine structure zone shown in Figure 6.6..... 56
6.8: Cross-sectional bright field TEM image of the relatively coarse grained region with precipitates below the area shown in Figure 6.6, of the TMS-75 superalloy after 100 h oxidation in air at 900°C..... 57
6.9: A typical EDX spectrum collected from the region shown in Figure 6.8 57

6.10: Cross-sectional bright field TEM image of the internal reaction zone revealing precipitates A and B in the TMS-75 superalloy after 100 h oxidation in air at 900°C 59
6.11: EDX spectrum from precipitate A in Figure 6.10 60
6.12: Electron diffraction patterns of (a) matrix and (b) precipitate A in Figure 6.10 60
6.13: Indexed diffraction pattern of (a) matrix [013] (compare with simulation Appendix D: Figure D1) and (b) precipitate A $[12\bar{3}0]$ (compare with simulation Appendix D: Figure D5) shown in Figure 6.10 61
6.14: EDX spectrum of precipitate B in Figure 6.10 62
6.15: Cross-sectional bright field TEM image of a plate-shaped precipitate labelled Z in the internal oxidation zone of the TMS-75 superalloy after 100 h oxidation in air at 900°C 63
6.16: EDX spectrum of a plate-shaped precipitate Z in Figure 6.15 63
6.17: Electron diffraction patterns of (a) matrix (b) precipitate Z in Figure 6.15 64
6.18: Indexed diffraction pattern of (a) matrix $[1\bar{1}0]$ (compare with simulation Appendix D: Figure D2) and (b) precipitate Z $[01\bar{1}0]$ (compare with simulation Appendix D: Figure D6) shown in Figure 6.15 65
6.19: Combined diffraction pattern from the matrix and precipitate Z taken at the precipitate zone axis $[01\bar{1}0]$ 65
6.20: Cross-sectional bright field TEM of precipitate C and a plate-shaped precipitate S in the internal oxidation zone of the TMS-75 superalloy after 100 h oxidation in air at 900°C 66
6.21: EDX spectrum from the portion remaining of precipitate C in Figure 6.20 67
6.22: Cross-sectional bright field TEM image of a plate-shaped precipitate (Q), plate-shaped precipitate (R) and a precipitate (P) in the internal oxidation zone of the TMS-75 superalloy after 100 h oxidation in air at 900°C 68
6.23: EDX spectrum obtained from a plate-shaped precipitate S in Figure 6.19. This is identical to the EDX spectrum obtained from plate-shaped precipitate R in Figure 6.22 68
6.24: Electron diffraction patterns of (a) matrix (b) precipitate R in Figure 6.22 69
6.25: Indexed diffraction pattern of (a) matrix [013] (compare with simulation Appendix D: Figure D1) and (b) precipitate R $[12\bar{3}0]$ (compare with

simulation Appendix D: Figure D5) shown in Figure 6.24 70
6.26: EDX spectrum from the part remaining of precipitate P in Figure 6.22 71
6.27: EDX spectrum of the precipitate Q shown in Figure 6.22 72
6.28: Electron diffraction patterns of (a) the matrix (b) precipitate Q in Figure 6.22 72
6.29: Indexed diffraction pattern of (a) matrix [$1\bar{1}0$] (compare with simulation Appendix D: Figure D4) and (b) precipitate Q [$01\bar{1}0$] (compare with simulation Appendix D: Figure D6) shown in Figure 6.22 73
6.30: Combined diffraction pattern from the matrix and precipitate Q at the precipitate zone axis [$01\bar{1}0$] 73
6.31: Cross-sectional bright field TEM image of precipitates C, D and E in the internal oxidation zone of the TMS-75 superalloy after 100 h oxidation in air at 900°C 75
6.32: EDX spectrum of precipitate D in Figure 6.31. The spectrum of precipitate precipitate E was identical to the above 75
6.33: Electron diffraction patterns of (a) matrix (b) precipitate D in Figure 6.31 76
6.34: Indexed diffraction pattern of (a) matrix [$\bar{1}1\bar{4}$] (compare with simulation Appendix D: Figure D4) and (b) precipitate D [$2\bar{1}\bar{1}2$] (compare with simulation Appendix D: Figure D7) shown in Figure 6.31 77
6.35: Electron diffraction patterns of (a) matrix and (b) precipitate E in Figure 6.31 78
6.36: Indexed diffraction patterns of (a) matrix [$1\bar{1}2$] (compare with simulation Appendix D: Figure D5) and (b) precipitate E [$10\bar{1}\bar{1}$] (compare with simulation Appendix D: Figure D8) shown in Figure 6.31 79
6.37: Bright field TEM micrograph showing the two phases: the γ′ phase labelled A, and the γ phase labelled B in the TMS-75 superalloy matrix after 100 h oxidation in air at 900°C 80
6.38: EDX spectrum from the γ-γ′ region in Figure 6.37 80
6.39: Schematic diagram of the oxidation zones 81

Figures in Appendix D

D1: Ni - solid solution and Ni - based solid solution (face centred cubic) [013] 101
D2: Ni - solid solution and Ni - based solid solution (face centred cubic) [$1\bar{1}0$] 101

D3: Ni - solid solution and Ni - based solid solution (face centred cubic) [$1\bar{1}4$] 102

D4: Ni - solid solution and Ni - based solid solution (face centred cubic) [$1\bar{1}\bar{2}$] 102

D5: AlN (hexagonal) [$12\bar{3}0$] 103

D6: AlN (hexagonal) [$01\bar{1}0$] 103

D7: α-Al_2O_3 (rhombohedral) [$2\bar{1}\bar{1}2$] 104

D8: α-Al_2O_3 (rhombohedral) [$10\bar{1}\bar{1}$] 104

List of Tables

3.1: Values for Δ_f H°, Δ_f G° and S° for Al_2O_3, Cr_2O_3 and AlN as compounds in Ni-Cr-Al alloy oxidation and nitridation [9] 28

5.1: Compositions in at. % of the experimental alloy TMS-75 and for comparison close composition commercial alloys CMSX-2, CMSX-4 and CMSX-10 42

6.1: Values of spacing R, d_{hkl}, *hkl* and θ for the matrix pattern shown in Figure 6.12(a) 60

6.2: Values of spacing R, d_{hkl}, *hkl* and θ for the precipitate A pattern shown in Figure 6.12(b) 61

6.3: Values of spacing R, d_{hkl}, *hkl* and θ for the matrix pattern shown in Figure 6.17(a) 64

6.4: Values of spacing R, d_{hkl}, *hkl* and θ for the precipitate Z pattern shown in Figure 6.17(b) 64

6.5: Values of spacing R d_{hkl}, *hkl* and θ for the matrix pattern shown in Figure 6.24(a) 69

6.6: Values of spacing R, $d_{hkl,}$ *hkl* and θ for the precipitate R pattern shown in Figure 6.24(b) 69

6.7: Values of spacing R, d_{hkl}, *hkl* and θ for the matrix pattern shown in Figure 6.28(a) 72

6.8: Values of spacing R, d_{hkl}, *hkl* and θ for the precipitate Q pattern shown in Figure 6.28(b) 73

6.9: Values of spacing R, d_{hkl}, *hkl* and θ for the matrix pattern shown in Figure 6.33(a) 76

6.10: Values of spacing R, d_{hkl}, *hkl* and θ for the precipitate D pattern shown in Figure 6.33(b) 76

6.11: Values of spacing R, d_{hkl}, *hkl* and θ for the matrix pattern shown in Figure 6.35(a) 78

6.12: Values of spacing R, d_{hkl}, *hkl* and θ for the precipitate E pattern shown in Figure 6.35(b) 78

CHAPTER 1

Introduction

1.1 Motivation

The major attribute of high temperature materials is the ability to withstand extreme conditions for long periods under load. To achieve materials with such attributes, group VIIIB elements are commonly incorporated into a Ni-matrix to form Ni-base superalloys. To-date, Ni-base superalloys (NBSAs) have been significantly the most useful and popular materials in high temperature applications such as jet engines and high temperature gas turbines, due to their high mechanical strength and environmental stability [1].

Development and compositional modifications in Ni-base superalloys are often due to the need to increase operating temperature so that greater efficiencies can be achieved. These targeted higher efficiencies have an advantage of cutting down on the cost of operation and CO_2 emission in gas turbines and jet engines. In such quests, composition is modified such the melting point of the material is raised to sustain temperatures at which the targeted efficiencies are realized. Compositional variations to achieve materials with desired properties for particular applications preferentially lead to the choice of elements that aid or improve the desired property to the alloy over those that do not [2]. In high temperature applications of NBSAs, modifications have often been made to simultaneously enhance the mechanical strength and increase the melting points of these alloys. Such attributes require the use of refractory elements, such as Ta, W, and Re, which are the minority of the composition of NBSAs. Equally important to mechanical strength in high temperature operations of NBSAs is also the need for the alloys to be environmentally stable and resistant to oxidation. This makes oxidation studies in high temperature alloys very fundamental and crucial.

Oxidation studies for most NBSAs show that these alloys oxidize in a manner such that they are borderline alumina formers [3, 4]. Borderline alumina formers have limited resistance to environmental degradation due to their failure to develop a completely protective scale. Such an effect is considered to be a result of reduced levels of elements necessary for the formation of protective scales, which are intentionally lowered to accommodate the increased levels of refractory elements required for the modification of mechanical properties. Limited environmental stabilities of borderline alumina formers have in the past been addressed by the use of aluminide coatings which act as alternative sources for scale forming elements thereby

promoting formation of protective scales. However, the use of coatings is complex. Coatings themselves suffer from failure. Also limiting the use of coatings are the additional weight constraints that coatings present in addition to NBSAs' component weight; weight is already an issue and component weight has to be kept minimal. Coating failure is usually caused by buildup of stresses in one part of the coating called the thermal grown oxide (TGO). Coatings commonly fail through spallation [1].

Hence current NBSAs are commonly used in high temperature applications without coatings, despite the fact that these alloys are borderline alumina formers. The propensity of borderline alumina forming alloys to undergo internal oxidation is high; hence this has inspired much research into investigating the internal oxidation behaviour of these alloys. With recent alloy modifications and developments not resolving the issue of borderline alumina forming NBSAs, these alloys still remain highly prone to internal oxidation. Internal oxidation is also promoted by lower oxidation temperatures where transient scales fail to prevent oxygen access into the alloy matrix. In such cases oxide precipitates are formed within the alloy matrix, and these still remain less reviewed experimentally.

It is important to mention that though internal oxidation is common in commercial NBSAs with up to 17 components in high temperature applications, the little work that has been done so far to fully understand internal oxidation is mostly limited to simple binary alloy systems. Considering internal oxidation varies with a number of factors and different alloys systems oxidize differently, it may be considered that the binary alloy systems studied so far may not give an accurate representation of what happens in multi-component NBSAs. There is also a lack of detailed work on the progression and development of internal oxides in NBSAs.

Hence, given that NBSAs are prone to internal oxidation and the current limited knowledge in this area in high temperature alloys, this current study seeks to investigate and identify experimentally the oxide phases precipitated internally in NBSAs. In this study investigations were carried out on an experimental third generation Ni-base superalloy, TMS-75 that was developed at NIMS, Japan.

Thus, in this study, it was attempted to identify the structures and orientations of internally developed oxides and to investigate the variations in oxide development with depth. Carrying out such investigations was done through the use of experimental techniques such as transmission electron microscopy (TEM) and X-ray diffraction (XRD) in combination with reference made to work carried out in model alloys.

1.2 Outline of dissertation

Chapter 2 presents the basic concepts involved in alloy oxidation on external and internal oxidation. Simulation work on internal oxidation of the alloy system under study and other related alloys is presented in the third chapter. A review on the instrumentation and methods used is presented in the fourth chapter. The fifth chapter is dedicated to the experimental procedure of the current work. The results obtained from XRD and TEM are presented in the sixth chapter while the seventh chapter is devoted to in-depth discussion and conclusions. Recommendations for future work are also presented in this last chapter.

CHAPTER 2

General background to nickel-based alloy oxidation

This chapter gives an overview of the theoretical background for this study. The first section outlines the general compositional aspects of NBSAs. The second section then gives an overview of the principles that govern alloy oxidation and also outlines different forms of oxidation. The third section discusses the dependence of alloy oxidation on different parameters, such as composition and temperature. Composition in combination with various environmental parameters determines the oxides that develop and how they develop. The process of internal oxidation, that is, the variation of oxide development with depth, oxide growth and nucleation is discussed.

2.1 Microstructure and composition of Ni-based superalloys

The ordered Ni_3Al phase embedded in the disordered austenitic matrix, Ni-solid solution gives NBSAs their two phase microstructure. Superior performance in mechanical strength and ability to withstand higher thermal and mechanical loads in NBSAs is due to the interactions between the two phases. A typical microstructure of a nickel-based superalloy is shown in Figure 2.1.

The two phases: γ and γ' are coherent since they both have face-centered cubic (fcc) structures, and very similar lattice parameters [1, 2, 5, 6, 7, 8]. Variations in coherence and lattice parameters causing lattice distortions in the two phase microstructure can be introduced through compositional modifications. This lattice misfit between the two phases contributes to hindering propagation of dislocations through two-phased alloys resulting in a strengthening mechanism called *precipitate hardening*.

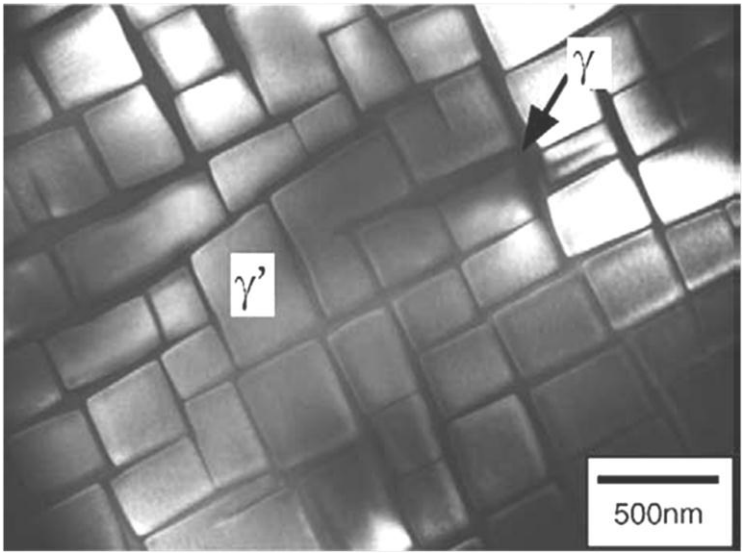


Figure 2.1: Typical microstructure of a nickel-based superalloy [5].

The substantial solubility of Ni for other alloying elements is due to the element's incompletely filled 3d electron shell enables Ni solid solutions to form [1], the solute elements being mainly Al, Co, Ta, W, Mo and Ti. It is reported that the atomic size difference between the alloying element in a solid solution with the Ni matrix results in another type of strengthening known as solid solution strengthening [1, 6, 7]. Solid solution strengthening is known to be greatly enhanced by the presence of elements with a slightly different atomic radius thereby causing lattice distortion. Changes in lattice distortions resulting from the inclusion of different elements in the Ni matrix have been reported by Wang *et al.* [6] showing that mechanical strength in NBSAs is strongly composition dependent.

A local increase in the elastic modulus of the lattice also takes place as the electron from the alloying element is taken up by the third electron of the Ni atom to gain stability [7]. This explains why solid solution does not cause phase instabilities in NBSAs [1].

The variation of strength of the disordered phase γ′ with temperature can be accounted for by the change in lattice parameter [8]. In general, the mechanical strength of NBSAs depends on both the composition and temperature of the alloys.

Studies indicate that consideration of environmental stability or oxidation resistance in addition to mechanical strength as a selection criterion for materials for high temperature applications is also critically important [3, 4].

2.2 Alloy oxidation

Oxidation is a thermodynamic process in which oxygen combines with the metal or alloy under a combined influence of temperature, different environments (ambient conditions, stress conditions) with and without pressure, and microstructural factors. A study of oxidation behaviour in various alloy systems can be undertaken in a number of ways. The options to evaluate the oxidation behaviour are to study the growth kinetics, oxide morphologies and oxide adhesion behaviours with respect to elemental composition, temperature and oxidant pressure. However, in every oxidizing environment the kinetics and the thermodynamics of the oxidation process are very fundamental. All oxidation reactions in alloys gradually result in the development of one or more non-metallic compounds called oxide, which can either be external or internal [9, 10, 11].

The driving force for the oxide formation is a change in the Gibbs free energy of formation. Oxides with lower Gibbs energy of formation are more likely to develop earlier than those with higher energy of formation provided ambient pressure is above their dissociation pressure [9, 10]. Dissociation pressure of any oxide is also a function its Gibbs energy of formation. Oxides with more negative Gibbs energy of formation show greater stabilities. However, an oxide will only form in an oxidation reaction and remain viable if the ambient pressure is in equilibrium or greater than the oxide's dissociation pressure [10, 12]. The Gibbs energies of formation for various oxides can be obtained from the Ellingham Diagram, illustrated in Figure 2.2 [12].

The change in Gibbs energy of formation and oxidant pressure can be favourable for a number of different metal oxidation reactions such that many oxides will develop as in the case with most multicomponent alloys. Different from the simple binary alloy oxidation where only two components are involved and limited reactivities exist, multicomponent alloy oxidation is complicated by the range of reactivities exhibited by the different alloy components. This also implies that a wide range of oxides can be formed upon alloy oxidation, as observed in oxidation products of multicomponent alloys [13, 14, 15].

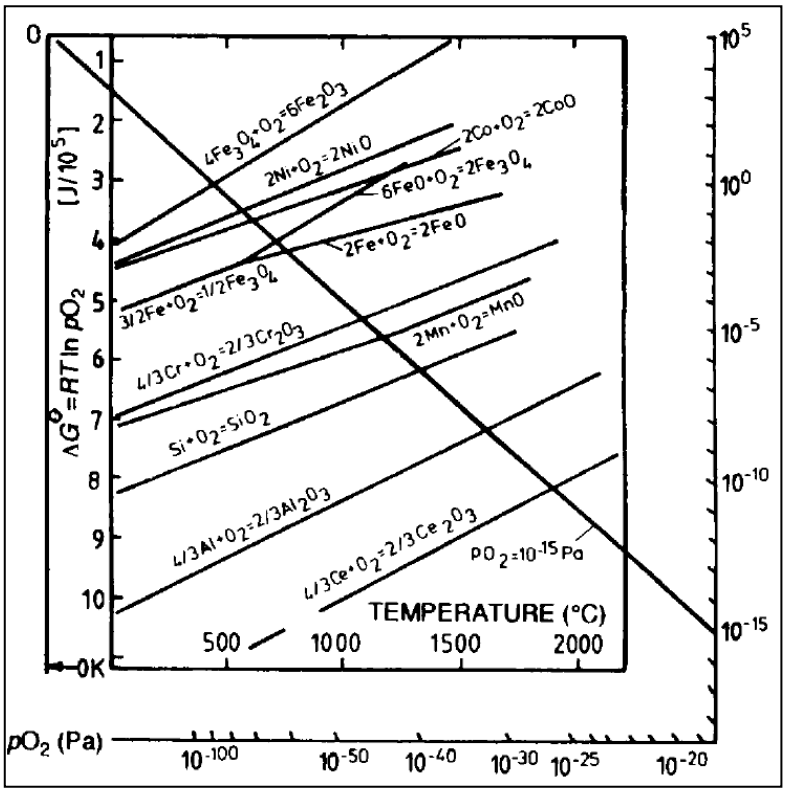


Figure 2.2: Ellingham diagram of oxides plotted against partial pressure [12].

Generally, the process of oxide formation begins with the initial adsorption of oxygen on the alloy surface and the process can be expressed as follows:

$$xM + \left(\frac{y}{2}\right)O_2 = M_xO_y \tag{2.1}$$

where, M represents the reacting metal and M_xO_y the oxide.

2.3 Thermodynamics of oxidation

After formation of the oxide scale, coexistence of the metal (alloy) and oxide scale is crucial. The oxygen partial pressure at which the two coexist can be derived from the following relationship:

$$p_{O_2}^{M/M_xO_y} = \exp(-\Delta G^\theta / RT) \tag{2.2}$$

The Gibbsian term, ΔG^{θ} significantly indicates the energy required to develop the oxide, hence its stability. Thus, from Eq. 2.2, the viability of each oxide at a given partial pressure depends on temperature.

In addition to temperature, element activity affects the minimum oxygen potential necessary to form a metal oxide. Surface activity for each element is also crucial for both bulk and surface reactions taking place during oxide formation.

The oxygen partial pressure at which reactions between the metal and its oxide are in equilibrium is related to the metal and oxide activities as follows:

$$P_{O_2}^{eq} = \frac{a_{MO_2}}{a_M} p_{O_2}^{M/MO_2} \tag{2.3}$$

Thus, Eq. 2.3 represents the equilibrium dissociation pressure of the metal oxide MO_2; the metal oxide will not form unless the ambient pressure exceeds $P_{O_2}^{eq}$. From Eq. 2.3 the dissociation pressure is a function of the metal activity and thus varies for different metal oxides. Apart from the oxide formed, the elemental composition of the alloy also plays a crucial role in the interactions between the alloy and the oxide.

Of importance, are the effects that alloy composition has on adhesion (in the case of external scale) and development of the oxide scales both internally and externally. The importance of composition in internal oxidation has been revealed in the work by Stott *et al*. [16] for Ni-Al and Ni-Cr alloys where different internal oxide morphologies were observed for different compositions. From studies [16, 17] rod-like structures prevail as internal oxides in Ni-Al system at higher Al concentrations, and acicular structures prevail in the dilute Ni-Al system, while the structures in Ni-Cr system tend to be spherical. $NiAl_2O_4$ and Al_2O_3 develop as internal oxides in the Ni-Al alloy system and Cr_2O_3 in the Ni-Cr alloy system [16, 17]. The effects of alloy composition on the external oxide scale development and behaviour has been widely reviewed in several research works [11–16]. However, in high temperature applications of alloys the major goal is to develop a stable surface oxide which serves as a barrier between the underlying alloy and environment. The surface oxide must be able to prevent further alloy oxidation for the alloy to be quantified as environmentally stable.

2.4 Kinetics of oxidation

An alloy can be said to be environmental stable if it can develop and sustain a protective and adherent scale such as corundum alumina. Development of external corundum alumina (α-Al_2O_3) results in oxidation kinetics defined by diffusion through the scale. In the case of the absence of an external protective scale and development of internal oxides or internal oxidation, oxidation kinetics are defined by the rate of progression of the oxidation front into the alloy matrix [16, 17]. As the oxidation front proceeds deeper into the alloy matrix an internal oxidation zone (IOZ) is created. The morphology of oxides in this region has been found to vary with depth as have the oxides in the external scale. There are three rate laws used to define the kinetics or rate of oxidation reactions and these rate laws mainly depend on diffusion of reactants through scales or reactions at phase boundaries [9].

Thus, for an oxidation reaction given in Eq. 2.1, the basic kinetic rate law is:

$$\frac{dX}{dt} = f(t) \tag{2.4}$$

In Eq. 2.4, X is a measure of the extent of reaction at time, t.

Depending on the mechanisms in effect, Eq. 2.4 varies to represent the reaction taking place and hence different rate laws.

For the rate of oxidation controlled by reactions taking outside the scale, the result is controlled by linear kinetics indicated as:

$$\frac{dX}{dt} = k_1 . \tag{2.5}$$

When integrated, Eq. 2.5 yields:

$$X = k_1 t \tag{2.6}$$

In Eq. 2.6 k_1 is the linear rate constant. Thus, in the case of the linear oxidation rate, scale thickness does not have control over the oxidation rate, the overall rate being controlled by phase boundary processes.

Considering a case where interfacial reactions are at equilibrium, the growth rate of a compact scale will be controlled by diffusion of some of the reactants through the scale. In such cases, the scaling is determined by properties of the oxide which are its composition and its diffusion

coefficient with the metal and the oxidant at equilibrium. In this case, the reaction rate depends on the rate of scale thickening which decreases with time as follows:

$$\frac{dX}{dt} = \frac{k_p}{X} \tag{2.7}$$

Integrating Eq. 2.7 gives:

$$X^2 = 2k_p t \tag{2.8}$$

where k_p is the rate constant and scale thickness $x = 0$ at time $t = 0$ [9].

Thus for an oxidation reaction controlled by diffusion through an oxide scale parabolic kinetics are promoted and this is due to reduced transport of reacting species across the scale as it continually thickens.

Usually oxides are initially thin and as a result the oxidation kinetics are controlled by phase boundary reactions resulting in a linear oxidation rate. As the scale thickens, diffusion becomes the rate limiting process. This gives rise to a reaction involving both linear and parabolic kinetics described by the following rate equation [18]:

$$X^2 + LX = kt + C, \tag{2.9}$$

where L and C are constants.

For a particular alloy composition the oxidation behaviour is also subject to other parameters constituted by the environment in which the oxidation is taking place. These parameters are of considerable impact, and adversely impact on the kinetics and thermodynamics of the process. Such parameters are the oxygen partial pressure and the temperature. Assessing the contribution and the role of each parameter on the outcome of alloy oxidation is crucial. These parameters can be external or internal. External parameters are considered to be those constituting the environment in which alloy oxidation is taking place and these are commonly: temperature and ambient pressure. Internal parameters are considered to be parameters such as: phases present, number of elements present and their concentration. It can be appreciated from the vast amount of modeling work undertaken by Gesmundo *et al*. [19, 20, 21] that alloys with the same composition, but different phases present different oxidation behaviour. This is attributable to the solubility of the scale forming element in the other phase(s) present and its diffusivity.

The solubility and diffusivity of alloy components are very significant to the reactions taking place during oxidation when the gaseous species have no access into the alloy. Access of the gaseous species into the alloy entails the control of the diffusion kinetics by the oxygen partial pressure in addition to the alloy's components. However, temperature mostly affects the stabilities of the phases present. The dependence of various oxide phases on different temperatures is well documented [22, 23]. However before the phase transitions can be considered, it is important to consider the general concepts that are involved in oxide formation and development, and the trend in the behaviour of alloys at different solute concentrations.

2.5 General concepts of alloy oxidation

The oxidation mechanisms of binary alloy systems are well documented [9, 10, 24]. Oxidation reactions taking place in simple to complex alloys can be mapped from the simple binary A-B alloy system, where A and B are components in the system, A being the more noble element and B being the reactive element. With the oxygen partial pressure and temperature fixed, treatments by Gesmundo [25] showed that the concentrations of the components A and B determined the type of oxide that will be formed. This implies that diffusion kinetics of each element and the element to be oxidized at the alloy surface is concentration driven and, hence, the observation that the type of oxide formed is dependent on concentration. Formation of the oxide of the more reactive component will take place if there is higher flux of this component and if the ambient pressure exceeds the oxide's dissociation pressure.

Flux is concentration driven and this implies a high concentration of solute element (B) is necessary in the matrix in order for the oxide (BO) to develop externally [26]. Several studies have so far indicated that an external BO oxide is established when the element B is present in adequate levels necessary to develop and sustain an external scale. In the case of the addition of a third element C being added to a binary system A-B, the amount of element B required to develop an external scale is lowered giving rise to an effect called the third element effect (TEE) [25, 27]. However, this third element should also be a scale forming element. The third element effect is easily illustrated in binary Ni-Al alloy systems where the concentration of Al required by each alloy to result in an external alumina is significantly lowered by the presence of Cr [28, 29].

A review of oxidation studies in alloys shows that oxidation studies have been commonly carried out for alloys with a two-phase microstructure. In the work of Gesmundo and Gleeson [19], microstructure was observed to play a significant role in the oxidation outcome as it does in the mechanical strengthening of the alloy. This is explained by considering the contribution of different phases to processes involved in alloy oxidation such as bulk diffusion of solute atoms. In cases of internal oxidation, microstructure has influence on the way that internal oxides nucleate. It has however been pointed out [11, 19, 20, 21, 27] that there is not yet a satisfactory mechanism that can sufficiently account for the oxidation behaviour of either two-phase or multiphase alloys.

As pointed out earlier, the complexity of oxidation reactions in a given alloy increases with the complexity of an alloy or the environment, and elemental composition is one of the factors which significantly complicates oxidation reactions taking place and hence oxidation studies in a given alloy system. For this reason, model alloys of binary and ternary compositions are often used to study or simulate oxidation reactions in NBSAs. A simple binary M-Al alloy as shown in Figures 2.3 and 2.4 is used to illustrate the criticality of sufficient Al concentration (N_{Al}) for the development of an external alumina scale.

Case 1, M-Al concentrated in Al M-Al



Figure 2.3: Schematic cross-section of an M-Al alloy concentrated in Al showing an external layer of Al_2O_3. Modified from [9, 10].

Case 2, M-Al dilute in Al

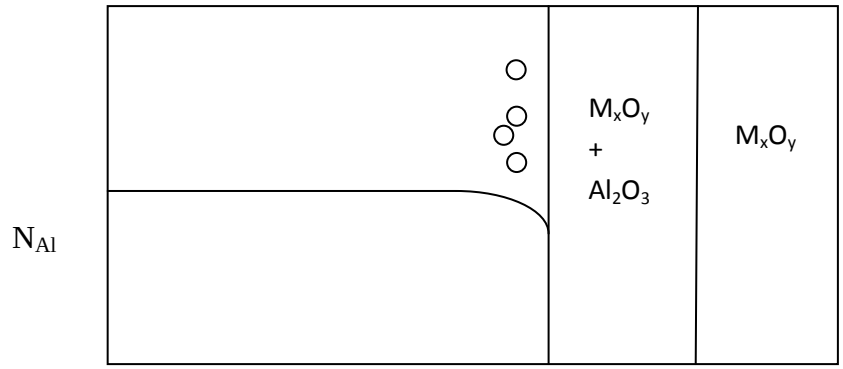


Figure 2.4: Schematic cross-section of an M-Al dilute in Al showing internal oxidation of Al under an external layer of M_xO_y. Modified from [9, 10].

High concentrations of Al are required to result in an external protective scale in Ni-Al alloys Figure 2.3. In the case of low concentrations of Al to form a protective scale, less protective scales develop in turn, Figure 2.4. Internal oxides then develop as a result of oxygen ingress through the less protective scale. However, very high concentrations of Al in alloys are critically devastating on the mechanical strength of the alloy [26] due its low melting point. Hence, design efforts of alloys with both mechanical and oxidation integrity are based on the basic ternary, M-Cr-Al alloy fundamentals.

Introduction of Cr lowers the amount of Al required to form an external Al_2O_3 scale without compromising both the oxidation properties and mechanical strength of the alloy. Basically, the Cr in M-Cr-Al diffuses more rapidly in the alloy(s) [11, 26] due to its high reactivity resulting in the Cr-based oxide overgrowing the Al-based oxide. The reaction of Cr with oxygen modifies the activity of oxygen at the alloy surface which reduces the chances of oxygen diffusing into the alloy to cause internal oxide precipitation. As a result of limited access of oxygen to the alloy, the oxygen partial pressure at the base of the developing oxide scale is lowered to very low levels such that only oxides with a much lower dissociation pressure such as Al_2O_3 will preferentially develop.

2.6 Oxidation in Ni-based alloys

Three parameters affecting oxidation, namely, composition, oxidant pressure and temperature have been considered so far. Though composition does influence the type of the oxides that can form during oxidation, it does not have such a strong influence on the phase in which the developed oxide will exist. Thus the evolution of oxide phases can be said to be independent of composition. This can be well illustrated using alumina. Developmental variations in the polymorphic forms of Al_2O_3 show that temperature increments bring about phase transitions in the oxide. The process of phase transition is also time-dependent [30].

A number of studies [22, 23, 30, 32] confirmed that alumina does have many polymorphic forms and can exist in any of the following transition phases depending on other factors and these phases of alumina are: cubic alumina γ-Al_2O_3 (space group $Fd\bar{3}m$) [32], θ-Al_2O_3 (space group C2/m) which is monoclinic and δ-Al_2O_3 (with two possible structures and space groups $P2_12_12$ or $P2_12_12_1$). All the three transition aluminas discussed above are characterized by high defect concentrations. Due to their high defective nature, transition aluminas are less dense and hence are also susceptible to high cationic diffusion. Transition aluminas also exhibit densities of varying degrees as would be expected from their different structures and ordering of aluminum and oxygen atoms. Figure 2.5 illustrates the mechanism in which cationic and anionic reordering occurs in alumina and how the transition from one phase to another takes place within the oxide until a less defective and stable α-Al_2O_3 develops.

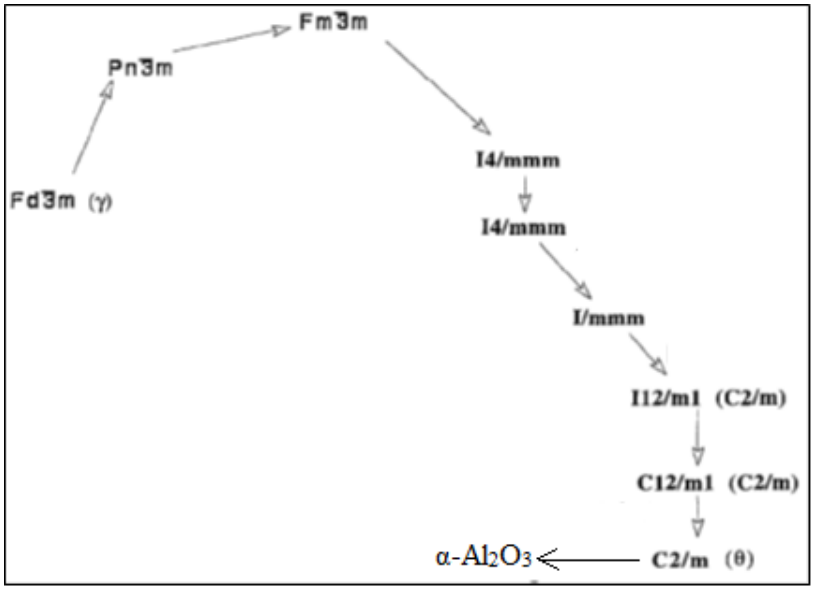


Figure 2.5: Subgroup/supergroup symmetry relations between the $Fd\bar{3}m$ and $C2/m$ space groups for the γ-Al_2O_3→θ-Al_2O_3 transformations. Modified from [23].

In Figure 2.5, the arrow length indicates the magnitude of symmetry. The arrows connect the allowed maximal group/sub- or supergroups while the crystallographic variants are shown as the bracketed numbers.

Transition aluminas are often observed to exist together, and also to coexist with stable alumina (corundum phase) at lower oxidation temperatures [14, 33, 34], while at high temperatures only the corundum is observed to exist. Transition in alumina is a gradual process such that it is often necessary to employ electron diffraction analysis in order for the co-existing phases to be distinguished. The final transition process in alumina is a transition into the stable alumina form, α-Al_2O_3; this process being promoted by very high temperatures. Thus the continuous reconstructive ordering of cations and anions [35, 36], is also a thermally aggravated process which results in the corundum alumina, as also indicated in Figure 2.5.

Compared to transition aluminas, α-Al_2O_3 is less defective and denser, and is thus characterized by very low and minimal diffusivities of cations and oxygen [30] and as a result is of great significance to the protection of alloys against further oxidation [10, 11, 22, 26]. This is true for an external and adherent α-Al_2O_3. Longer oxidation times also facilitate the transition into α-Al_2O_3, even at lower temperatures, and some alloying elements are reported to have the effect of increasing the rate of this transition [35]. The principle behind some alloying increasing this rate of transition however still needs to be verified. The effects of reactive elements (RE) and rare elements such as Hf, Zr and Y in enhancing the adhesion between external α-Al_2O_3 scale in various alloy systems have been well verified both theoretically and experimentally [38-41]. Several ways in which these elements improve adhesion between α-Al_2O_3 and NBSAs have so far been proposed and confirmed [1, 9, 10, 11, 26, 27].

The functionality of α-Al_2O_3 fundamentally lies in its structure, which is made up of Al atoms octahedrally coordinated with the oxygen atoms and occupying two-thirds of the octahedral interstices [2, 42, 43]. Thus this stable alumina exhibits a rhombohedral structure (space group $R\bar{3}c$). The significance of temperature in oxidation has been shown from X-ray diffraction studies of oxide products formed at various temperatures for a given time [34].

2.6.1 Ni-Cr-Al alloys

A number of studies [30, 44, 45, 46] confirmed the development of α-Al_2O_3 at temperatures above 1000^{o}C, and at sufficient concentration of this scale forming element, protective external scale is guaranteed. The likelihood of an external protective scale developing on the various compositions of NBSAs can be derived from an oxidation map of a ternary system, Ni-Cr-Al. An oxide map of a binary Ni-Al system would not accurately represent the Al elemental concentrations that are found in NBSAs or Ni-base alloys due to the very high Al concentrations that would be required in the system to develop an external scale. Such high Al levels have degrading effects on the alloy strength, but the presence of Cr in Ni-Cr-Al and NBSAs significantly lowers the Al concentrations required to generate the same external alumina scale. Fig. 2.6 shows an oxidation map of a Ni-Cr-Al system as derived by Chen *et al*. [47] at a threshold temperature for α-Al_2O_3 formation.

From Figure 2.6, oxide development is clearly shown to be a function of composition, of which the concentration of the oxide forming elements is critical, as indicated in the composition region and oxide type formed.

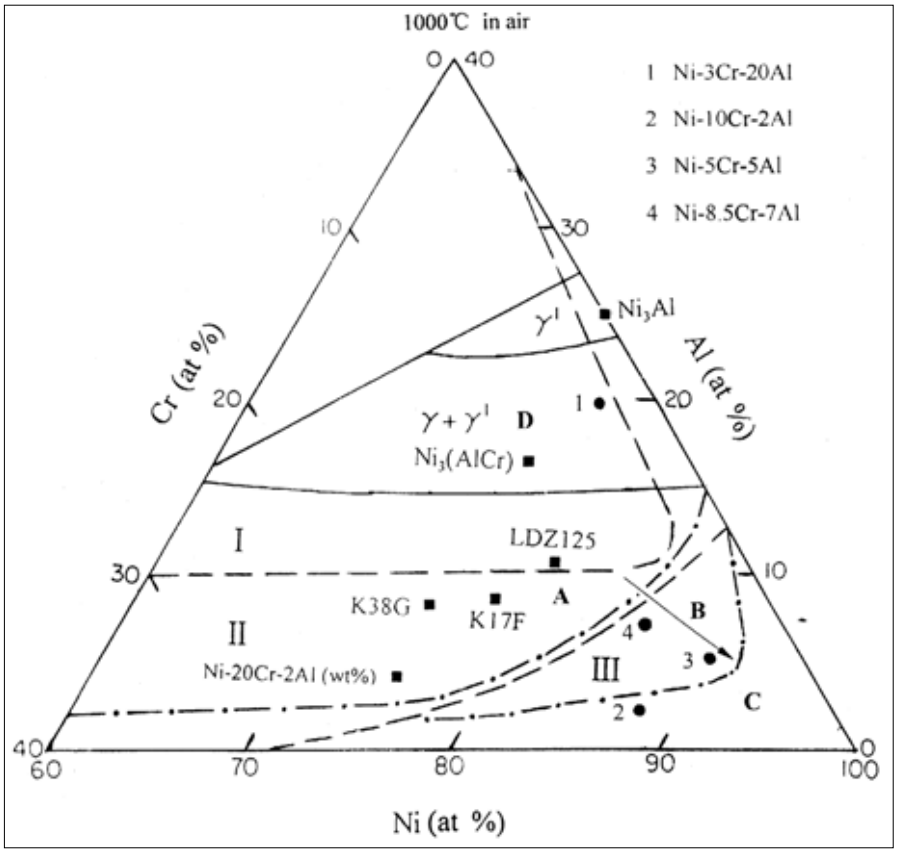


Figure 2.6: Oxide map for ternary Ni-Cr-Al alloys at 1000^{o}C [47].

Figure 2.6 shows three composition groups which can be classified according to scale morphology analysis:

- *Group I*: Al and Cr concentration promote development of an external Al_2O_3 layer.
- *Group II*: Cr_2O_3 develops externally and Al_2O_3 internally.
- *Group III*: Internal Al_2O_3 and/or Cr_2O_3 with external layer of NiO.

The complexity of oxidation studies can be appreciated if one considers the number of parameters that have to be fixed in order to study the effect of one variable in alloy systems, thus only one of the following: composition, temperature, oxidant pressure and oxidation time should be varied to make reasonable comparisons. This is often not the case in most oxidation studies making such studies difficult.

However, in most of these studies, the propensity of internal oxide formation in the later generation NBSAs is seemingly inevitable. This is prompted by the absence of a scale to prevent access of the oxidant to the alloy surface, hence resulting in the desorption of the gaseous species into the alloy. Ingress of the gaseous species usually occurs in the presence of less protective external scales such as NiO and $NiAl_2O_4$ [48], whose structures shall be discussed later to elaborate on their lack of protection against environmental degradation.

2.6.2 Ni_3Al intermetallic compound

Despite its functional role in high temperature applications as an intermetallic, Ni_3Al also exists in Ni-base alloys as a strengthening phase (γ') with a reasonably high melting temperature of 1390^{o}C [49]. γ'-Ni_3Al has an $L1_2$ ordered structure of Cu_3Au type [43], with lattice sites for the sublattice for Ni atoms being three times more than for Al and all the three low index surfaces (100), (110) and (111) being bulk terminated [50]. Observations of the significant NiO and $NiAl_2O_4$ oxides, in addition to an internal Al_2O_3 scale in Ni_3Al alloy oxidation [48] confirm the high Ni-to-Al ratio. Due to its thermodynamic stability (more negative Gibbs free energy), internal alumina is reasonably expected to develop deeper where the partial pressure is much reduced upon ingress of oxygen into the alloy, with an Al depleted zone forming below the scale. The low Al content in Ni_3Al lowers the activity and diffusivity of Al in the alloy which leaves Ni only to reach the alloy surface, react with

oxygen and form an external NiO due to its high activity. Due to the highly defective nature of NiO substantive ingression of oxygen takes place through the oxide, which leads to internal oxidation of Al and formation of internal Al_2O_3.

From a consideration of the Gibbs free energy of formation [51], NiO is likely to result from the following reaction:

$$Ni + \frac{1}{2} O_2 = NiO \qquad (2.10)$$

However, a study by Gao *et al*. [52] showed that oxygen partial pressure plays a critical role in the manner that the Ni_3Al intermetallic compound oxidizes. Under various pressures, different oxidation behaviours were observed, and at oxygen pressures below 10^{-22} atm., an external alumina scale was observed with an absence of Ni particles on the surface. For oxygen pressures in the range of 10^{-15} and 10^{-18} atm., Ni particles were observed on the alloy surface as well as the formation of an internal 'self-healing' alumina scale after long exposure times. Gao *et al*. [52] substantially reiterated the general concept of composition being the major variant controlling the oxidation outcome, and as generally perceived from the composition point-of-view, an external alumina is impossible for the Ni_3Al intermetallic compound. A study of this intermetallic phase at a low oxygen partial pressure of $4x10^{-19}$ atm. and temperature of 950^oC [22] again showed similar results to those of Gao *et al*. [52] except that an external alumina scale was observed. In addition to this, various epitaxial relationships were observed in alumina as the oxide evolved through its various polymorphic forms. A study of the change of orientations of oxides with phase and depth can be of further importance in characterizing the oxidation of Ni_3Al and other Ni-base alloys.

2.6.3 β-NiAl alloys

A 50:50 at. % Ni-Al binary alloy is a NiAl B2-ordered intermetallic compound, with a relatively simple CsCl crystal structure. Deviation from the stoichiometric composition means that NiAl is either Al-enriched predominated by vacancies on the Ni-sublattice, or Ni-rich with anti-structural Ni atoms on the Al sublattice. Generally, β-NiAl alloys are desirable in oxidation studies, due to the formation of a pure alumina scale upon selective oxidation of Al at higher temperatures [30]. Pure alumina formation in β-NiAl alloys is due to the exclusive contribution of Al to oxidation [30, 53], although at lower temperatures and short oxidation

times, NiO and spinel oxides also develop [54]. Development of such oxides is also encouraged by high oxygen pressures such as in air [55, 56]. However, spinel oxide formation is highly restricted in these alloys such that in the oxidation studies carried out in β-NiAl alloys, the oxides were observed to disappear after only one hour at 800^{o}C, and only metastable θ-Al_2O_3 remained [54, 57].

2.7 Oxidation in Ni-based superalloys (NBSAs)

Interactions in nickel-base superalloys are complex as indicated by diffusion studies which are mainly limited to binary and ternary systems, but present complications in NBSAs [16-21]. In less complex alloys (binary and ternary alloys), Fick's laws of diffusion can be easily applied to model relative diffusion kinetics of components in the system in order to understand oxidation. However, such simple treatments do not easily apply in NBSAs, and hence the need to rely on experimental observations to a larger extent.

NBSAs mainly differ from the model alloys discussed above in the concentration of the scale forming elements and the presence of other non-protective scale forming elements. Different generations of NBSAs yield different oxidation behaviours due to the reduction of the concentration of the scale forming element, Cr from one generation of NBSAs to another [1, 58, 59]

The presence of other alloying elements in addition to Al and Cr generally results in a variety of oxides and stoichiometries developing in NBSAs when compared to simple alloys [14, 22, 30, 33, 34]. Compared to the model alloy, binary Ni-Al, the presence of additional alloying elements in NBSAs presents differences in the overall oxidation kinetics and phase transformations between the two alloy systems. Considering the complicated kinetics and phase transformations in NBSAs, Akhtar's group [15] derived an oxidation model for the 3rd-generation nickel-base superalloy, CMSX-10. In the oxidation model, three oxidation pathways were presented as shown in Figure 2.7, the model being based on the group's experimental findings.

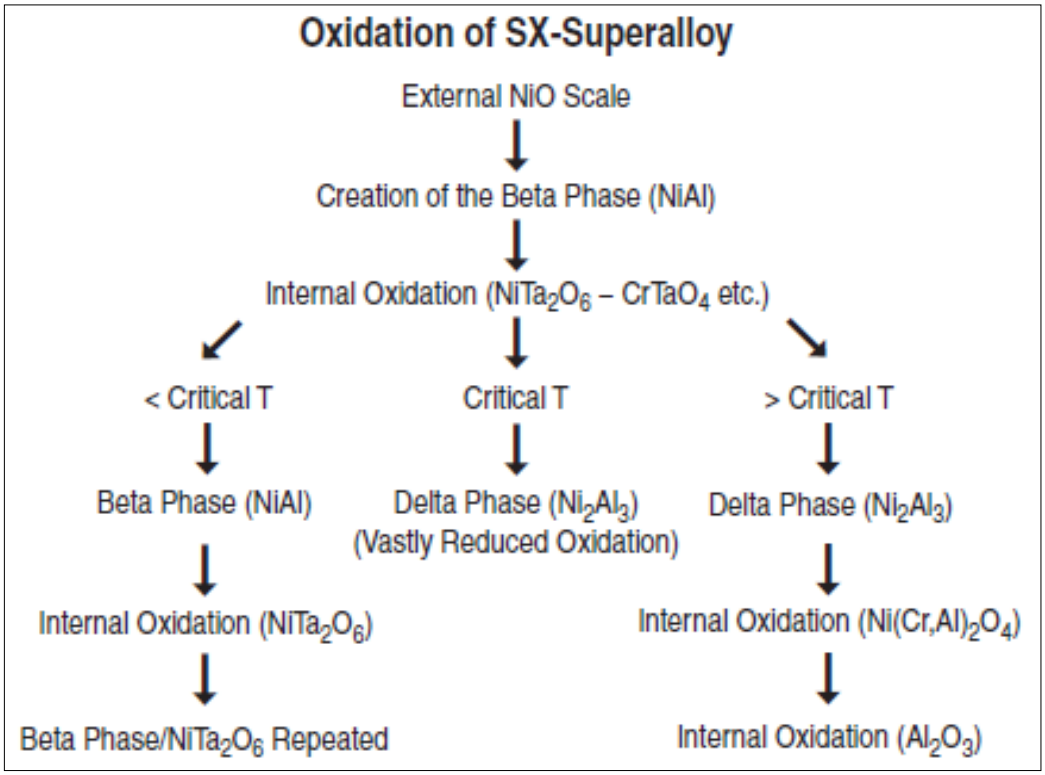


Figure 2.7: Sequence of events during oxidation of nickel-based CMSX-4 single crystal superalloys at 900°C for 100 h as proposed by Akhtar *et al*. [15].

Ideally, oxidation can be classified as either internal or external, depending on the scale behaviour. An alloy can be classified as having undergone internal oxidation when oxides develop within the alloy matrix, whether in the presence or absence of an external scale. In the case of absolute external oxidation, an external scale develops with no internal oxide precipitation. For both internal and external oxidation, two processes are fundamental, these being oxide nucleation and growth. These two processes usually determine the shape and orientation of the oxide in internal oxidation and the morphology of an external scale. Also, apart from the internal oxide development, development of new non-oxide phases is also observed to follow the growth and nucleation pattern. The study of internal oxidation in a Ni-based superalloy CMSX-10 oxidized at 900°C [15] revealed the uncommon behaviour of an absence of internal Al_2O_3 development, either as discrete particles or in a continuous form. From the same study, the oxide spinel $Ni(Cr,Al)_2O_4$ was also noted to be absent at temperatures below 1000°C, which is uncharacteristic of most NBSAs.

The prominence of internal oxidation was also observed in the 1st-generation Ni-based superalloy CMSX-2, despite the high concentrations of the scale forming elements Al and Cr. This observation indicates that apart from composition, internal oxidation can be triggered by

a number of other factors. Cross-sectional analysis in these alloys oxidized at a temperature of 1000^{o}C indicated three oxidation zones [60], these being identified as: a thin external scale of regular thickness, an internal oxidation zone and a zone depleted in γ′-precipitates. Internal oxides of $NiAl_2O_4$ and γ-Al_2O_3 were observed in the temperature ranges between 900^{o}C and 1100^{o}C for this alloy while an external α-Al_2O_3 was observed at temperatures above 1100^{o}C. However for CMSX-4, a 3rd–generation superalloy, Younes's group [13] observed α-Al_2O_3 as an external scale at 1100^{o}C, and also, spinels of $(Ni,Co)Al_2O_4$ and $(Ni,Cr)_2O_4$. The manner in which a single crystal Ni-base superalloy oxidized in the work carried out by Li *et al*. [14] presented a characteristically common behaviour in the oxidation of these alloys where oxides show a non-uniform structure. Li *et al*. [14] showed that this trend is temperature dependent as illustrated in Figure 2.8, where the non-uniform oxide structure at 800^{o}C changed to a more planar and uniform oxide structure at 900^{o}C.

The behaviour in Figure 2.8(a) is consistent with several other observations [15] on the oxidation behaviour of latter generations of single crystal Ni-base superalloys.

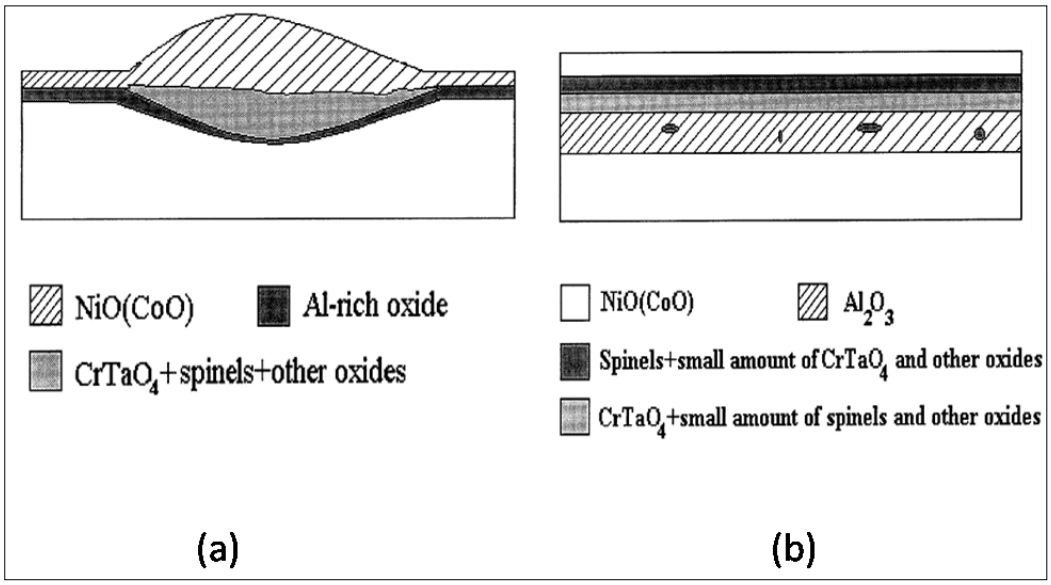


Figure 2.8: Schematic model for scale and subscale growth on the single crystal Ni-based superalloy (with 6.3 wt% Al, 6 wt% Cr, some Co, Ti, Mo, W and Ta) at (a) 800^{o}C and (b) 900^{o}C [14].

Phase changes in the internal oxidation region can be considered to be a function of depth, and these do not always occur uniformly across the alloy, as shown in Figure 2.8. Thus, some regions across the alloy are often observed to have deeper oxide penetration than others,

Figure 2.8(a). Such behaviour often makes it difficult to analyze the stability of each oxide from depth analyses and also make X-ray diffraction analysis yield different phases. Such behaviour still needs further investigation in order to determine why such scale morphology exists when the oxidation front is expected to penetrate linearly and planar.

2.8 NiO and $NiAl_2O_4$

The oxide NiO and nickel-aluminum spinel, $NiAl_2O_4$, are commonly observed in high temperature oxidation of most Ni-base alloys as transient oxides [14, 33, 34, 36]. Despite their occurrence to a greater extent in these alloys, these oxides are generally of little significance to high temperature alloy oxidation due to a lack of protection against oxygen diffusion into the alloy, hence allowing further alloy oxidation and undesired internal oxidation. The oxides NiO and $NiAl_2O_4$ are characterized by high defect concentrations which allow rapid lattice diffusion of oxygen, thus leaving the alloy exposed to further oxidation reactions. NiO occurs in two structures: the cubic (NaCl-type) structure with space group (Fm3m) and the rhombohedral structure with space group ($R\bar{3}m$). The oxide spinel $NiAl_2O_4$ is a result of a solid–state reaction between NiO and γ-Al_2O_3 [56]. $NiAl_2O_4$ has a general formula: AB_2O_4, where A and B, are divalent and trivalent cations respectively. The spinel can also be modified through solid state reactions such as substitutions in the Ni and Al sublattices by Co and Cr respectively.

CHAPTER 3

Internal oxidation in nickel-based superalloys

The following chapter presents work on the mechanism by which internal oxidation takes place in NBSAs. The internal oxidation process is considered to be more favourable at low oxidation temperatures and low Al activity (low Al concentration). The complexity of this process in multi-element alloy systems limits the studies on the classical theory of internal oxidation to mostly binary alloy systems.

3.1 Progression of internal oxidation

Simulations based on the kinetics of internal oxidation are made by considering the solute element B in a binary A-B alloy, where A is the noble element [19, 20]. Ingression of oxygen proceeds in the absence of a protective scale and at a low oxygen partial pressure to oxidize the noble element A. An oxidation front can be assumed to progress into the alloy as shown in Figure 3.1, the oxidation taking place for those elements with oxides whose equilibrium pressures fall below the oxygen partial pressure.

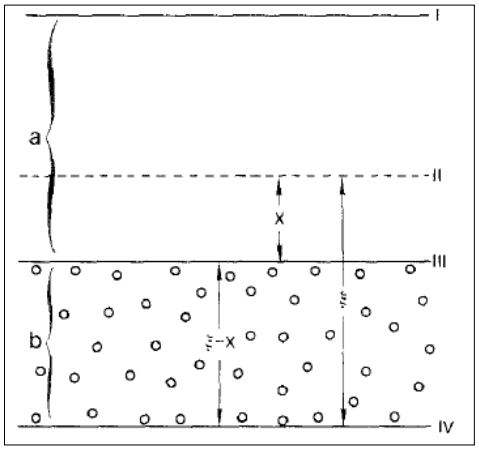


Figure 3.1: Schematic view of a corroded sample: I, actual scale/gas interface; II, original alloy/gas interface; III, actual alloy/scale interface; IV, internal oxide precipitation front; (a) external scale (oxide AO); (b) internal oxide region; X, thickness of alloy consumed; ξ, position of the internal oxide front measured from the original alloy surface; (ξ-X), actual thickness of the internal oxide region [61].

The development of internal oxide precipitates normally stems from the lowering of scale forming elements Al and Cr to inadequate levels, which is also aggravated by the presence of a region depleted of these elements (γ-phase). The high oxygen permeability of the γ-phase [16, 61, 62] does facilitate internal oxidation from selective oxidation under aggravation of high temperatures and scale spallation [63]. The occurrence of internal oxidation in cases where selective oxidation and spallation do not lead to high oxygen permeability should however be dependent on different parameters and kinetics. Edmonds *et al*. [64] showed that internal oxidation is also highly restricted to the γ′ precipitates. The confinement of internal oxidation to γ′ precipitates, despite their existence in the vicinity of the matrix, is an indication that the γ′ precipitates are oxidized at a lower oxygen potential than that required to oxidize the matrix. As pointed out in the oxidation of nickel aluminides [53, 54, 57, 65] and Ni_3Al at low oxygen pressure [20, 63], the exclusive contribution of Al from the precipitates to internal oxidation results in the following reaction taking place in the internal reaction zone:

$$\frac{3}{2}O_2 + 2Ni_3Al \rightarrow 6Ni + Al_2O_3 \qquad (3.1)$$

The difference between the reaction indicated in Eq. (3.1) with the general reaction for Al_2O_3 development indicates that the γ′ phase is used up during Al_2O_3 formation. The process also results in the build up of excess Ni. Of significance are the volume differences between the precipitates Ni_3Al and Al_2O_3 within the matrix and the overall internal oxidation kinetics.

A consideration of a planar oxidation front advancing with infinitesimal depths dx from the alloy surface, Figure 3.2 shows that compositional changes and hence phase changes are most likely to take place as the oxidation front advances.

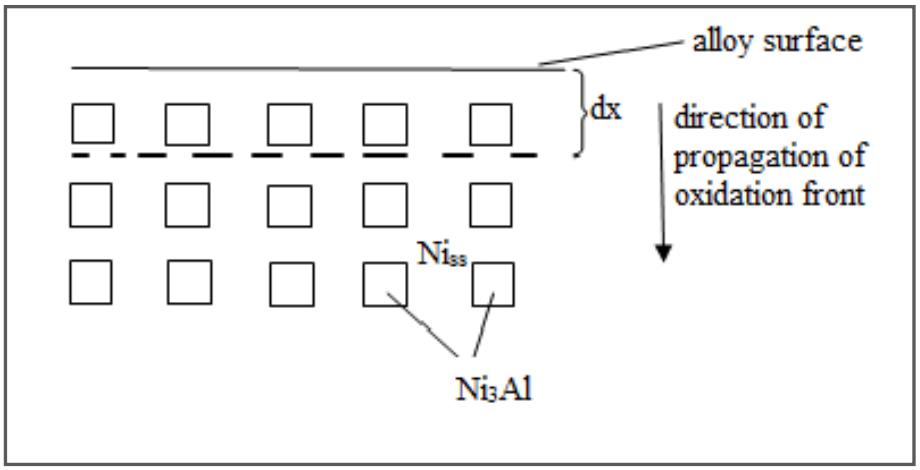


Figure 3.2: Schematic view of advancement of an oxidation front during internal oxidation of a Ni-Ni_3Al alloy [64].

From [14, 61, 63], the disappearance of γ′ precipitates in the alloy matrix is countered by the development of internal oxides, and the lack of linearity in the oxygen front as it advances deeper is assumed to bring about compositional discrepancies at different depths and hence phase changes. Internal stresses due to the nucleation and growth of internal oxides, and the disappearance of precipitates results in compressive stresses which force nickel out of the alloy matrix. The process of nickel extrusion counters oxygen diffusivity D_o which tends to vary parabolically with depth, hence affecting the overall oxygen solubility N_oD_o. Gradually, differences arise in the two competing processes of oxide nucleation and growth as a function of depth.

This process of internal oxidation is considered to follow the following parabolic rate law [59] as given in Eq. 3.2:

$$\xi^2 = 4\gamma^2 D_o t. \tag{3.2}$$

In Eq. 3.2, ξ is the position of internal oxidation front measured from the alloy/gas interface, D_o is the diffusion coefficient of oxygen in the alloy, where γ is a dimensionless parameter related to the parabolic rate constant for internal oxidation, and t is time. In simple binary A-B systems, this oxidation kinetic is associated with a concentration profile of the two most reactive components which are given as follows [66]:

$$N_O = N_O^S\{1-erf[x/2(D_O t)^{1/2}]erf(\gamma)\}, \qquad \text{for } 0 \le x \le \xi \tag{3.3}$$

$$N_B = N_B^O\{1-erfc[x/2(D_B t)^{1/2}]/erfc(\gamma\varphi^{1/2}\}, \qquad \text{for } \xi \le x \tag{3.4}$$

where N_O^S is the mole fraction of O dissolved in the alloy in equilibrium with the partial pressure of oxygen prevailing in the gas, N_B^O is the mole fraction of B in the bulk alloy, D_B is the diffusion coefficient of B in the alloy, x is the distance from the alloy/gas interface, *erf (γ)* and *erfc (γ)* are the error function and complementary error function of γ respectively.

In the same binary A-B alloy used to illustrate the position of the internal oxidation front (depth of the oxidation front), a number of assumptions can be made to Eq. 3.2 in terms of concentrations of the two reacting elements. It will also be assumed that BO_n oxide will be formed due to B having a higher oxygen affinity than A, and also that the oxygen pressure is high enough to oxidize B only. The following approximations are made [62]:

- The reaction front is described by a sharp boundary,
- D_B is so small such that internal oxidation takes place inside the metal (alloy),
- The oxygen solubility is small,
- There is equilibrium between the oxygen concentration at the surface and the solubility c_o and it is all at the same temperature.

Thus

$$c_O D_O > c_B D_B \tag{3.5}$$

where, c_O is the concentration of oxygen, c_B the concentration of B in A, D_O and are the corresponding D_B diffusion constants of oxygen and B in A.

With the fulfillment of Eq. 3.5, internal oxidation will result in the depth of the oxidation front being given by Eq. 3.6 [66]:

$$\xi = \sqrt{\frac{2c_O D_O t}{n c_B}} \tag{3.6}$$

where n is half the valence of B (considering the oxide BO_n is formed).

However, numerical quantifications of concentration profiles are strongly limited to simple alloy systems, where such quantifications as in Eqs. 3.3 and 3.4 are complicated by a degree of solubility of different elements in different phases in multicomponent alloys. The complexity is further intensified by solid solution among elements and phases precipitated,

and hence the need to rely on cross analytical techniques in carrying out studies in higher order alloys.

From cross-sectional analytical techniques [25, 67] the interaction of oxygen and alloy components internally under competitive dissolution (γ') and precipitation (mainly Al_2O_3) takes place in the oxidation reaction domain (ORD).

3.2 Variation of alloy composition with depth of internal oxidation

The variations of composition with depth are strongly demonstrated in numerical treatments which quantify concentration profiles and the penetration depths [16]. Stott *et al*. [16] showed minor variations in the oxide penetration depth with Al concentrations between 0 – 0.08 wt. %, and an increase in penetration depth from approximately 10 – 20 um when oxidation was increased by 10 h. These numerical treatments are diffusion processes within the alloy [68], where basically the gaseous species inward diffusion is normally countered by the outward diffusion of alloying elements.

Of interest is the case whereby a negligible diffusion of Al to the surface takes place, hence promoting the precipitation of internal oxides in the proximity of the γ'-precipitates. Such a tendency is bound to localize oxide precipitation to regions where the oxide's thermodynamic stability is sustained and also where an excess of one or more elements tends to increase the solubility of the gaseous species [68].

In spite of all the assumptions described above, the numerical analysis and quantification presented together with experimental observations [63, 69, 70], analyses have not gone beyond identification of the small discrete phases which are precipitated internally in different Ni-base alloys. Stability of different oxide phases have however been correlated with depth, and structure developments have also been deduced for different alloy compositions [63]. In the studies, different oxide phases were observed to have distinctive shapes. Though different oxides have been well correlated with depth at which they develop within the matrix, much work still needs to be done in order to identify the factors that determine the orientation of oxides within the matrix.

3.3 Internal oxide development and phase changes

Development of different internal oxides can be noted in X-ray diffraction (XRD) studies and Electron Probe Microanalysis (EPMA) investigations in which different diffraction patterns and concentration profiles respectively indicate the variation of oxides and phases with depth. Considering Table 3.1 and Fig. 3.3 and taking into account the effect that depth has on oxide stability, which in turn is determined by the Gibbs energies, it can be hypothetically suggested that there should be a clear boundary distinguishing oxides of different stabilities at different depths. This should only be possible if there are very negligible or no solid solution interactions between two different oxides or oxides from two gaseous species such as oxides and nitrides.

Table 3.1: Values for $\Delta_f H^o$, $\Delta_f G^o$ and S^o for Al_2O_3, Cr_2O_3 and AlN as compounds in Ni-Cr-Al alloy oxidation and nitridation [9].

Compound	$\Delta_f H^o$ (kJ/mol)	$\Delta_f G^o$ (kJ/mol)	S^o (J/molK)
Al_2O_3	-1675.7	-1582.3	50.9
Cr_2O_3	-1139.7	-1058.1	81.2
AlN	-318.0	-287.0	20.2
Cr_2N	-	-	-

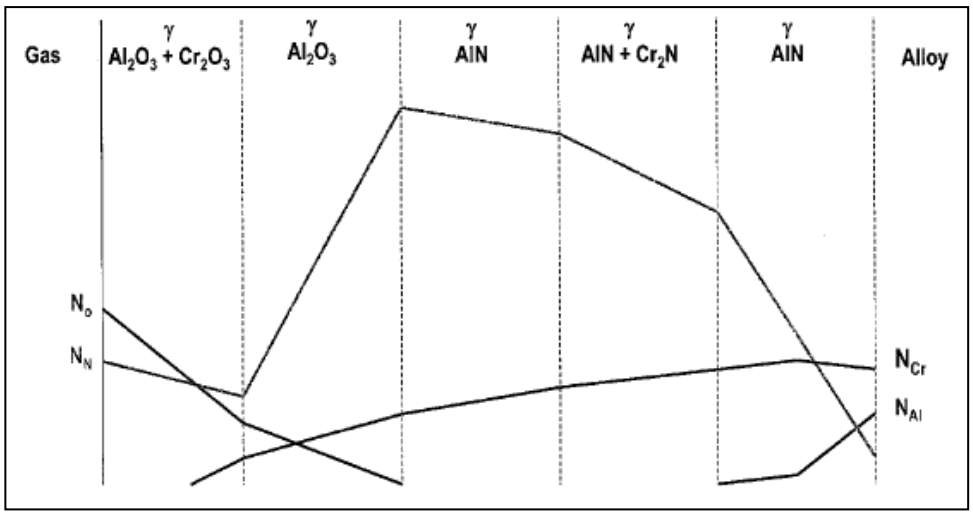


Figure 3.3: Schematic representation of internal-precipitate formation zones and concentration profiles in Ni-Cr-Al alloy system [63].

From Table 3.1 and Figure 3.3, a strong correlation can be seen between the depth of oxides and their stability. Still to be verified are the orientation relationships of these oxides with the matrix with respect to their stabilities.

Two investigations [16, 68] have been carried out, and as far as these investigations were concerned, stability of internal oxides can best be verified from how deep they develop within the matrix from the alloy surface. In addition to orientation relationships existing among various internally precipitated oxides, orientation relationships have also been studied between the alloy and the oxide systems [54, 65, 71].

A study on the orientation relationship between γ-Al_2O_3 and θ-Al_2O_3 [71] showed that the two oxides were oriented as $(001)_\gamma//(100)_\theta$ and $[110]_\gamma//[010]_\theta$. Selected area diffraction (SAD) analysis in NiAl and γ-Al_2O_3 systems [65] also revealed that cube-on-cube relationships existed between the two such that the orientation relationships were [100]NiAl//[110]γ-Al_2O_3 and (001)NiAl//(001)γ-Al_2O_3. However studies of orientation relationships were mainly limited to areas that form an interface between parallel crystallographic planes and directions aligned within those planes [54]. The implication of this is that similar concepts can be used to deduce orientation relationships in both internal oxide and external oxide structures. It will be appreciated that the crystallographic planes defining an interface are also thermodynamically stable; hence orientation relationships are time independent as revealed by Doychak *et al*. [54]. Thus in the present study, investigations concerned the orientation relationships between internal oxides and the alloy matrix. The investigations were carried out through implementing various experimental techniques which are discussed in Chapter 4.

CHAPTER 4

Instrumentation and methods

4.1 The Scanning Electron Microscope (SEM)

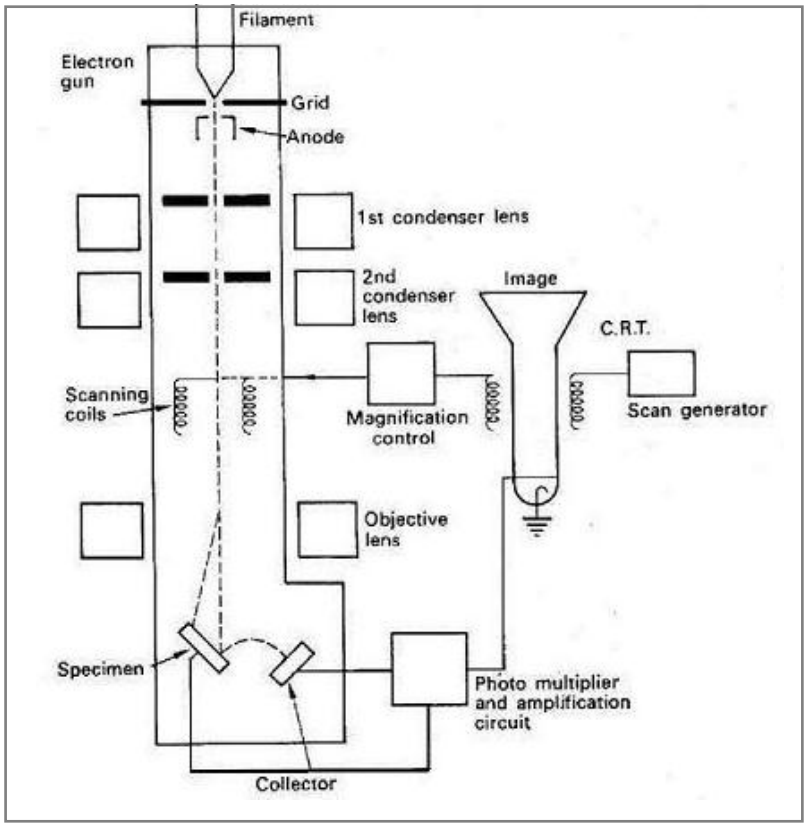


Figure 4.1: Schematic diagram of a SEM [72].

A scanning electron microscope (SEM), shown in Figure 4.1, comprises an electron source, a high voltage supply, typically 1-30 keV, to accelerate the electrons down microscope column, a series of lens to demagnify the source, deflector coils to raster or scan the beam over the sample and a final or objective lens to focus the beam onto the sample. The microscope is maintained under vacuum in order to allow the electron beam to travel unimpeded all the way to the sample. When the electron beam hits the sample, different signals are produced which are collected by various detectors. The signal from a given detector is fed to a monitor which is scanned in synchronism with that of the scan of the electron beam over the sample. The

signal from each point on the sample varies the brightness of the equivalent point on the monitor. The SEM enables 3D imaging through the use of a small final aperture in the electron column which yields a large depth of focus, up to a thousand times greater than for an optical microscope.

Low energy or secondary electrons (SEI), which are emitted from the surface region of the sample, Figure 4.2, yield topographic information, while high energy backscattered electrons (BSE) coming from deeper within the sample reveal atomic number contrast, this signal increasing with atomic number (Figure 4.3). BSE imaging thus shows compositional or phase variations in the sample. An X-ray detector can be utilized to determine the elemental composition of the sample at any point or any area as well as produce elemental maps of different regions. BSE and X-ray imaging are normally undertaken on flat, polished samples in order to exclude topographic information. Although a fine focused beam is incident onto the sample, the area and volume from which such signals are derived can be several orders of magnitude greater as a result of beam broadening within the sample. The size of the interaction volume increases with increasing accelerating voltage and decreasing atomic number.

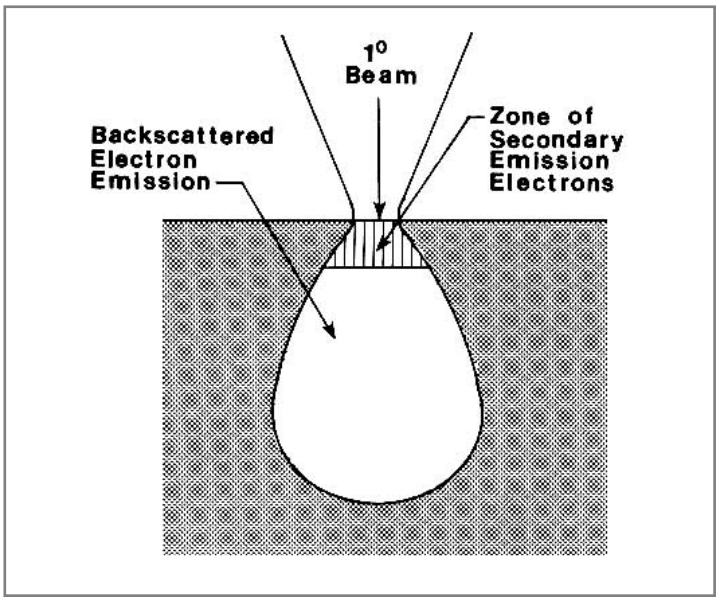


Figure. 4.2: Schematic diagram of the interaction of the electron beam with the specimen. The zones of the secondary and backscattered electron emission are shown within the primary excitation volume [73].

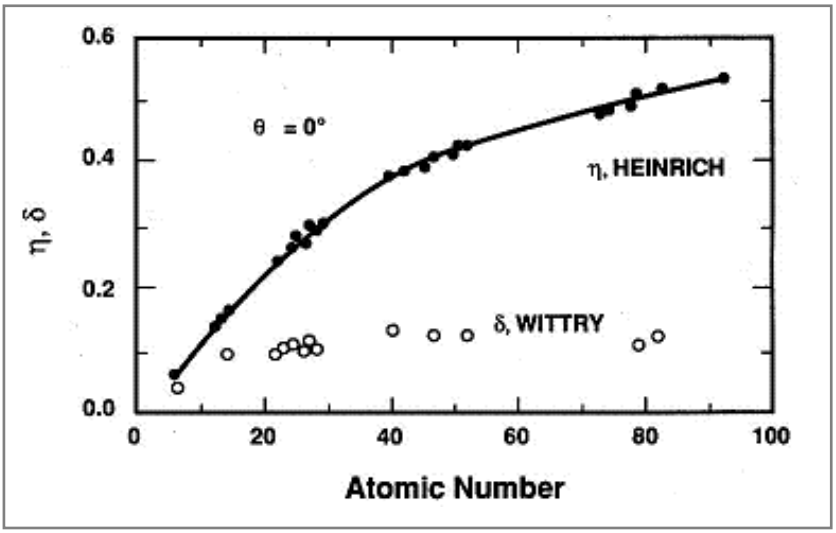


Figure 4.3: Comparison of backscattered electron and secondary electron coefficients as a function of atomic number for an accelerating voltage of 30 keV from the data of Wittry [74] and Heinrich [75]. Figure adopted from [76].

4.2 Transmission Electron Microscope (TEM)

The microscope schematically shown in Figure 4.4, consists of an electron source which supplies the electrons that are then accelerated down the microscope column by a high voltage, typically in the range 120 – 300 kV. The electron beam is focused onto the sample with the condenser lenses, either as a parallel beam for imaging and selected area diffraction or as a focused beam for micro-diffraction and X-ray analysis. The electrons that pass through the thin sample which is positioned at the front focal plane of the objective lens then travel through the objective lens and come together in the back focal plane of that lens to produce a diffraction pattern (Fourier transformed image). These diffracted beams then combine further down the column at the image plane of the objective lens to produce an image of the sample, the diffraction pattern having undergone a reverse Fourier transformation. Depending on the sequencing of the lower lenses, intermediate and projector, either a magnified image of the sample or a magnified diffraction pattern is recorded on a phosphor screen or CCD camera.

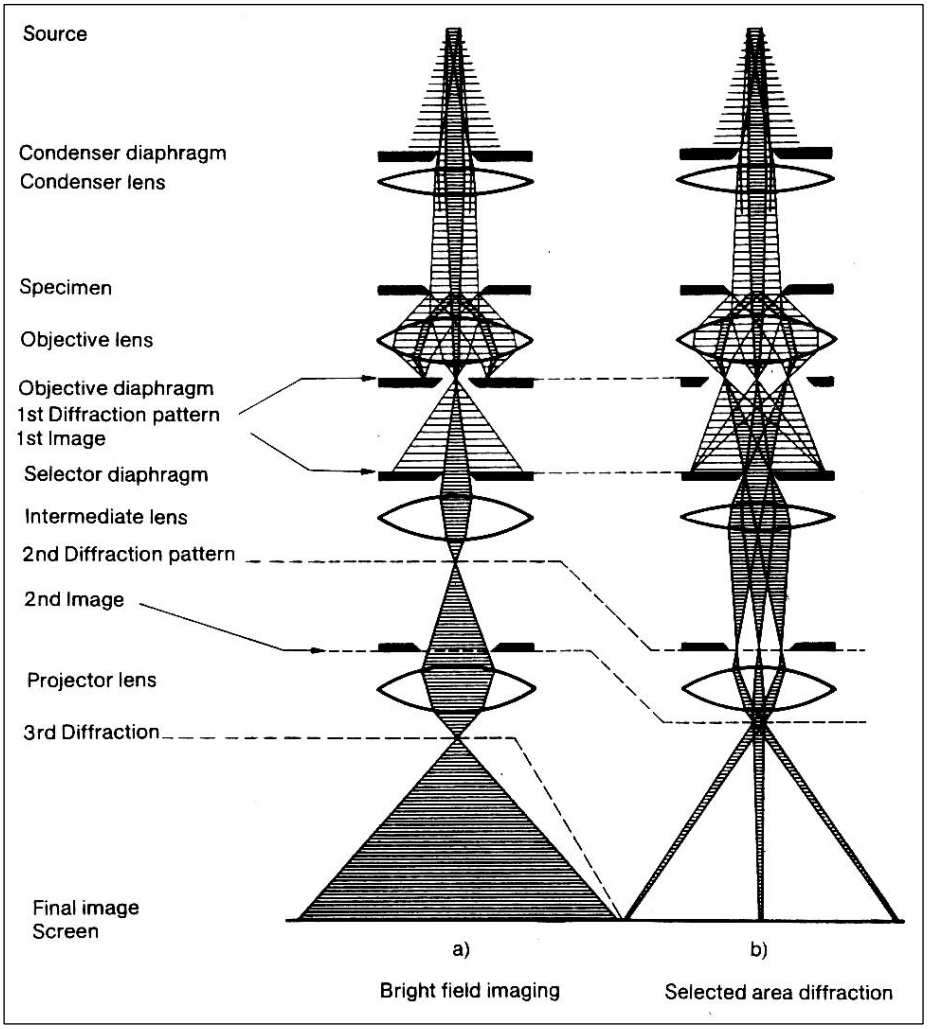


Figure 4.4: Ray diagram for a transmission electron microscope in (a) bright field imaging mode and (b) selected area electron diffraction mode [77].

Movable sets of apertures are available in three locations: (a) in the condenser system to collimate the beam and modify its intensity; (b) in the objective back focal plane to select electrons at particular scattering angles for subsequent magnification such as bright-field using the central transmitted beam only; dark-field using a Bragg diffracted beam only, see below; or lattice imaging using the central transmitted beam and some symmetrically positioned diffracted beams around that beam; (c) in the objective image plane to select electrons from a particular area of the specimen for selected area diffraction (SAD). However, there is a limit to the smallest size of the aperture that can be utilized for SAD, and thus to the smallest area from which a diffraction pattern can be collected. In addition, spherical lens aberration causes displacement of the image in the plane of the SAD aperture such that the transmitted information and the diffracted information are obtained from slightly different areas. Thus SAD is normally best suitable for larger area analyses. For small regions, as for

most of the phases analysed in this investigation, micro-diffraction can be utilized. In this case, the condenser lenses are used to form a focused spot on the sample. This causes the diffraction spots in SAD patterns to be replaced by diffraction discs the sizes of which are governed by the condenser aperture size utilized. For precise beam location on the specimen, the beam is first positioned on the area of interest and then in diffraction mode the final condenser lens focus is slowly changed from under focused to focused. In the central diffraction disc this is seen as the image increasing in magnification. During this process, the beam is moved to keep the area of interest in the centre of the disc until at focussed the magnification is infinite and the disc is uniform in brightness. The only problem with using the focused probe is that carbon contamination buildup is much faster, resulting in fading of the diffraction pattern with time. To reduce this unwanted contamination, samples can be pre-cleaned in a plasma cleaner just prior to insertion in to the microscope.

Each of the spots in a diffraction pattern corresponds to diffraction of the incident beam at an angle θ to an atom plane under the condition that:

$$n\lambda = 2d_{hkl} \sin \theta \tag{4.1}$$

where n is an integer, λ is the wavelength of the electrons, θ is the angle of incidence of the electron beam to the atomic plane of Miller indices hkl, and d_{hkl} is the spacing between the hkl planes. This is termed Bragg's Law. Under this condition, there is constructive interference (addition) between the diffracted beams since the extra path length travelled by the diffracted electrons from each parallel plane is a whole number of wavelengths, Fig. 4.5.

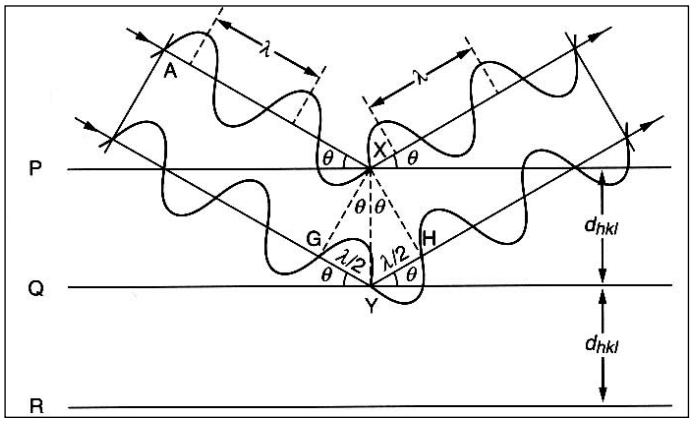


Figure 4.5: The Bragg equation. P, Q and R, are three successive parallel lattice planes (*hkl*) in a crystal. The incoming radiation of wavelength λ is incident on the planes of spacing d_{hkl} at a glancing angle θ and is reflected by the planes at an angle θ. The path difference between the rays reflected by planes P and Q is λ, which, by geometry, is equal to $2d \sin \theta$ [78].

The indexing of the diffraction spots from a given sample is determined using the equations given in Appendix A. The only additional information required is the camera length *L*, which relates to the magnification of the pattern, Figure 4.6. Use is normally made of a known polycrystalline film which yields diffraction rings instead of spots due to the many different oriented grains. This diffraction pattern is collected under identical conditions to that of the sample diffraction patterns. Using the expression,

$$Rd = \lambda L \tag{4.2}$$

where *R* is the radius of a given ring corresponding to diffraction from planes of Miller indices *hkl*, *d* is the spacing between these planes, and λ is the wavelength of the electrons the camera length *L* can be calculated. λL is termed the camera constant.

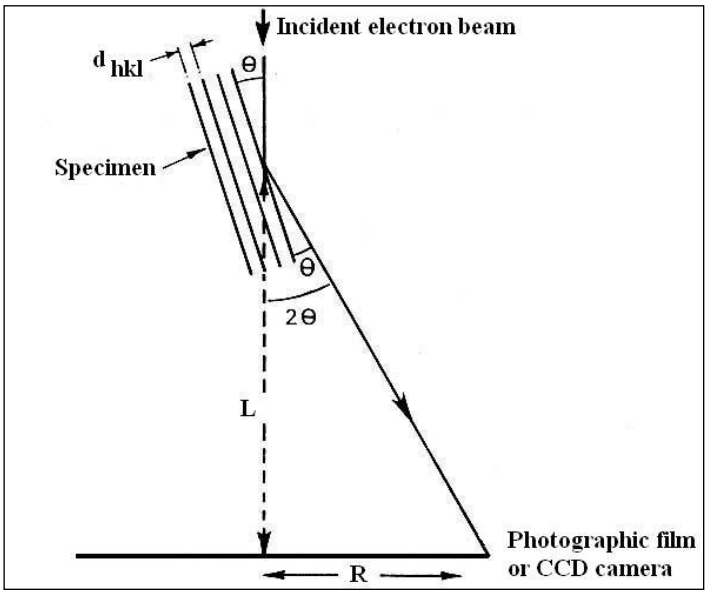


Figure 4.6: The TEM considered as a simple electron diffraction camera [79].

4.3 Ion milling

Ion milling is used to thin samples to perforation for TEM, either as the complete thinning process or as the final step. The process of ion milling is illustrated in Figure 4.7. Accelerated inert argon ions are incident at a shallow angle onto the sample and through ion-atom collisions cause sample atoms to be sputtered off the sample surface. Variables in ion milling are the angle of incidence of the argon beam onto the sample and the accelerating voltage of the ion beam. Compositional thinning during milling is reduced by making use of small

incident angles, typically 2 - 5^{o}, low accelerating voltages 2 - 6 keV and rotation of the sample.

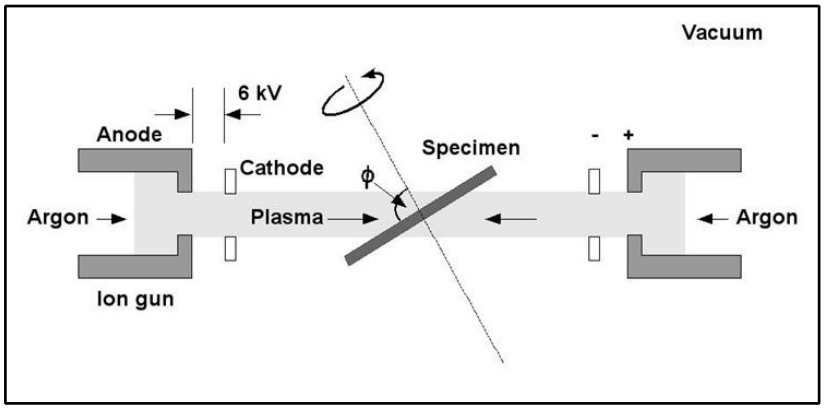


Figure 4.7: A schematic diagram of an ion beam TEM sample thinning device: Argon bleeds into an ionization chamber (ion gun) where a potential typically 2-6 keV creates an Ar ion beam incident onto an inclined rotating specimen [73].

Figure 4.8 illustrates a typical ion milled sample with a hole in the proximity of the region of interest where electron transparency occurs. Electron-specimen interaction in the electron transparent region enables characterization of the microstructure since the electrons can be manipulated in many different ways [81, 82] to provide information such as structural images, chemical composition and information on the local atomic environment [81, 83].

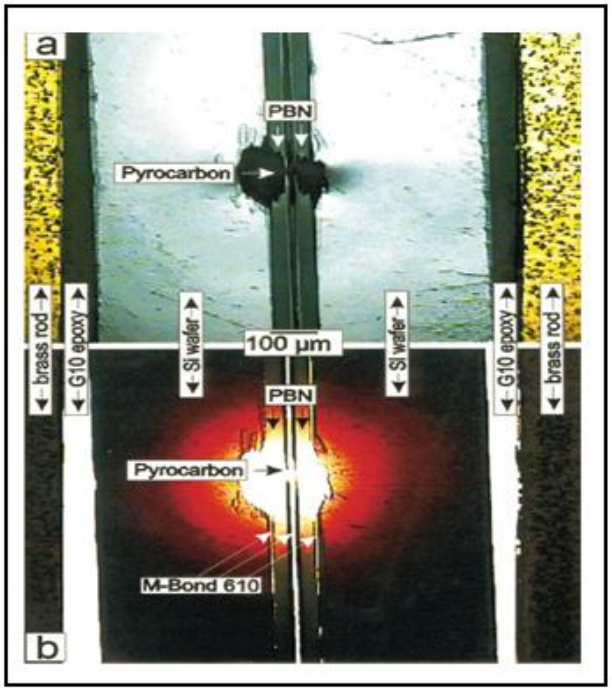


Figure 4.8: Light micrographs of the TEM sample prepared from dimpling followed by ion milling to achieve a small hole and electron transparent regions around it (a) reflected light and (b) transmitted light [84].

4.4 Energy Dispersive X-ray Analysis (EDX)

There are two types of x-rays generated by the electron beam when it interacts with a sample, Figure 4.9. The first is Bremsstrählung or "braking radiation" resulting from electrons that undergo deceleration in the coulombic field of the sample atom. Under these circumstances, the incident electron undergoes an interaction with the atom as a whole, changes direction and loses some energy which is given off as a photon of electromagnetic energy somewhere between zero and the original energy of the incident electron. Summing over all interactions, this forms a continuous background spectrum due to the random nature of the beam-sample interaction [76]. The second type of X-ray generated is characteristic radiation, Figure 4.9. This results from the direct, inelastic interaction between an incident electron and an orbital electron around the nucleus of the sample atom. The incident electron can transfer enough energy to eject the orbital electron out of its shell, thus leaving the shell with a vacancy. This vacancy can then be filled by an electron from an outer orbit. Since each shell and sub-shell of a given atom has a specific minimum energy to displace an electron, the critical ionization energy, and outer shells have a higher energy than inner shells, the electron filling the vacancy has too much energy and this excess energy is given off as an X-ray. The energy of this X-ray is characteristic of both the two shells (K,L,M etc.) involved in the transition and the element, Figure 4.10.

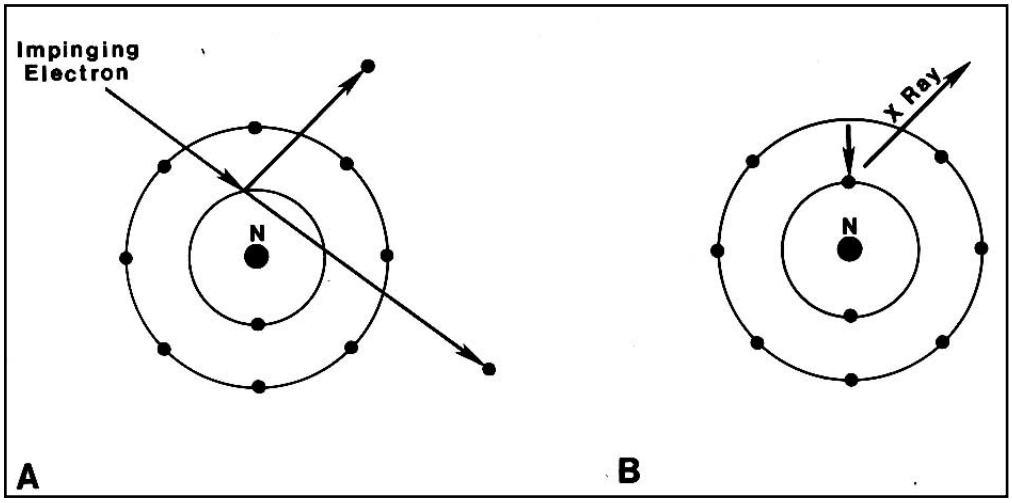


Figure 4.9: Schematic diagram of the generation of a characteristic X-ray. (A) shows an impinging electron removing a sample electron from the innermost shell orbit (K-shell), and (B) shows the vacancy being filled by an electron from the next outer shell (L-shell) with the subsequent generation of an X-ray. The resultant X-ray would be a K_α X-ray [76].

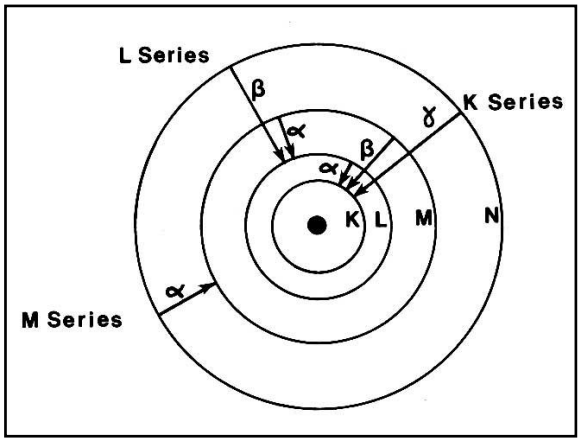


Figure 4.10: Schematic diagram of the spectrum of X-rays that may be generated from a single element. Since each shell actually comprises several energy levels, transitions are thus more numerous (and the nomenclature more complicated) than shown here [76].

The analyzing system disperses all the X-rays by their energy, hence the name of such analysis, so yielding a histogram of energy on the x-axis and number of X-ray counts on the y-axis. The characteristic X-rays result in peaks at specific energy positions superposed on the Bremsstrählung radiation. The area under the X-ray peaks is related to the composition of the sample. Since the X-ray detector does not depend on Bragg diffraction of X-rays to be incident on it at a mechanically set angle, a full spectrum of elemental analysis can be obtained simultaneously of a wide variety of elements.

4.5 X-Ray Diffraction (XRD)

X-ray diffraction (XRD) analysis makes use of the scattering effects of materials when an incident, collimated X-ray beam is focused onto them. Diffraction of the incident beam takes place due to the comparable order of the atomic distances between planes and the wavelength of the incident X-ray beam. Peaks are produced where the diffraction satisfies the Bragg condition (Eq. 4.1 and Figure 4.4).

The essential components of a typical X-ray diffractometer are:

- a source of X-rays, usually a sealed X-ray tube,

- a goniometer, which provides precise mechanical motions of the X-ray tube, specimen and detector,
- an X-ray detector,
- electronics for counting detector pulses in synchronization with the positions of the goniometer.

Typical data comprises a list of detector counts versus 2θ angle whose graph is a diffraction pattern. The angular positions of the peaks and intensities can be matched to standard files to identify the phases present.

A schematic diagram of the typical components in a "Bragg-Brentano" (also known as θ-2θ) geometry X-ray diffractometer is shown in Figure 4.11. Precise movements of the specimen and detector with respect to the X-ray source are provided by the goniometer. In practice, it is easier to keep the bulky X-ray source stationary, and to rotate the specimen by an angle θ. To ensure that the scattered X-rays leave the specimen at the angle θ, the detector must be rotated precisely by the angle 2θ. The goniometer may also provide for the rotation of the specimen in the plane of its surface by the angle ϕ, and in the plane of the goniometer by the angle ω. Normally, a line source is employed, which is narrow in the plane of the goniometer, but has a height of perhaps 1cm perpendicular to this plane. Slits are used to collimate both the incident and diffracted beams.

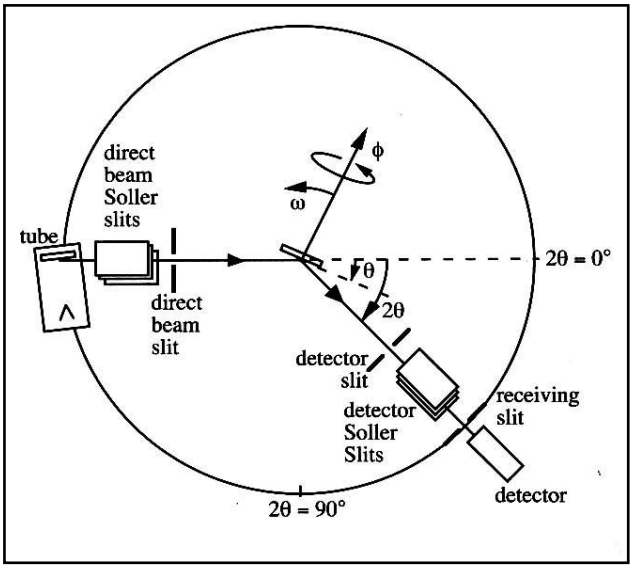


Figure 4.11: Schematic diagram of some typical components and angles of the goniometer for a θ-2θ X-ray diffractometer. The flat specimen is at the centre of the goniometer circle, whose radius is typically 0.25-0.5 m [85].

A divergent incident beam is a practical necessity for obtaining reasonable X-ray intensities at the detector. The advantage of the "Bragg-Brentano" geometry is that it gives well-defined diffraction angles for finite slit widths and beam divergences, Figure 4.12. In this goniometer, both the detector and X-ray tube are on the circumference of a "goniometer circle" with the specimen in the centre. Although the two rays in the diagram from the X-ray tube are incident at different angles to the specimen surface, if they pass through the detector slit they form the same angle, 180^{o}-2θ, at the specimen. This geometry results in the illumination of a reasonable area of the specimen surface, and many ray paths having the same scattering angle. Good intensity and good instrument resolution are obtained.

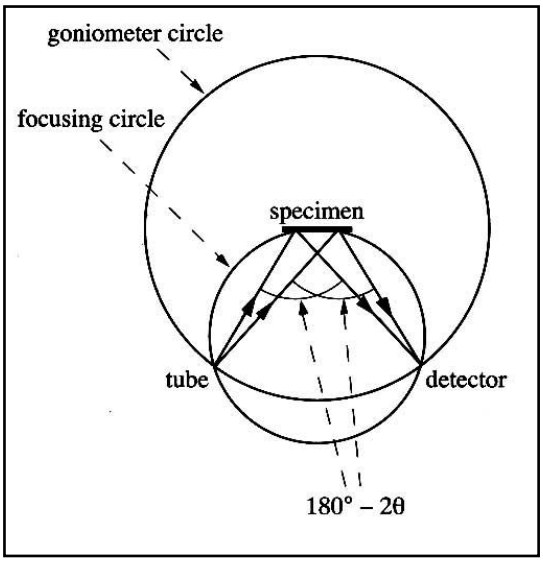


Figure 4.12: Geometry of a Bragg-Brentano diffractometer. The two angles at the specimen are the same 180^{o} - 2θ [85].

For the investigation of thin films on bulk material Glancing Incidence X-ray Diffraction (GIXRD), Figure 4.13, is more appropriate. As its name suggests, GIXRD employs low angle of incident X-rays to the sample surface, and as a result only a shallow depth of penetration into the sample surface film is achieved and probed without interference from the bulk material [78]. In addition, the low angle of incidence provides for a long beam path in the surface film and hence yields a higher X-ray signal from the surface film. Since the geometry for GIXRD is only a slight modification of that for "Bragg-Brentano", the same principles of diffraction hold for the two geometries.

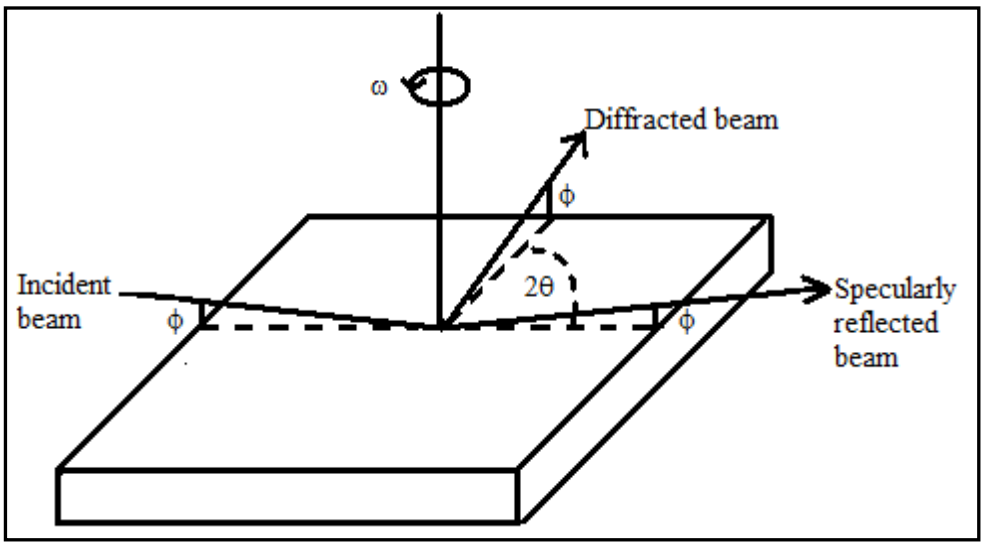


Figure 4.13: Schematic diagram showing Glancing Incidence X-ray Diffraction for surface films [86].

CHAPTER 5

Experimental procedure

5.1 The material

The alloy material studied was an experimental nickel-based superalloy TMS-75 whose composition is given in Table 5.1 below. For comparison purposes, the compositions of three commercial alloys of similar composition are also given. The TMS-75 alloy was supplied as a single-crystal rod of 10 mm radius from the National Institute for Materials Science (NIMS), Japan.

Table 5.1: Compositions in at. % of the experimental alloy TMS-75 and for comparison close composition commercial alloys CMSX-2, CMSX-4 and CMSX-10.

	Ni	Cr	Co	Al	Ta	W	Re	Mo	Hf	Ti	C	Y	S(ppm)
CMSX-2	65.40	9.00	5.00	12.50	2.00	2.50	-	0.40	-	1.20	-	-	-
CMSX-4	63.70	7.60	9.30	12.60	2.20	2.00	1.00	0.40	0.100	1.00	-	-	-
CMSX-10	Bal.	2.40	3.20	13.20	2.03	2.80	2.00	0.30	<0.1	-	-	-	-
TMS-75	63.07	3.57	12.57	13.75	2.05	2.02	1.66	1.29	0.035	-	-	-	-

5.2 Sample preparation

The sample preparation was undertaken in two stages: the samples were first prepared for scanning electron microscopy and oxidation treatment, and then for XRD and transmission electron microscopy, the latter requiring the preparation of cross-sectional samples.

5.2.1 Sectioning

The first sample preparation step involved cutting the (001) orientation rod into 1 mm thick slices using a Buehler Isomet Low Speed Saw with a 300 μm thick diamond tipped blade.

5.2.2 Mechanical polishing

To prepare the samples for oxidation, the sample slices were consecutively ground using 600-grit, 1000-grit and 2500-grit SiC paper, the samples being ultrasonically degreased in acetone, then ethanol between each grit size polishing step. The grinding stage was followed by mechanical polishing of the samples using pastes with a 6 μm, 3 μm, 1 μm and finally 0.25 μm diamond suspension, respectively, in order to produce a flat, unoxidised planar sample surface with minimal surface roughness. Degreasing again was utilized after each polishing step.

Characterization of the surface roughness and the effectiveness of each polishing step were carried out on a macro scale using a JEOL JSM-840 scanning electron microscope (SEM).

Figure 5.1 shows the planar SEM backscattered (BSE) image of the internal structure of the polished TMS-75 surface before oxidation.

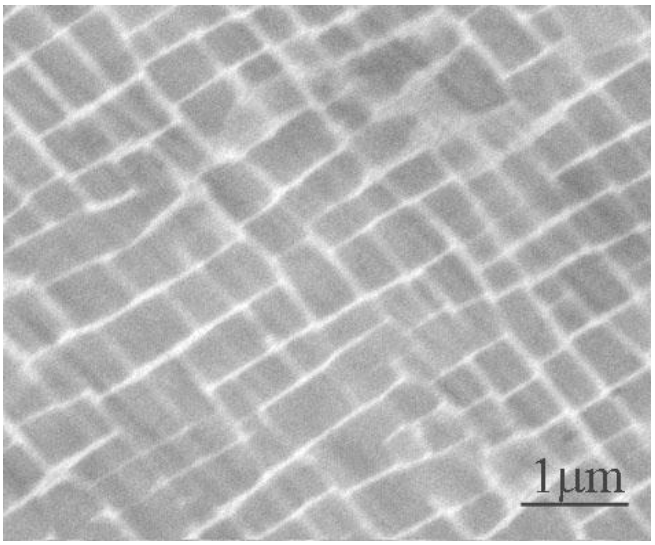


Figure 5.1: SEM electron backscattered image of a TMS-75 surface polished down to 0.25 μm prior to oxidation.

5.2.3 Sample oxidation

The polished samples were individually oxidized in static laboratory air at 900^{o}C. Each sample was introduced into the tube furnace at the desired oxidizing temperature and removed at temperature and allowed to cool down in air. The oxidation time was 100 h. The temperature and time were chosen to be equivalent to the heat treatment required to obtain the correct microstructure.

5.2.4 Transmission electron microscopy sample preparation

The preparation of samples for cross-sectional TEM analyses was undertaken as proposed by Strecker *et al.* [87]. The first step in the TEM sample preparation involved cutting each sample in half and adjoining the cut oxidized faces together using MBond 610 epoxy glue as shown in Figure 5.2. The glue was cured in air at 150^{o}C for two hours.

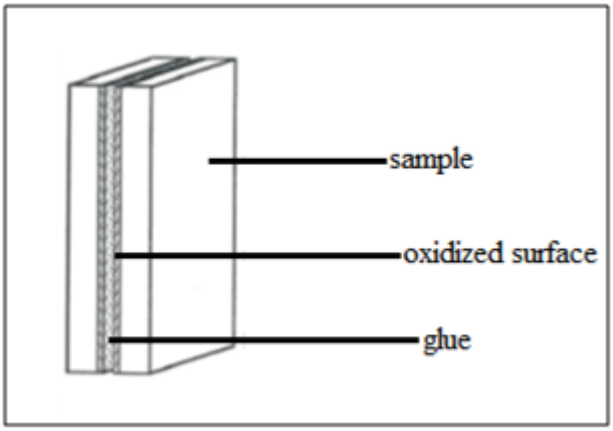


Figure 5.2: Schematic diagram of the glued oxidized sample.

The glued samples were ground on both sides equally to yield a 600 µm thick slab thin enough to fit into the slot cut in a 2.3 mm diameter brass rod. The rod was then epoxied into a brass tube of outside diameter 3.05 mm as shown in Figure 5.3. The epoxy was again cured at 150^{o}C for two hours. Subsequent to this, the tube encasing the sample was sectioned with a wire saw into discs of 400 mm thickness as shown in Figure 5.4.

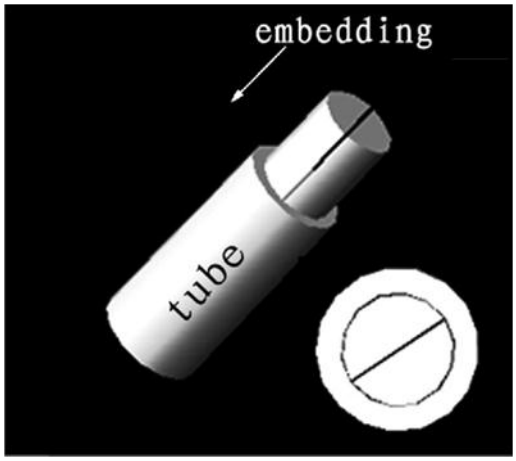


Figure 5.3: Embedding of the sample into brass tubing. The two oxidized surfaces were glued and ground to fit into the 600 µm groove of the inner rod [88].

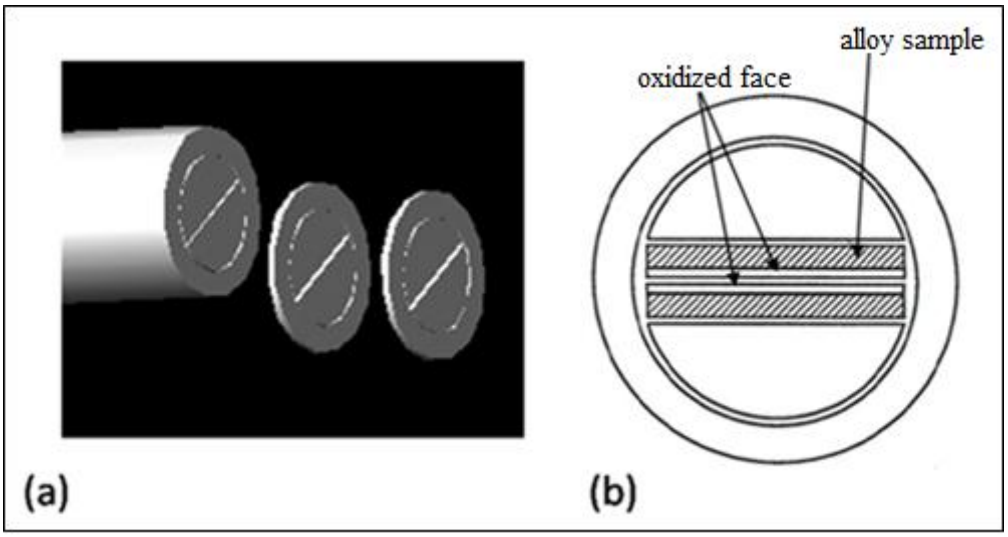


Figure 5.4: (a) Cutting of the sample embedded in the brass rod and tubing into thin discs, (b) planar view of an embedded sample in a brass disc ready to be dimpled [88].

5.2.5 Sample dimpling

After the embedded sample discs, Figure 5.4, were ground on both sides on a 15 µm diamond pad down to a thickness of 100 µm, they underwent dimpling as the last abrasive pre-thinning step. The aim of dimpling was to create a specific area in the sample, normally near the centre, and containing the interface between the two glued oxidized sample faces, where the thickness was approximately 20 µm and on which subsequent ion milling could be carried out. This procedure thus considerably shortens the final ion milling time.

Dimpling was carried out on both sides of the sample disc with the dimpled regions on the two sides aligned with each other. Figure 5.5 is an illustration of how the samples were dimpled. Double-sided dimpling was used as a result of a number of advantages which it has over dimpling from one side. These advantages are [88]:

- The chances of specimen bending from residual strain are minimized due to symmetry in surface damage and the resulting strain.
- The same depth can be achieved on both sides thus making both of the sides of the sample workable, independent of the direction of specimen mounting.
- Dimpling on both sides makes the dimple depth less, which also lowers the angle of incidence at which ion milling can be carried out, so reducing the ion damage depth into the sample, while also reducing the surface roughness.

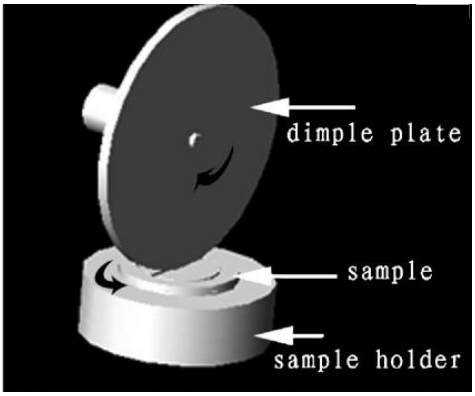


Figure 5.5: Sample dimpling in which both the dimple plate or wheel and the sample holder rotate [89].

Dimpling was carried out using a Gatan Model 656 Dimple Grinder. The grinding stage was carried out using a phosphor bronze wheel utilizing a load of 10 g and a speed of 2 rpm. Diamond paste of 6 µm, 3 µm and then 1 µm were employed for the dimpling. On completion, the surface was cleaned with ethanol. Dimple grinding was followed by polishing, which involved replacing the dimpling wheel with a felt pad and polishing the dimpled area using a 0.05 µm alumina suspension for 2-3 minutes. The polishing load and speed were 15 g and 5 rpm. This procedure was carried out on both sides of the sample, with final cleaning in ethanol.

5.2.6 Ion milling

The ion milling was carried out in a Gatan Precision Ion Polishing System (PIPS) employing two miniature Penning ion guns (PIGS). Initial argon ion thinning was undertaken for 5 hours at 5 keV at an angle of incidence to the sample surface of 5^{o}, followed by thinning to perforation at 4 keV at an angle of 4.5^{o}. Once a hole was produced, a final thinning at 2.5 keV and at an angle of 4.5^{o} for 5 minutes was used to reduce the depth of the surface ion damage.

5.3 Scanning electron microscopy

The quality of polishing was studied using secondary electron images (SEI) in a JEOL JSM-840 SEM operating at 10 keV. A FEI NanoSEM was utilized at 20 keV to obtain the planar view of the surface internal structure using backscattered electrons (BSE).

5.4 Transmission electron microscopy

All the transmission electron microscopy and X-ray analyses were undertaken in a Philips CM200 TEM operating at 197 keV using a LaB_6 electron source. X-ray analyses utilized an Oxford INCA energy dispersive X-ray detector (EDX) with an ultra-thin window. The sample was located in a FEI double tilt (usable $\pm 38^{o}$, $\pm 28^{o}$) analysis holder having a beryllium sample cup to reduce spurious X-rays. Liquid nitrogen cooling of the anti-contaminator was always employed in order to reduce carbon contamination onto the sample. In addition, immediately prior to viewing, the samples were pre-cleaned for four hours in the TEM sample holder in a 25% oxygen/75% argon atmosphere in a low energy Gatan Plasma Cleaner. The majority of the TEM images were recorded on a post column Gatan 678 Tridiem Imaging Filter (GIF). The remainder of the images and all the diffraction patterns were captured on high speed Kodak SO-163 photographic film.

The diffraction camera length calibration for each matrix and precipitate pattern was determined using the (600) diffraction ring, the outer of the doublet in Figure 5.6, from an aluminum fine grained polycrystalline sample. The procedure utilized was to take the precipitate and the matrix micro-diffraction patterns using a nanometer sized probe under the same conditions, and the combined matrix and precipitate diffraction patterns under

essentially the same conditions, except for the probe size being expanded to cover both regions. The lens currents and stage co-ordinates were saved on the microscope computer. With both the electron beam and high voltage remaining on, the sample was removed and replaced with the thin film calibration specimen. The calibration sample was then bought into image focus solely by using the height (Z) adjustment of the stage, that is, without changing the lens settings. A selected area diffraction pattern was then recorded requiring only a readjustment of the condenser lens for an expanded beam and lower intensity condition as a result of the thin film utilized and a very slight readjustment of the diffraction lens to regain sharp diffraction focus.

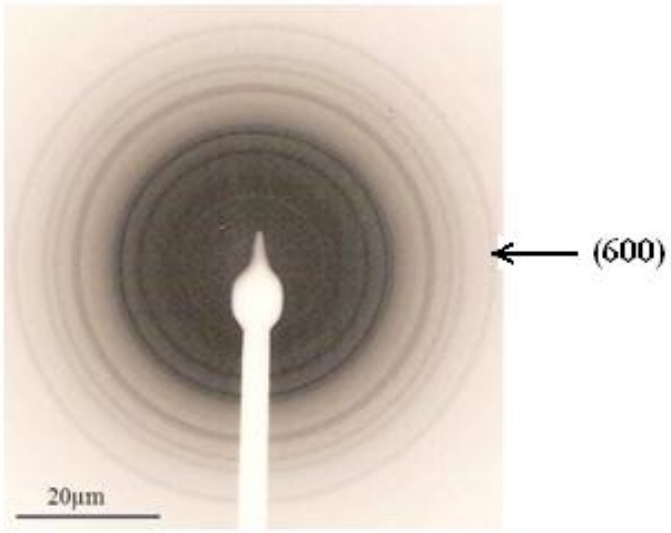


Figure 5.6: Electron diffraction pattern from an aluminum thin foil showing the (600) ring, the outer of the doublet, used as a standard to calculate the camera constant λL.

Each diffraction *hkl* spot spacing, R, was measured over a number of multiple spacings and then averaged. The measurements were made with a travelling microscope with an accuracy of about 0.01-0.02 mm. Angular spacing between different *hkl* planes were measured with a protractor with an accuracy of typically 0.5-1^{o}. Each diffraction pattern was indexed using at least five different *hkl* planes.

The WebEMAPS software package [90] was used to generate different zone axis diffraction patterns for both the matrix and the precipitate, given in Appendix D, in order to confirm the manually calculated results obtained using the equations in Appendices B and C. It should be noted that the diffraction patterns are generated using kinematical theory and are only useful

in a quantitative way. Kinematical theory is only valid for thin specimens up to about 50 nm thick such that each incident electron is only scattered by one atom. The effect of absorption can only be adequately treated by dynamical theory of diffraction. In this case, electrons in the diffracted beam can be scattered back into the forward direction and multiple scattering can occur. The effect of this is to change the intensities of the diffracted beams. This is why in some cases in Appendix D the intensities differ from the experimental patterns. What is important is the positions of the diffracted beams and their inter-relationship in the pattern.

5.5 X-ray diffraction

Bulk analysis of the material using large angles of incidence was undertaken on a PANalytical PW1710 Reflection Diffractometer using copper K_α radiation and a voltage of 40 keV. Diffraction spectra were obtained for 2θ angles in the range 10^o to 80^o using a step size $0.02^o\ s^{-1}$.

Surface type analysis of the oxidized samples to determine phase variations with depth using Glancing Incidence X-ray Diffraction were carried out on a Bruker D8 Advance X-Ray Diffractometer using copper K_α radiation and a voltage of 40 keV. Data acquisition involved projecting a beam collimated by a 600 μm slit onto the surface of the sample at angle of 1^o. Incidence angles lower than 1^o were not utilized, since the beam could strike the sides of the specimen holder. A step size of $0.043^o\ s^{-1}$ was used to obtain the cumulative diffraction spectra for 2θ angles in the range 30^o to 80^o. This procedure was carried out for each abrasive step until the internal oxidation region had been cleared. Abrasion was carried out using SiC paper, each abrasion step being targeted to remove a depth of approximately 6 μm of material. The peak matching was undertaken using Diffrac plus Eva, Copyright © Bruker-AXS 1996-2010.

CHAPTER 6

Results and Discussion

This chapter presents the experimental results from the work carried out to investigate the internal oxidation behaviour of the alloy, TMS-75 following its oxidation at 900^{o}C. The first section of the chapter focuses on the XRD data of the unoxidized material as well as the oxidized alloy with depth. The θ-2θ coplanar Bragg-Brentano diffraction pattern was considered first. This diffraction encompasses phase information over a range of depths since the angle of incidence is large and thus so is the beam penetration depth. Subsequently, an investigation of the various phases was carried out with glancing angle incidence x-ray diffraction. Nominal 6 μm sequences of polishing steps were utilized to obtain this information at different depths into the material. Internal oxides, orientation relationships and compositional analyses are subsequently discussed. Internal oxides were identified through cross-sectional TEM analysis, while orientation relationships were determined through both selected area diffraction and microdiffraction.

6.1 X-ray diffraction

Although in-situ high temperature XRD is normally employed to investigate the evolution of the crystalline phases present in the oxide scale as function of oxidation time [91, 92, 93, 94], in the present case, the process was considered unnecessarily expensive to be utilized since the aim was only to identify the internal oxidation products at one particular temperature and oxidation time.

The XRD patterns were studied through utilizing the EVA software package obtained with the Glancing Incident X-ray Diffraction Angle system, peak matching, considering other possible phases through the input of all the elements present in the alloy, and considering possible phases resulting from their oxidation in air. Subsequently, some phases such as $CrTa_4O_6$, $NiTa_4O_6$, $CrWO_4$, $AlTaO_4$ and ReO_3 were discarded solely for XRD identification purposes since their percentage concentrations would have meant that their peaks would be hidden within the background radiation level and thus they would not be detectable.

The diffraction pattern obtained from the θ-2θ Bragg-Brentano XRD of the polished unoxidized alloy, Figure 6.1, confirmed the single crystal nature of the unoxidized material. The phase identification of the alloy matched well with the Ni_3Al phase, that is, the γ´-phase. No additional peaks were observed in the 2θ range 10 - 30^o. The highest peak was identified from both simulation [95] and experiment [96] as originating from the (002) plane, while the minor peaks corresponded well with the (110) and (111) planes. However, considering the diffraction angles for these peaks and comparing them to those of Wilde and Grant [95], a shift of the order of 1^o to 2^o was observed. This shift could be accounted for by the other elements in the alloy being soluble in the γ´ phase and thus changing its lattice parameter and diffraction peak positions. It should be noted that the shoulder on low angle side of the major (002) peak is an artifact resulting from aberrations in the diffractometer optics and from the use of filters rather than a monochromator. The unoxidized diffraction pattern set the baseline to which the oxidation diffraction studies and phase changes were correlated.

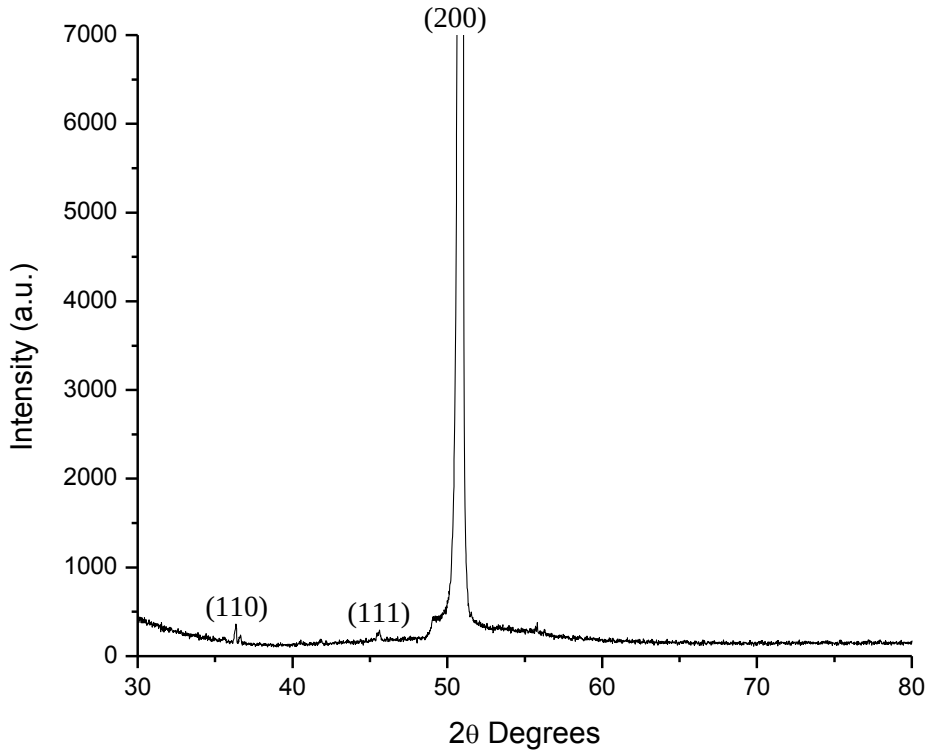


Figure 6.1: Bragg-Brentano XRD diffraction pattern obtained from an unoxidized single crystal TMS-75 surface revealing a preferred (200) orientation which is identical to (001) orientation for a fcc structure.

Figure 6.2 is the diffraction pattern obtained from the θ-2θ Bragg-Brentano XRD of the alloy oxidized for 100 h at 900°C. Immediately of note is the fact that the major peak lies at a completely different position, some eight degrees less than that found for the unoxidized surface, Figure 6.1. Using the EVA analyzing software and peak matching, and the XRD ICSD resource at Karlsruhe [97] the phases identified were (Ni,Co)O being the major peak, Ni_3Al now becoming a minor peak, Al_2O_3 and Ta_2O_5.

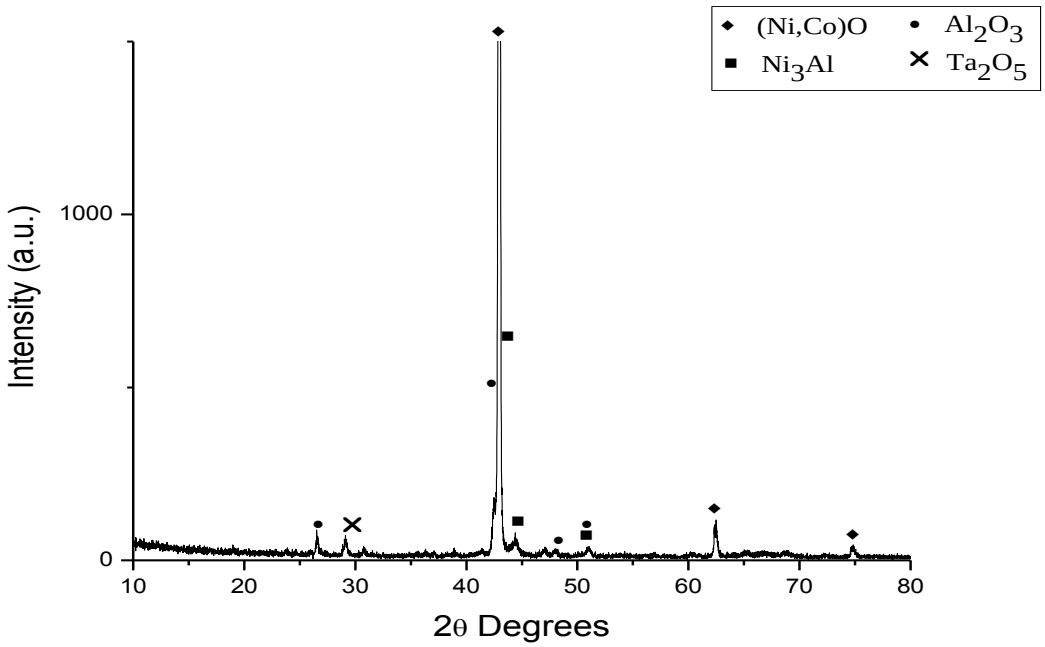


Figure 6.2: Bragg-Brentano XRD diffraction pattern obtained from the sample after oxidation in air for 100 h at 900°C.

Figure 6.3 compares the diffraction patterns obtained from the unoxidized alloy and the oxidized material. The misalignment of the (Ni,Co)O major peaks is either due to solid solution effects or a slight discrepancy of a few degrees resulting from sample positioning in the two X-ray diffraction systems used. In spite of the difference caused by the different information depths that the Glancing Incident X-ray Diffraction Angle and θ-2θ Bragg-Brentano XRD patterns originate, the oxide patterns are consistent with Al_2O_3 appearing to show prominence below the surface external scale and upper internal reaction zone region.

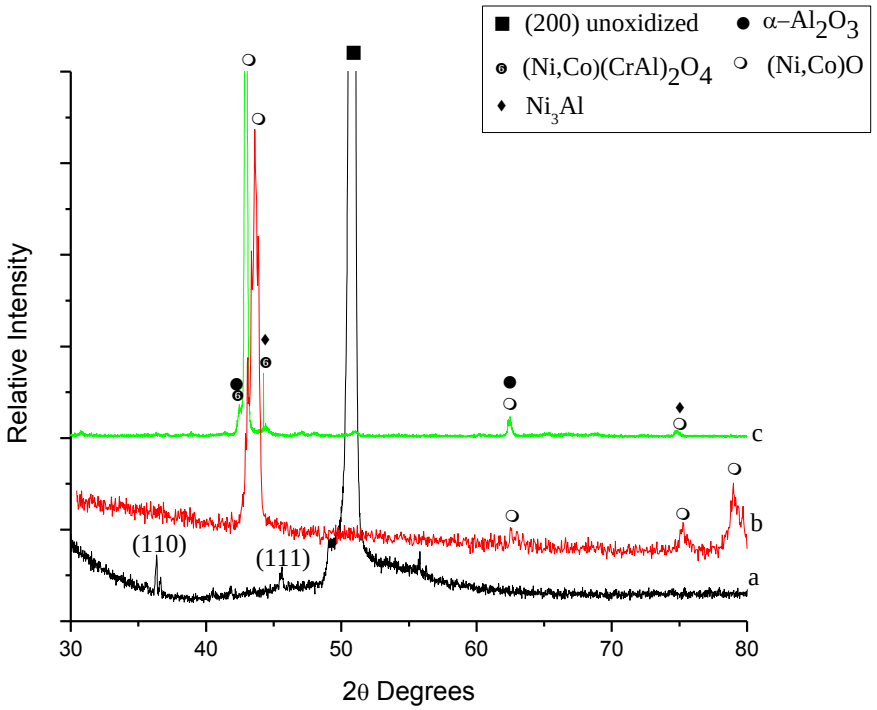


Figure 6.3: Comparison of the diffraction patterns observed from (a) the unoxidized TMS-75 alloy surface, (b) oxidized TMS-75 surface using GIXRD, and (c) the oxidized TMS-75 surface using Bragg-Brentano diffractometry.

To study the internal oxidation closer, a series of GIXRD patterns were obtained as a function of depth into the sample, a new spectrum being collected after each approximate 6 µm deep polishing step. The results are displayed in Figure 6.4 in the 2θ range of 30 - 80°, there being no additional peaks in the 2θ range 10 - 30°, and in Figure 6.5 for a more detailed study over an expanded 2θ range of 30 - 45°. At each analysis point, the X-ray sampling depth at an angle of incidence of 1° would be greater than 20 µm.

The diffractograms in Figures 6.4 and 6.5 showed only relatively small variations as the oxidation zone was penetrated, but appearances and disappearance of different phases can be seen within this region with depth. The size of the variations in peak heights can be attributed to the depth of the incident X-ray penetration and the limited contribution from the low volume fraction of discrete internal precipitates. Although GIXRD can be considered to be rather more applicable to cases where thin films are concerned [93, 94], especially where they occur in lamellar structures, or alternatively in *in-situ* x-ray diffraction studies [81, 86, 89], the diffraction patterns especially for the limited 2θ range of 30 - 45° did provide some interesting insights to the changing structure with depth.

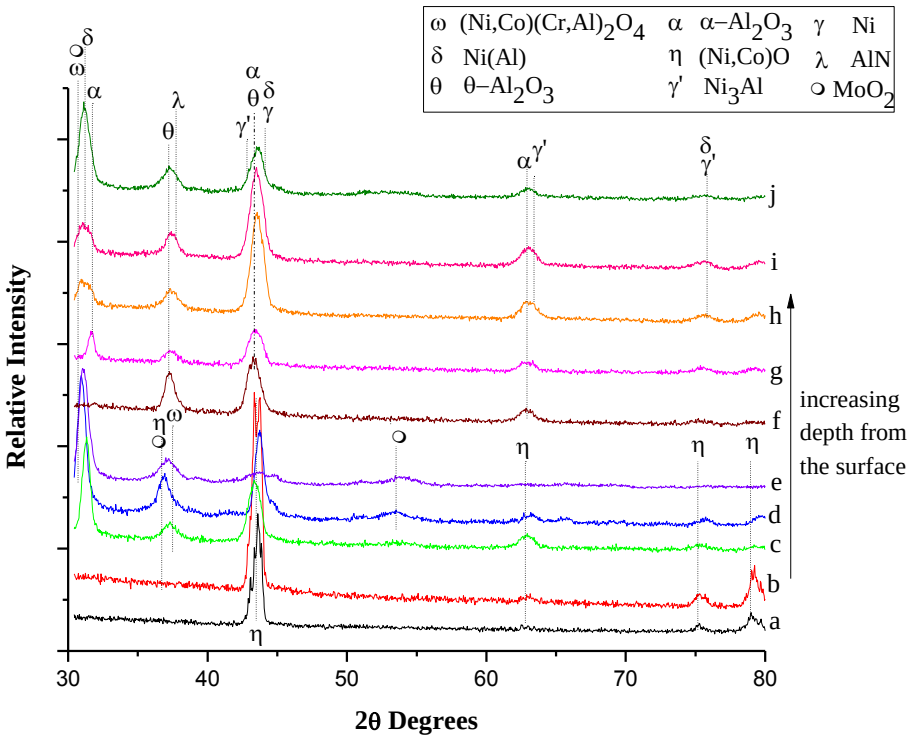


Figure 6.4: GIXRD diffractograms recorded after each nominal 6 µm depth of material had been removed by polishing from the TMS-75 alloy, previously oxidized for 100 h at 900°C, "a" was the first analysis on the as oxidized, unpolished surface.

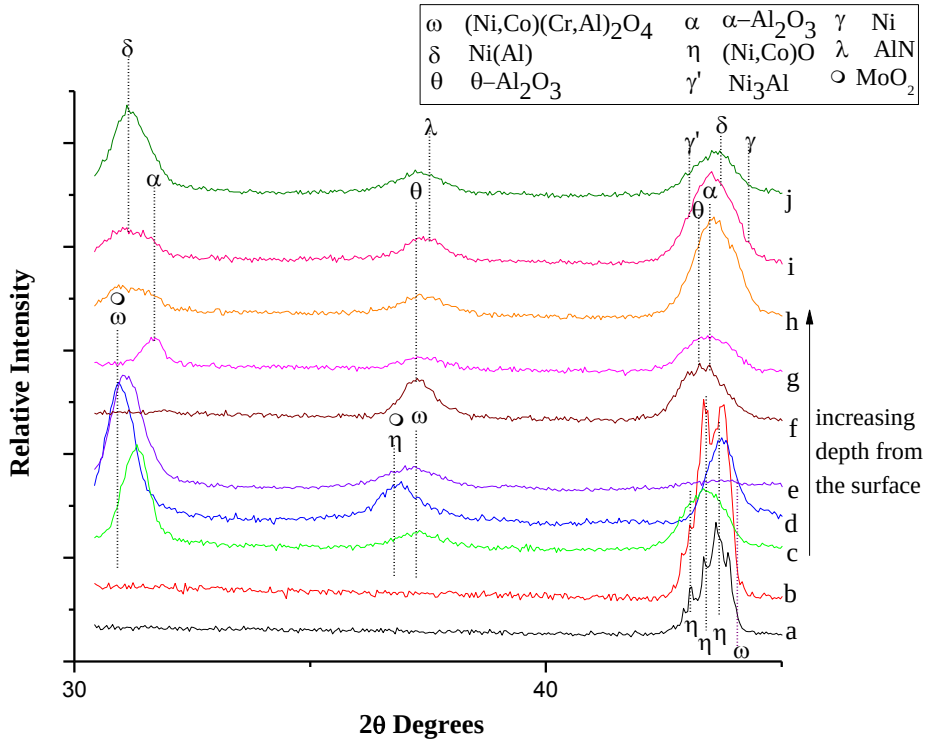


Figure 6.5: Expanded GIXRD diffractograms recorded after each nominal 6 µm depth of material had been removed by polishing from the TMS-75 alloy, previously oxidized for 100 h at 900°C, "a" was the first analysis on the as oxidized, unpolished surface.

(NiCo)O is indicated to be the major outer scale component, see diffraction patterns (a) to (d), and to occur to a thickness of about 20 µm. This layer is then followed by an intermediate region around 4 µm in depth with a mixture of (Ni,Co)O, $(Ni,Co)(Cr,Al)_2O_4$, MoO_2 and and Ta_2O_5. From about diffraction pattern (f) inwards for about 20 µm, a region containing θ-Al_2O_3, α-Al_2O_3 and AlN phases is indicated to be present. The original γ-γ' phase structure then resumes from about diffraction pattern (j), at a depth of around 44 µm, inwards.

6.2 TEM imaging and electron diffraction analysis

Figure 6.6 illustrates a representative TEM micrograph from the fine structure zone immediately underlying the external oxide scale. A fine grain structure with precipitates in the range 20nm to about 200nm diameter can be seen. An associated EDX spectrum from this region, Figure 6.7, reveals the ingression of oxygen through the external scale into the alloy with the formation of spinel oxide structures. A marked increase in Al and all the refractory elements (Cr, Ta, W, Mo and Re) was noted in this region.

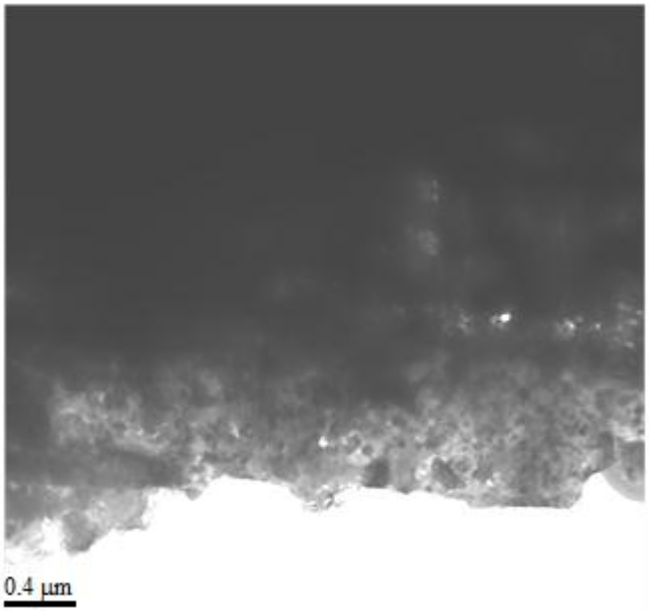


Figure 6.6: Cross-sectional bright field TEM image of the fine structure zone showing small oxide precipitates and grains in the TMS-75 superalloy after 100 h oxidation in air at 900^{o}C.

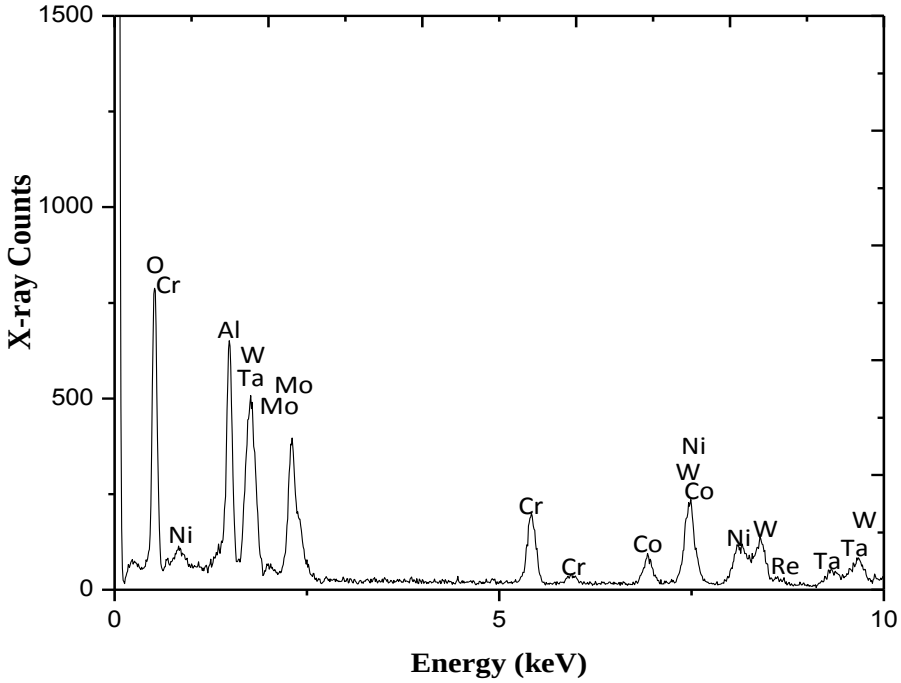


Figure 6.7: EDX spectrum of the topmost region of the fine structure zone shown in Figure 6.6.

Figures 6.8 and 6.9 respectively show a representative micrograph and associated EDX spectrum of the coarser grained fine structure region just below that shown in Figure 6.7. In marked contrast to Figure 6.7, the dominance of a chromium based oxide can be seen with the area showing, in particular, increased tungsten content, but with similar concentrations of the other refractory elements found in the region above.

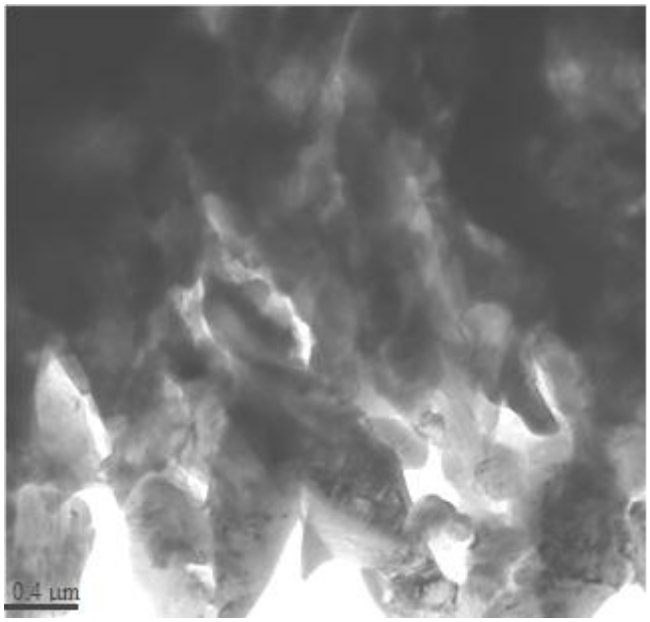


Figure 6.8: Cross-sectional bright field TEM image of the relatively coarse grained region with precipitates below the area shown in Figure 6.6, of the TMS-75 superalloy after 100 h oxidation in air at 900^{o}C.

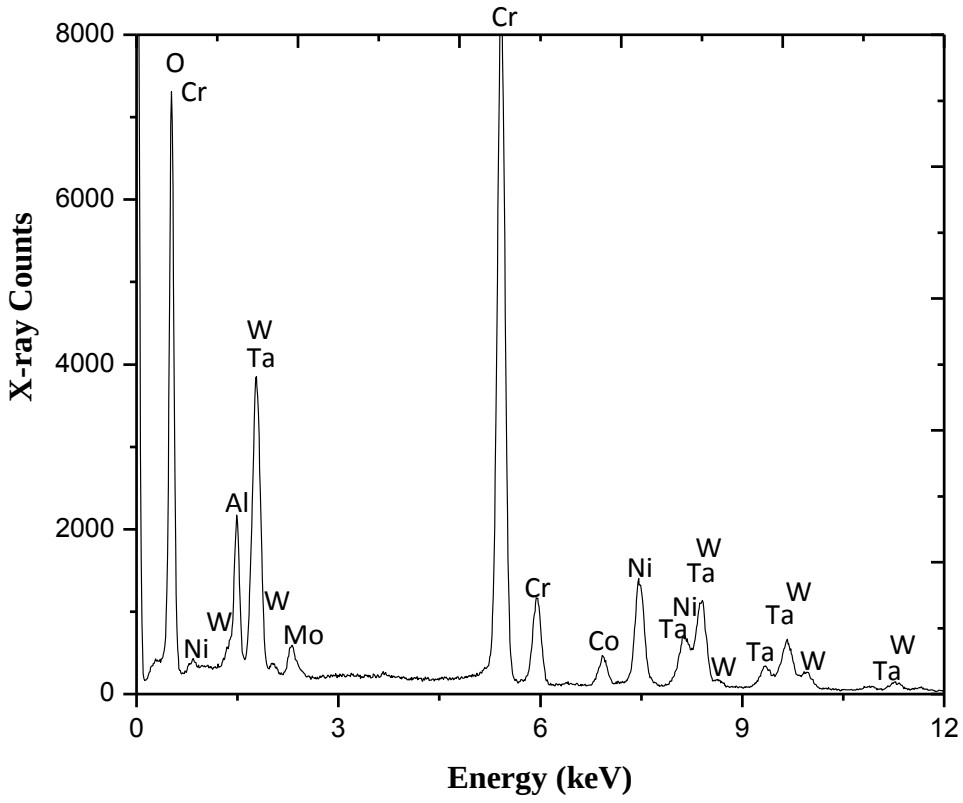


Figure 6.9: A typical EDX spectrum collected from the region shown in Figure. 6.8.

Representative images and analyses of some of the precipitates found within the internal reaction or oxidation zone now follow. Typically, at least five different diffraction spots in each pattern were utilized. This is also true for all the diffraction patterns in this chapter. In each case, the planar spacings, R, and the angles between planes measured on the diffraction patterns, were compared to those calculated using the equations in Appendices B and C. The indexing of the diffraction spots is completely arbitrary for the first zone axis only until the first two spots are indexed; these then determine the *hkl* values of the other diffraction spots as well as those in subsequent zone axes obtained when the same precipitate is tilted. Thus, different *hkl* values are possible for the same zone axis (*uvw*) depending on the initial two arbitrarily chosen *hkl* values. This is why for the same zone axis the experimentally-determined and simulated diffraction patterns can have different *hkl* values for the same diffraction spots. However, what is essential for the identification of the zone axis is that the planar spacings (separation of the diffraction spots) and angles between the planes (angles between rows of diffraction spots) are the same for the two indexing systems. The procedure adopted was to solve the first pattern for a structure, or structures, to determine the possible initial zone axis, then to try to index the rest of the sequence of zone axes. This always resulted in only one structure being possible. Subsequently, simulation of these zone axes was undertaken for that structure for confirmation. In practice, at least three different zone axis diffraction patterns were utilized to provide absolute confirmation of the structure type, but for brevity, only one experimentally obtained and the corresponding simulated zone axis pattern is shown. The contrast of the diffraction patterns has been reversed to permit easier recognition.

Figure 6.10 is a TEM micrograph of platelet shaped precipitates labelled A and B slightly further into the internal reaction zone than the region shown in Figure 6.8. Figure 6.11 displays the EDX spectrum obtained from precipitate A indicating an aluminium nitride phase. The diffraction pattern of the matrix region in close proximity with the precipitate A is shown in Figure 6.12(a), while that for the precipitate is given in Figure 6.12(b). While a combined diffraction pattern of the precipitate and matrix was taken, it is not shown here or for some other precipitates elsewhere in the dissertation for clarity since none of the zone axes of the precipitate and matrix were found to be parallel, being misaligned by 2 - 7^{o}. However, the two diffraction patterns here have been aligned as best possible here to show their correspondence. Various nitride structures were tested, the only one that satisfied this and other zone axes was for AlN (hexagonal, a = 3.111 Å, c = 4.978 Å, space group $P63mc$, no. 186) the surrounding matrix structure was found to be disordered Ni – solid solution (cubic *a*

= 3.5238 Å, space group *Fm*3*m*, no. 225) [98]. For clarity, Table 6.1 and 6.2 refer to only some of the measurements taken from the matrix and precipitate diffraction patterns shown in Figures 6.12. Within experimental error, a good fit can be seen in Tables 6.1 and 6.2. The matrix and precipitate diffraction patterns are shown indexed in Figures 6.13(a) and Fig. 6.13(b) respectively. The simulated diffraction pattern for this structure shown in Appendix D is consistent with the ratio of different planar spacings and angles between planes for this zone axis.

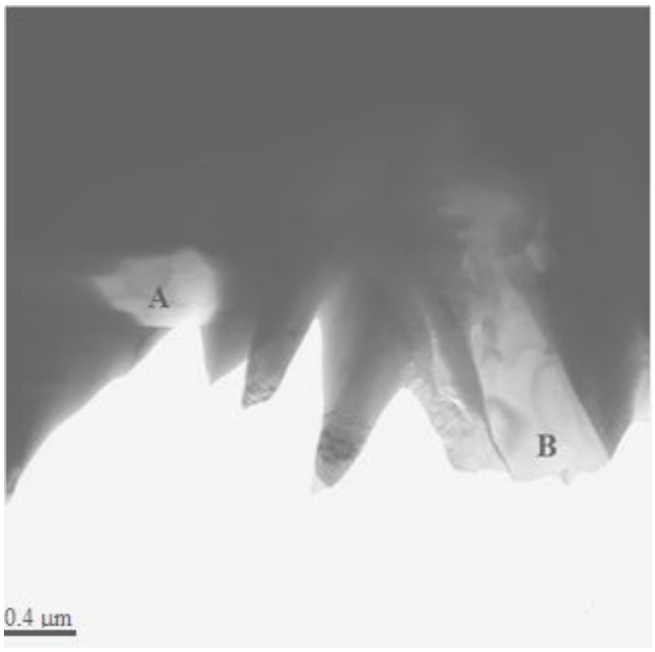


Figure 6.10: Cross-sectional bright field TEM image of the internal oxidation zone revealing precipitates A and B in the TMS-75 superalloy after 100 h oxidation in air at 900^{o}C.

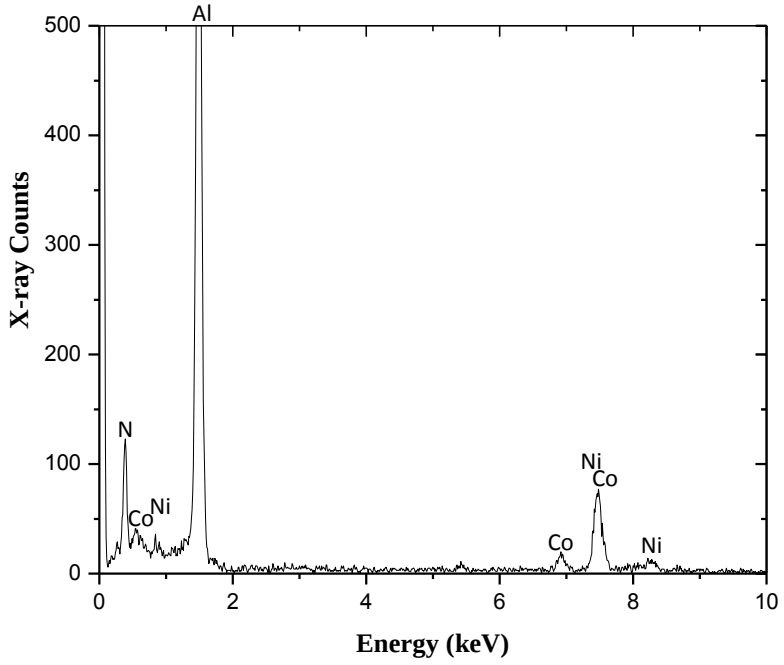
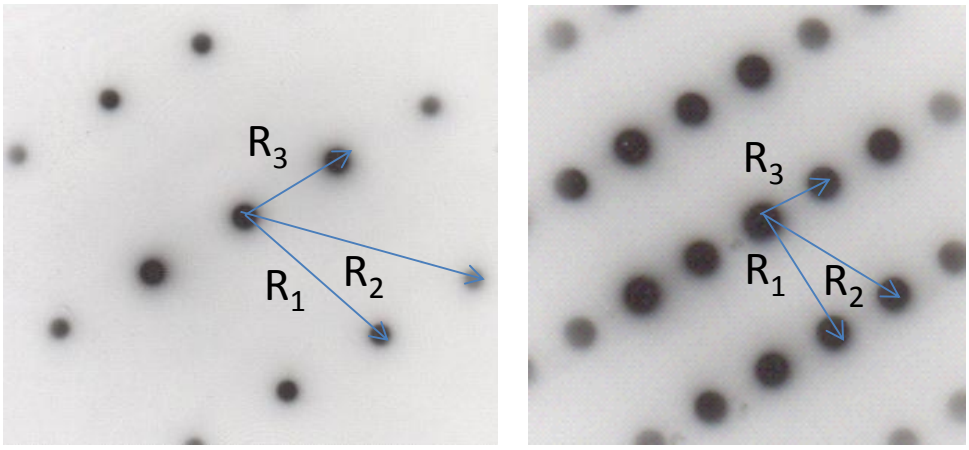


Figure 6.11: EDX spectrum from precipitate A in Figure. 6.10.



a **b**

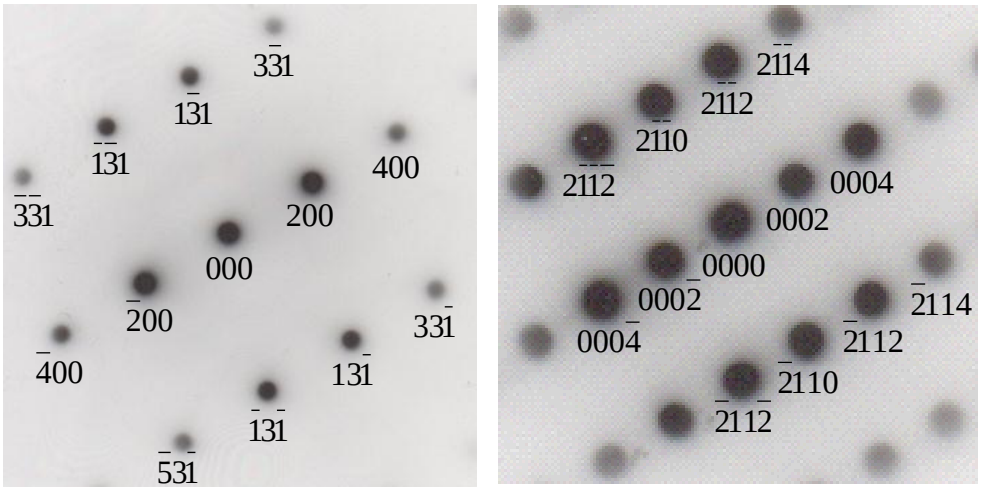
Figure 6.12: Electron diffraction patterns of (a) matrix and (b) precipitate A in Figure 6.10.

Table 6.1: Values of spacing R, d_{hkl}, *hkl* and θ for the matrix pattern in Figure 6.12(a).

	$r_{measured}$ (mm)	$r_{calculated}$ (mm)	d_{hkl} (Å)	*hkl*	$\theta_{measured}$	$\theta_{calculated}$
R_1	15.3	15.3	1.063	$\bar{1}3\bar{1}$	$1\bar{3}1\hat{}3\bar{3}1$ 35°	$1\bar{3}1\hat{}3\bar{3}1$ 35°
R_2	15.3	15.3	1.063	$13\bar{1}$		
R_3	9.3	9.2	1.751	200	$3\bar{3}1\hat{}200$ 72°	$3\bar{3}1\hat{}200$ 72°

Table 6.2: Values of spacing R, d_{hkl}, *hkl* and θ for the precipitate A in Figure 6.12(b).

	$r_{measured}$ (mm)	$r_{calculated}$ (mm)	d_{hkl} (Å)	*hkil*	$\theta_{measured}$	$\theta_{calculated}$
R_1	6.1	6.0	2.690	$\bar{2}110$	$\bar{2}110 \wedge \bar{2}112$ 30°	$\bar{2}110 \wedge \bar{2}112$ 29°
R_2	6.5	6.5	2.489	$\bar{2}112$		
R_3	3.3	3.3	4.975	0002	$\bar{2}112 \wedge 0002$ 60°	$\bar{2}112 \wedge 0002$ 62°



a **b**

Figure 6.13: Indexed diffraction pattern of (a) matrix [013] (compare with simulation Appendix D: Figure D1) and (b) precipitate A [$12\bar{3}0$] (compare with simulation Appendix D: Figure D5) shown in Figure 6.10.

The orientation relationship between the matrix and the AlN precipitate A was found to be:

zone axes: $[\,013\,]_M$ // near (~2°) to $[\,12\bar{3}0\,]_P$

where M indicates matrix and P indicates precipitate.

atom planes: $(\,200\,)_M$ // $(0002)_P$ and $(\,0\bar{3}1\,)_M$ // $(\,2\bar{1}\bar{1}0\,)_P$; next nearest was $(\,1\bar{3}1\,)_M$ // near (~5°) $(\,2\bar{1}\bar{1}4\,)_P$

In Figure 6.10 another precipitate, labelled B can be seen. From the EDX spectrum shown in Figure 6.14, precipitate B was identified to be an aluminum oxide, Al_2O_3. However, the precipitate was very thin, with no Kikuchi lines arising from the diffraction of previously inelastically scattered electrons for defining the sense of tilt. Thus, further structural identification could not be pursued.

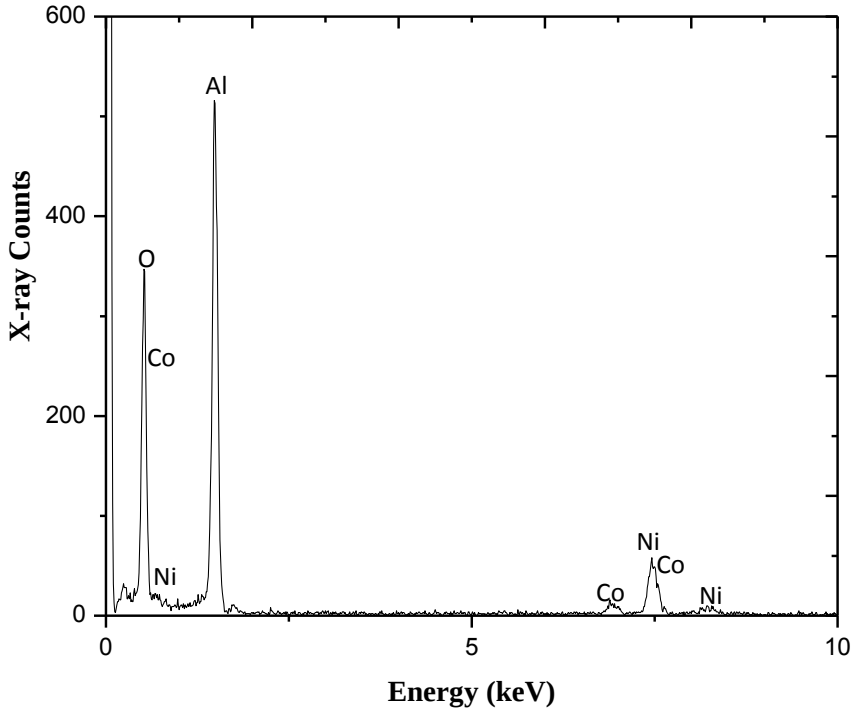


Figure 6.14: EDX spectrum of precipitate B in Figure 6.10.

In Figure 6.15 a plate-like precipitate labelled Z can be seen. The EDX spectrum from this precipitate, Figure 6.16, indicated it to be an aluminium nitride. Other elements such as Ni and Co present in the spectrum are presumably due to electron scattering onto the surrounding matrix. The diffraction patterns from a low index zone for the matrix next to the precipitate and from the precipitate itself are shown in Figures 6.17 (a) and (b) respectively. Tables 6.3 and 6.4 compare the measured and calculated planar separations and angles from the matrix and precipitate. From these and other different zone axis diffraction patterns for the precipitate it was found to have the hexagonal structure of AlN. The complete identification of the two diffraction patterns is given in Figure 6.18 and agree with the simulated diffraction patterns, shown in Appendix D.

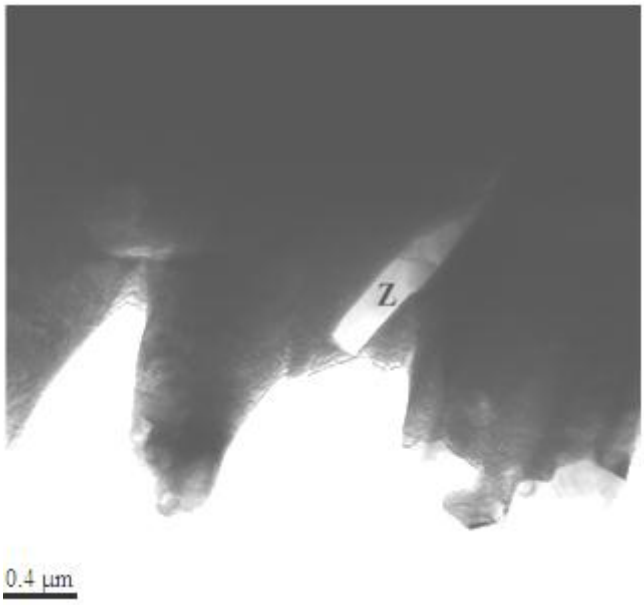


Figure 6.15: Cross-sectional bright field TEM image of a plate-shaped precipitate labelled Z in the internal oxidation zone of the TMS-75 superalloy after 100 h oxidation in air at 900^{o}C.

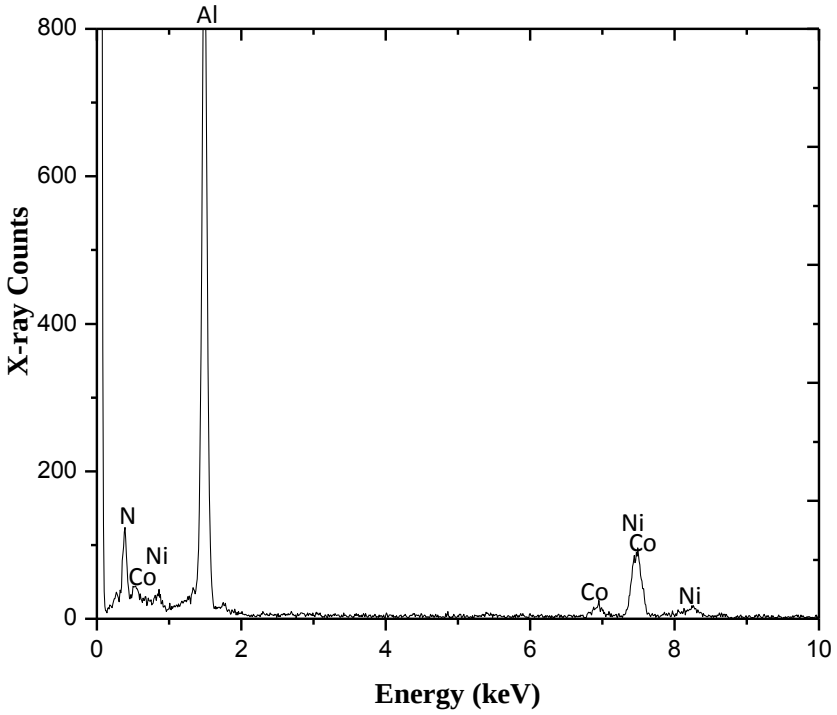
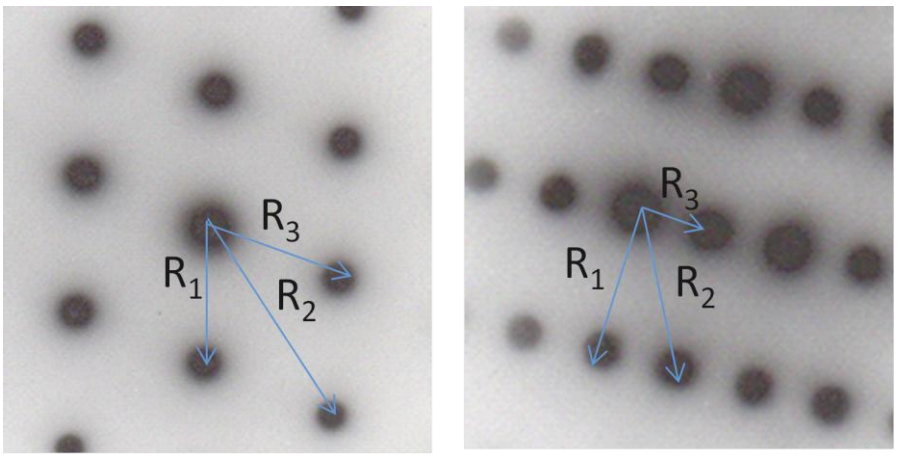


Figure 6.16: EDX spectrum of a plate-shaped precipitate Z in Figure 6.15.



a b

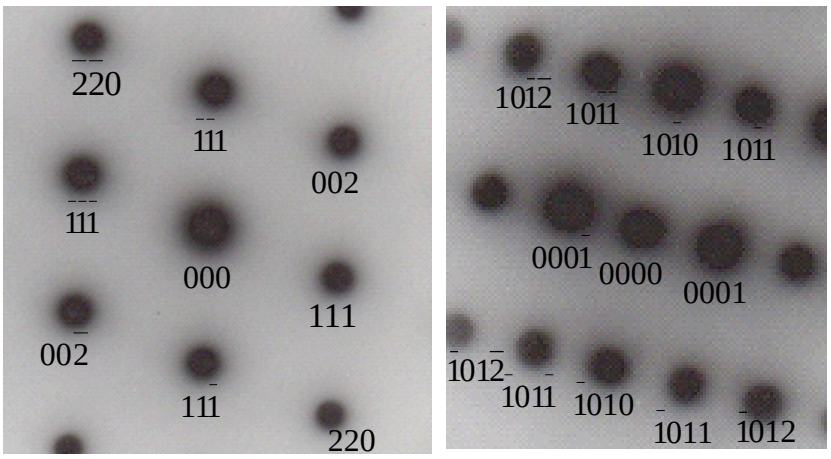
Figure 6.17: Electron diffraction patterns of (a) matrix and (b) precipitate Z in Figure 6.15.

Table 6.3: Values of spacing R, d_{hkl}, *hkl* and θ for the matrix in Figure 6.17(a).

	$r_{measured}$ (mm)	$r_{calculated}$ (mm)	d_{hkl} (Å)	*hkl*	$\theta_{measured}$	$\theta_{calculated}$
R_1	8.0	8.1	2.034	$1\bar{1}$	111^220 36°	111^220 35°
R_2	13.1	13.2	1.246	220		
R_3	8.1	8.1	2.034	111	220^1$\bar{1}$ 36°	220^1$\bar{1}$ 35°

Table 6.4: Values of spacing R, d_{hkl}, *hkl* and θ for precipitate Z in Figure 6.17(b).

	$r_{measured}$ (mm)	$r_{calculated}$ (mm)	d_{hkl} (Å)	*hkil*	$\theta_{measured}$	$\theta_{calculated}$
R_1	6.1	6.1	2.694	$10\bar{1}0$	$10\bar{1}0$^$10\bar{1}1$ 28°	$10\bar{1}0$^$10\bar{1}1$ 29°
R_2	7.0	7.0	2.370	$10\bar{1}1$		
R_3	3.3	3.3	4.978	0001	$10\bar{1}1$^0001 62°	$10\bar{1}1$^0001 62°



a **b**

Figure 6.18: Indexed diffraction pattern of (a) matrix [$1\bar{1}0$] (compare with simulation Appendix D: Figure D2) and (b) precipitate Z [$01\bar{1}0$] (compare with simulation Appendix D: Figure D6) in Figure 6.15.

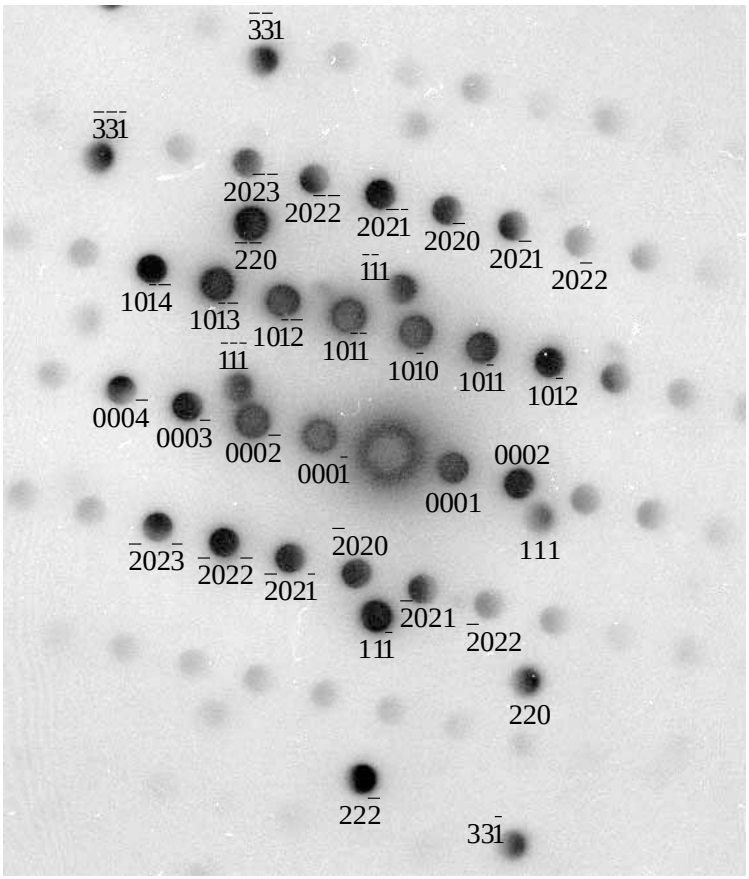


Figure 6.19: Combined diffraction pattern from the matrix and precipitate Z taken at the precipitate zone axis [$01\bar{1}0$].

The orientation relationship between the matrix and AlN precipitate Z was found to be:

zone axes: $[1\bar{1}0]_M$ // near (~3^o) to $[0\bar{1}\bar{1}0]_P$

atom planes: the closest alignment was $(220)_M$ // near (2^o) to $(\bar{1}012)_P$; the next nearest being $(111)_M$ // some 9^o from $(0002)_P$

The portion remaining of precipitate C in Figure 6.20 was identified to be Al_2O_3 from the corresponding EDX spectrum, Figure 6.21. The other elements in the EDX spectra resulted from electron scattering onto the neighbouring material and the carbon from hydrocarbon contamination on the sample surface. Precipitate C was unfortunately too thin to be practical for tilting work for orientation relationship information.

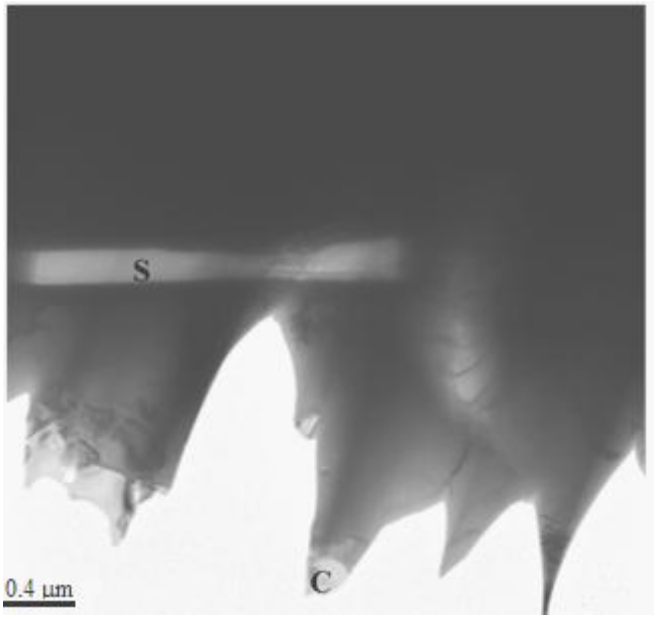


Figure 6.20: Cross-sectional bright field TEM image of precipitate C and a plate-shaped precipitate S in the internal oxidation zone of the TMS-75 superalloy after 100 h oxidation in air at 900°C.

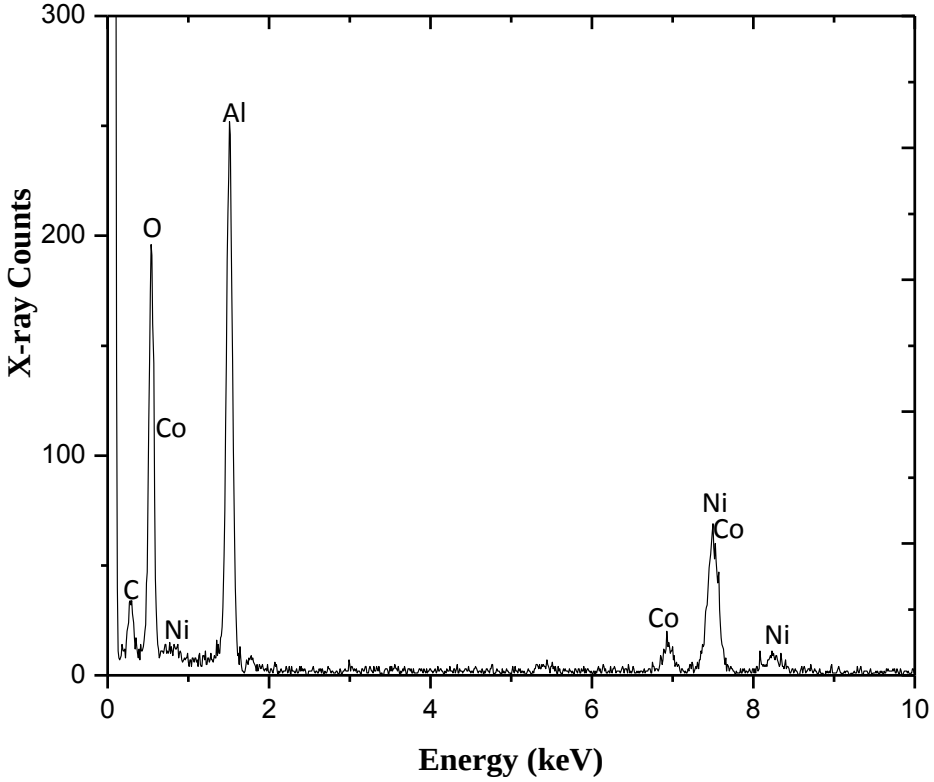


Figure 6.21: EDX spectrum from the remaining portion of precipitate C in Figure 6.20.

The plate-shaped precipitates S in Figure 6.20 and R in Figure 6.22 were identified from EDX measurements (Figure 6.23 for precipitate S) to be nitrides of aluminium. The diffraction patterns derived from both precipitates S and R were identical. One zone axis for precipitate R is shown here in Figure 6.24, and from Table 6.6 it was confirmed that the phase corresponded to hexagonal AlN as did that for precipitate S. The complete identification of the two diffraction patterns is given in Figure 6.25 and agree with the simulated diffraction patterns, shown in Appendix D.

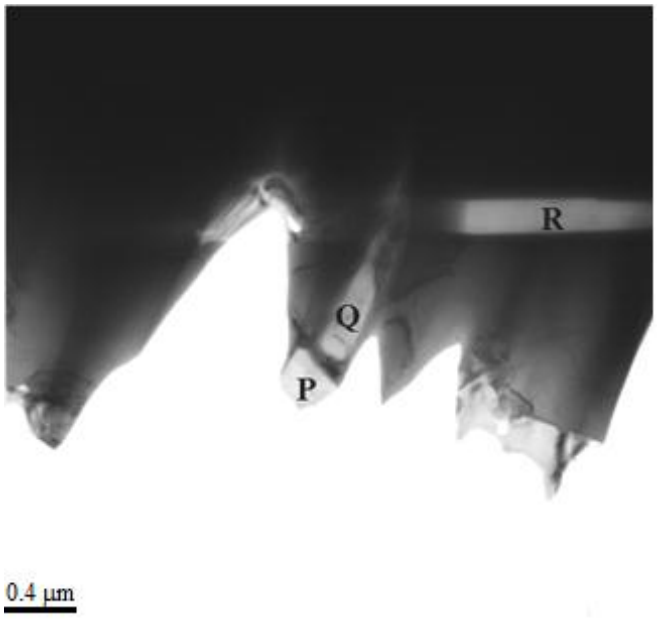


Figure 6.22: Cross-sectional bright field TEM image of a plate-shaped precipitate (Q), plate-shaped precipitate (R) and a precipitate (P) in the internal oxidation zone of the TMS-75 superalloy after 100 h oxidation in air at 900^{o}C.

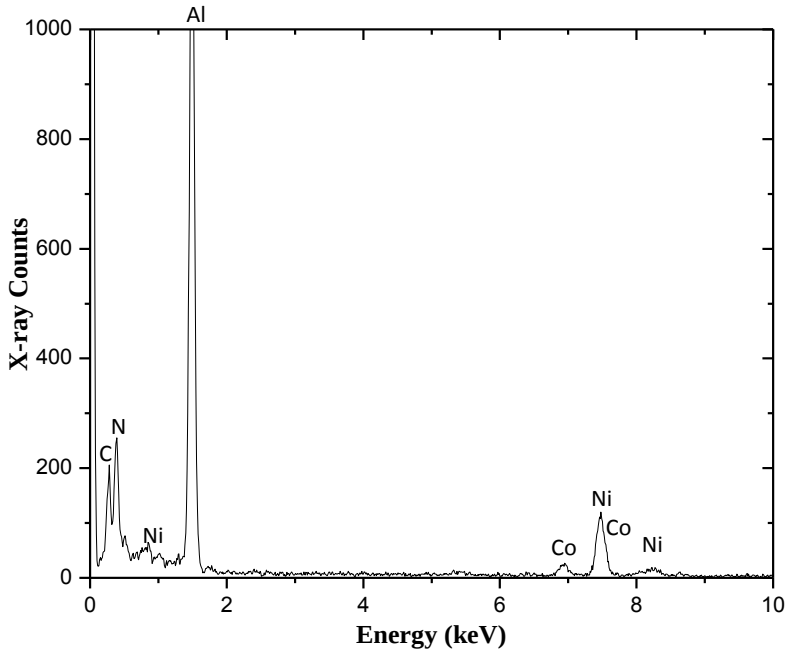
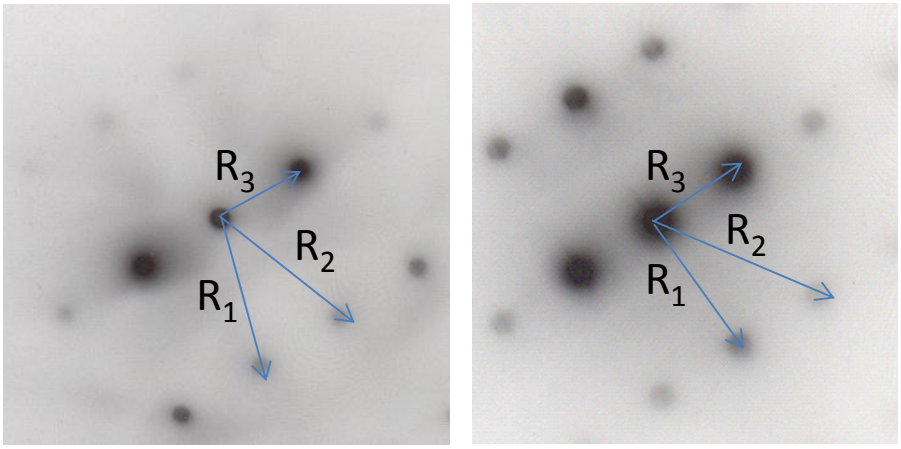


Figure 6.23: EDX spectrum obtained from a plate-shaped precipitate S in Figure 6.20. This is identical to the EDX spectrum obtained from plate-shaped precipitate R in Figure 6.22.



a **b**

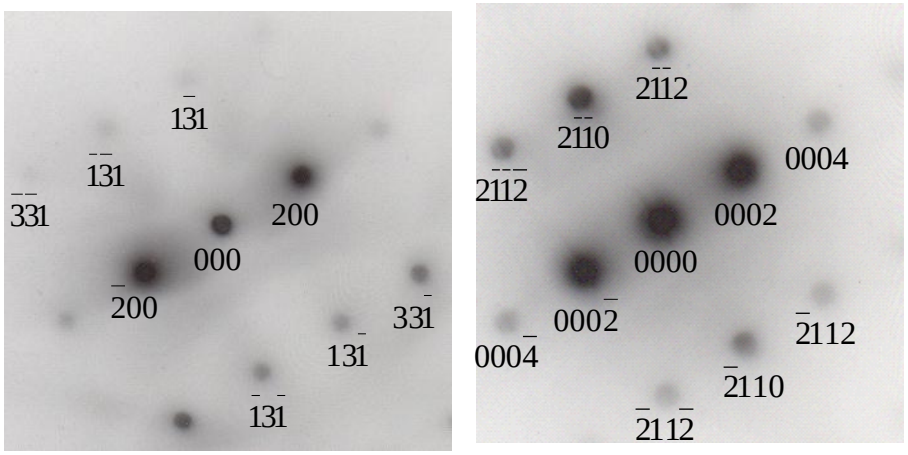
Figure 6.24: Electron diffraction patterns of (a) matrix (b) precipitate R in Figure 6.22.

Table 6.5: Values of spacing R, d_{hkl}, *hkl* and θ for the matrix in Figure 6.24(a).

	$r_{measured}$ (mm)	$r_{calculated}$ (mm)	d_{hkl} (Å)	*hkl*	$\theta_{measured}$	$\theta_{calculated}$
R_1	15.3	15.3	1.063	$\bar{1}3\bar{1}$	$\bar{1}3\bar{1}\,\hat{}\,13\bar{1}$ 35°	$\bar{1}3\bar{1}\,\hat{}\,13\bar{1}$ 35°
R_2	15.5	15.3	1.063	$13\bar{1}$		
R_3	9.3	9.2	1.751	200	$13\bar{1}\,\hat{}\,200$ 71°	$13\bar{1}\,\hat{}\,200$ 72°

Table 6.6: Values of spacing R, d_{hkl}, *hkl* and θ for precipitate R in Figure 6.24(b).

	$r_{measured}$ (mm)	$r_{calculated}$ (mm)	d_{hkl} (Å)	*hkil*	$\theta_{measured}$	$\theta_{calculated}$
R_1	6.1	6.0	2.690	$\bar{2}110$	$\bar{2}110\,\hat{}\,\bar{2}112$ 30°	$\bar{2}110\,\hat{}\,\bar{2}112$ 29°
R_2	6.5	6.5	2.489	$\bar{2}112$		
R_3	3.3	3.3	4.975	0002	$\bar{2}112\,\hat{}\,0002$ 60°	$\bar{2}112\,\hat{}\,0002$ 62°



a **b**

Figure 6.25: Indexed diffraction pattern of (a) matrix $[\,013\,]$ (compare with simulation Appendix D: Figure D1) and (b) precipitate R $[\,12\bar{3}0\,]$ (compare with simulation Appendix D: Figure D5) in Figure 6.24.

The orientation relationship between the matrix and the AlN precipitates S and R was found to be:

zone axes: $[\,013\,]_M$ // near (~1.5°) to $[\,12\bar{3}0\,]_P$

atom planes: $(\,200\,)_M$ // $(\,0002\,)_P$ and $(\,03\bar{1}\,)_M$ // near (~1.5°) to $(\,11\bar{2}0\,)_P$

The EDX spectrum, Figure 6.26, obtained from the remaining part precipitate P shown in Figure 6.22 indicated that the precipitate was Al_2O_3. The Ni and Co peaks originated from contributions from electron scattering onto the surrounding matrix material. Unfortunately, the precipitate was too thin to be practical for serious tilting zone axis diffraction studies, so no further investigation was undertaken.

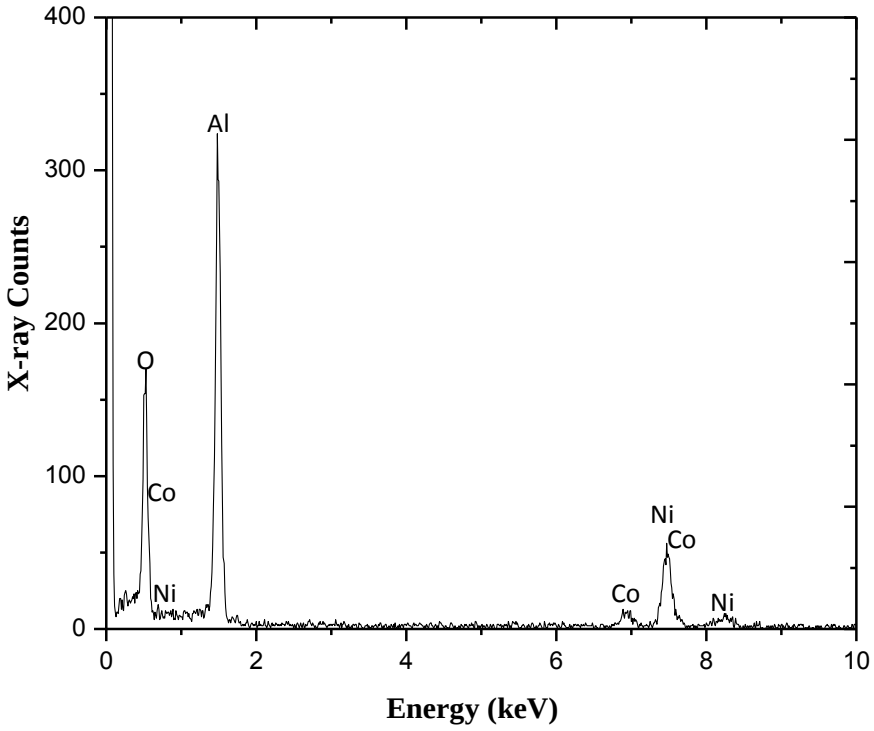


Figure 6.26: EDX spectrum from the remaining part of precipitate P in Figure 6.22.

In Figure 6.22, the precipitate Q was identified from the EDX spectrum shown in Figure 6.27 to be an aluminium nitride. The other elements originated from the surrounding matrix material while the carbon came from hydrocarbon contamination on the surface of the sample. Figures 6.28 (a) and (b) display the zone axis diffraction patterns from both the matrix next to the precipitate and the precipitate Q. Tables 6.7 and 6.8 give the measured and calculated planar spacings and angles between planes for the both the matrix and the precipitate. A good fit can be seen between measured and calculated values. From this zone axis and others not shown, as well as the simulated diffraction patterns in Appendix D, the precipitate structure was confirmed as hexagonal AlN. Figure 6.29 shows the indexed diffraction patterns of (a) the matrix and (b) precipitate Q.

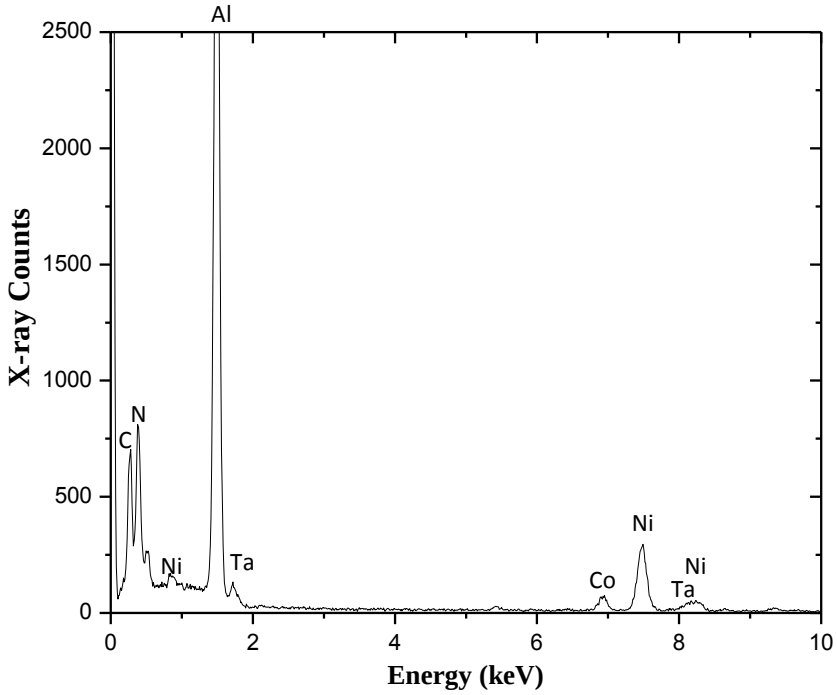
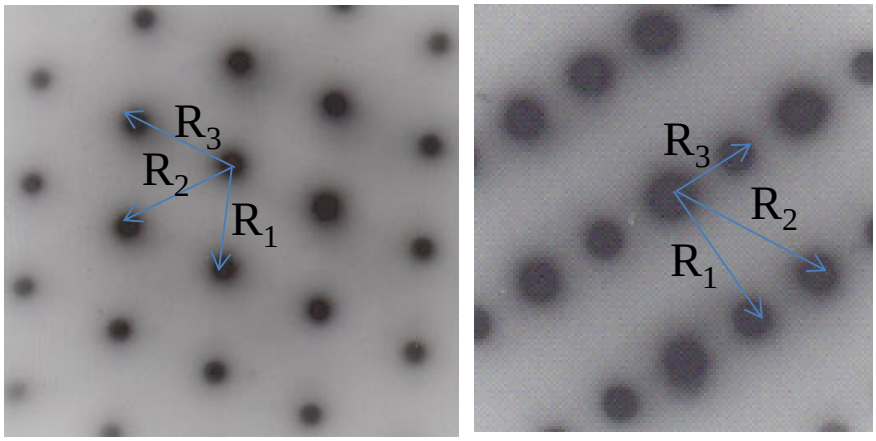


Figure 6.27: EDX spectrum of the precipitate Q shown in Figure 6.22.



a **b**

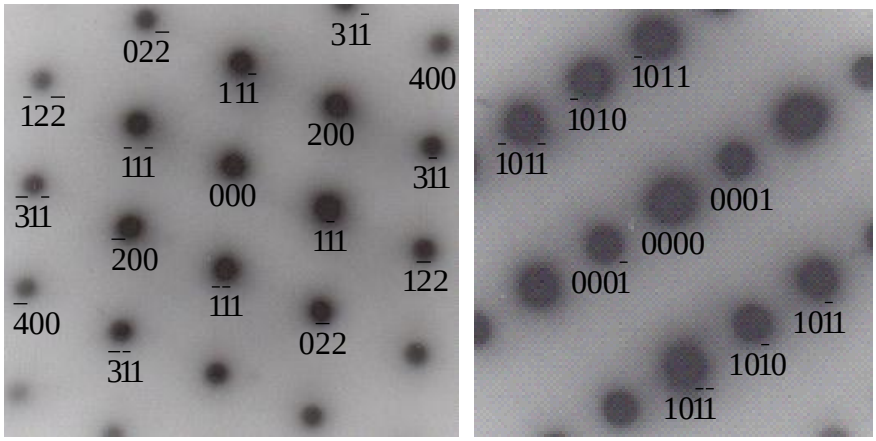
Figure 6.28: Electron diffraction patterns of (a) the matrix (b) precipitate Q in Figure 6.22.

Table 6.7: Values of spacing R, d_{hkl}, *hkl* and θ for the matrix in Figure 6.28(a).

	$r_{measured}$ (mm)	$r_{calculated}$ (mm)	d_{hkl} (Å)	*hkl*	$\theta_{measured}$	$\theta_{calculated}$
R_1	8.0	8.0	2.034	$\bar{1}1\bar{1}$	$\bar{1}1\bar{1}\,\hat{}\,1\bar{1}1$ 70°	$\bar{1}1\bar{1}\,\hat{}\,1\bar{1}1$ 70°
R_2	8.0	8.0	2.034	$1\bar{1}\bar{1}$		
R_3	9.3	9.3	1.762	200	$\bar{1}1\bar{1}\,\hat{}\,200$ 55°	$\bar{1}1\bar{1}\,\hat{}\,200$ 55°

Table 6.8: Values of spacing R, d_{hkl}, *hkl* and θ for the precipitate Q in Figure 6.28(b).

	$r_{measured}$ (mm)	$r_{calculated}$ (mm)	d_{hkl} (Å)	*hkil*	$\theta_{measured}$	$\theta_{calculated}$
R_1	6.1	6.1	2.690	$10\bar{1}0$	$10\bar{1}0$^0001 90°	$10\bar{1}0$^0001 90°
R_2	7.0	6.9	2.380	$10\bar{1}1$		
R_3	3.3	3.3	4.981	0001	$10\bar{1}1$^0001 60°	$10\bar{1}1$^0001 61°



a **b**

Figure 6.29: Indexed diffraction patterns of (a) the matrix [1$\bar{1}$0] (compare with simulation Appendix D: Figure D3) and (b) precipitate Q [01$\bar{1}$0] (compare with simulation Appendix D: Figure D6) in Figure 6.22.

Figure 6.30 shows the combined diffraction pattern from the precipitate and matrix. The precipitate is at its zone axis while that for the matrix is some 5^o away being positioned off the bottom right hand side of the image. The elongated diffraction spots result from the shape of the precipitate.

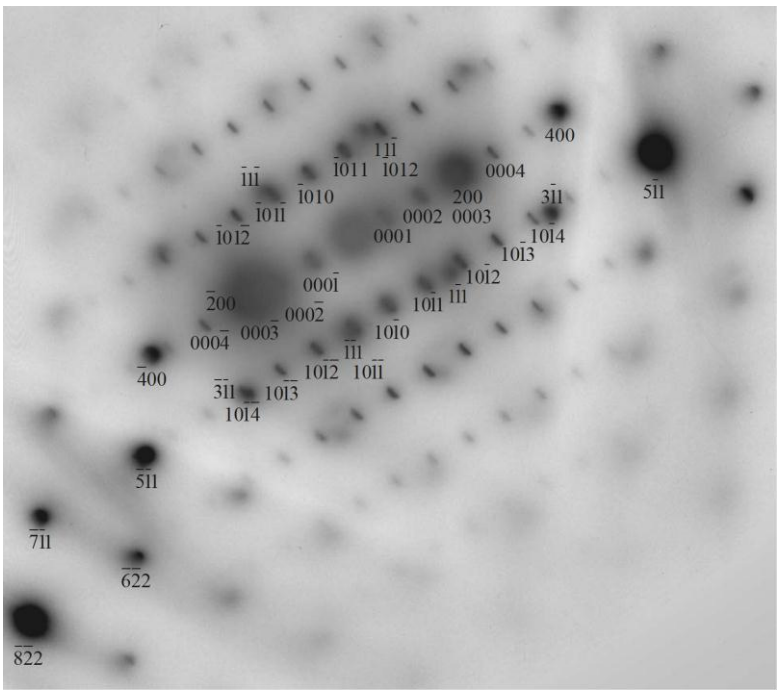


Figure 6.30: Combined diffraction pattern from the matrix and precipitate Q taken at the precipitate zone axis $[0\bar{1}\bar{1}0]$.

The orientation relationship between the matrix and the AlN precipitate Q was found to be:

zone axes: $[011]_M$ // near (~5°) to $[0\bar{1}\bar{1}0]_P$

atom planes: $(200)_M$ // $(0002)_P$ and $(3\bar{1}\bar{1})_M$ // very close (~0.5°) to $(\bar{1}010)_P$

Figure 6.31 is a bright field TEM image of an area of the internal reaction zone showing three precipitates labelled C, D and E. Figure 6.32 shows the EDX spectrum obtained from precipitate D revealing that it is an aluminium oxide. Figure 6.33 shows one set of zone axis diffraction patterns from the precipitate and the neighbouring matrix. Tables 6.9 and 6.10 compare the measured and calculated planar spacings and angles between planes for the final indexing of both the matrix and precipitate patterns. The indexing of this precipitate diffraction pattern was confirmed from the simulated diffraction patterns, Appendix D. Other zone axis patterns obtained from precipitate D revealed that this precipitate had the rhombohedral structure of α-Al_2O_3 (a = 5.136 Å, α = β = γ = 55.28°, space group $R\bar{3}c$, no.167) [98].

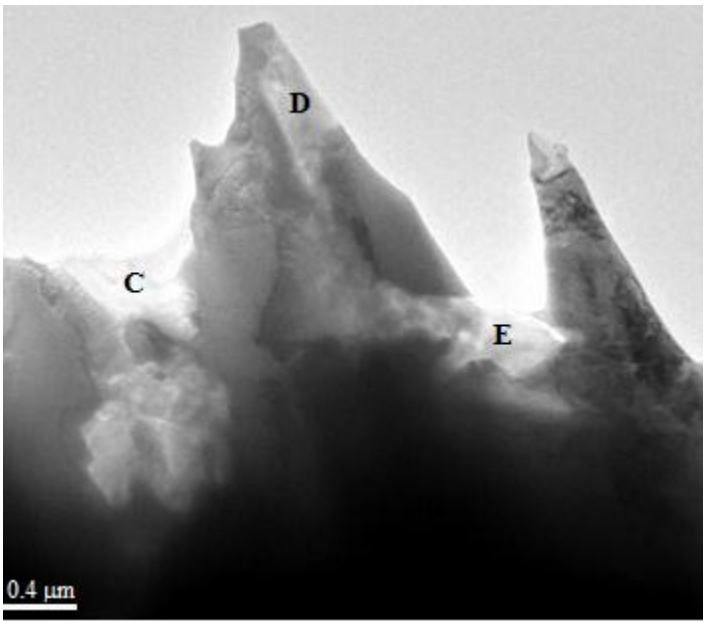


Figure 6.31: Cross-sectional bright field TEM image of precipitates C, D and E in the internal oxidation zone of the TMS-75 superalloy after 100 h oxidation in air at 900^{o}C.

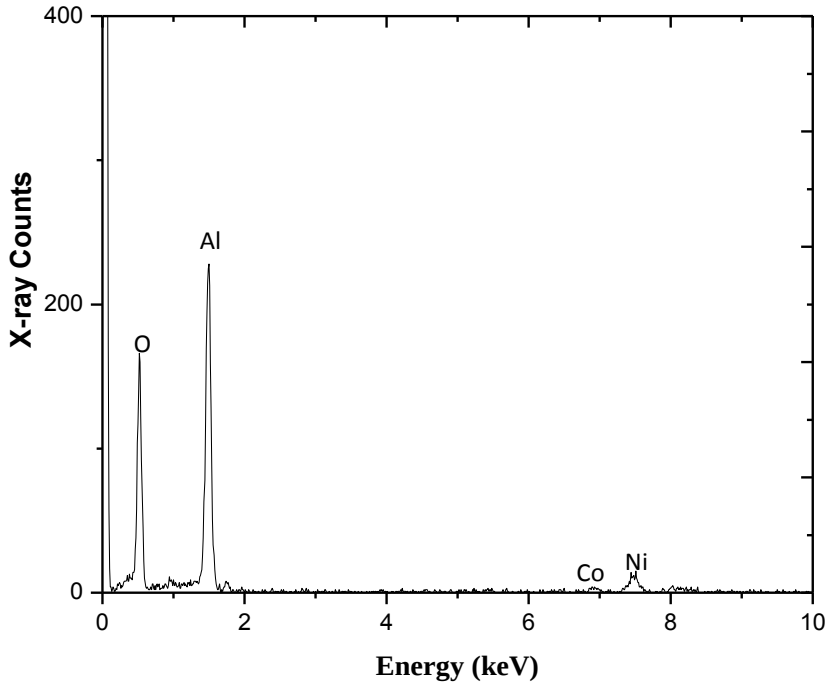
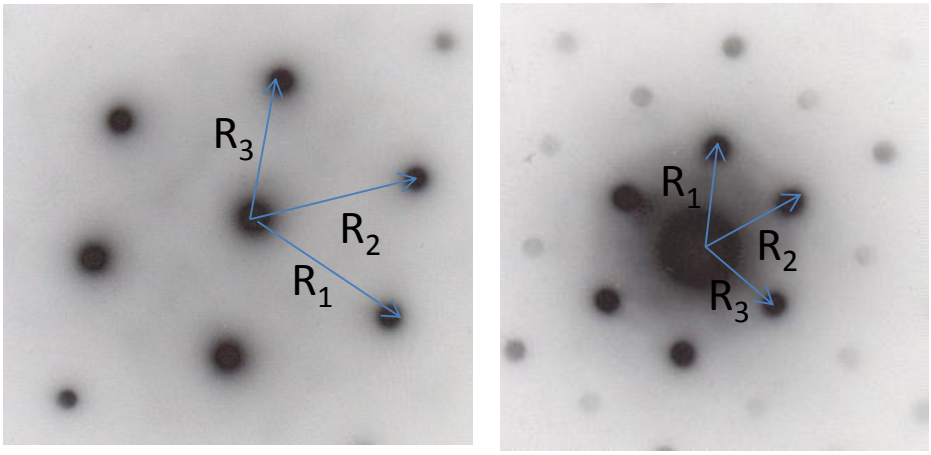


Figure 6.32: EDX spectrum of precipitate D in Figure 6.31. The spectrum for precipitate E was identical to the above.



a **b**

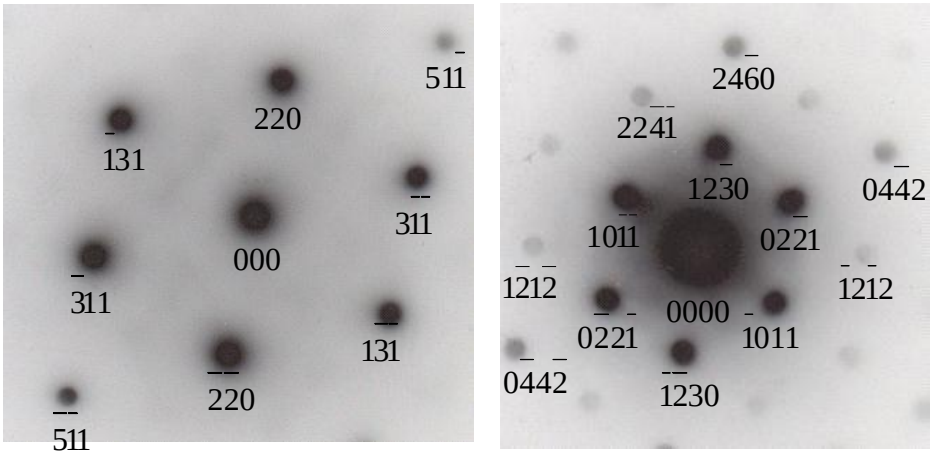
Figure 6.33: Electron diffraction patterns of (a) matrix (b) precipitate D in Figure 6.31.

Table 6.9: Values of spacing R, d_{hkl}, *hkl* and θ for the matrix in Figure 6.33(a).

	$r_{measured}$ (mm)	$r_{calculated}$ (mm)	d_{hkl} (Å)	*hkl*	$\theta_{measured}$	$\theta_{calculated}$
R_1	15.3	15.2	1.064	$1\bar{3}\bar{1}$	$1\bar{3}\bar{1}\,\hat{}\,3\bar{1}\bar{1}$ 50°	$1\bar{3}\bar{1}\,\hat{}\,3\bar{1}\bar{1}$ 50°
R_2	15.3	15.2	1.604	$3\bar{1}\bar{1}$		
R_3	13.0	12.9	1.297	220	$3\bar{1}\bar{1}\,\hat{}\,220$ 65°	$3\bar{1}\bar{1}\,\hat{}\,220$ 65°

Table 6.10: Values of spacing R, d_{hkl}, *hkl* and θ for the precipitate D in Figure 6.33(b).

	$r_{measured}$ (mm)	$r_{calculated}$ (mm)	d_{hkl} (Å)	*hkil*	$\theta_{measured}$	$\theta_{calculated}$
R_1	7.9	7.7	2.085	$12\bar{3}0$	$12\bar{3}0\,\hat{}\,0\bar{2}2\bar{1}$ 51°	$12\bar{3}0\,\hat{}\,0\bar{2}2\bar{1}$ 50°
R_2	7.9	7.7	2.085	$0\bar{2}2\bar{1}$		
R_3	6.9	6.8	2.379	$\bar{1}011$	$0\bar{2}2\bar{1}\,\hat{}\,\bar{1}011$ 65°	$0\bar{2}2\bar{1}\,\hat{}\,\bar{1}011$ 65°



a **b**

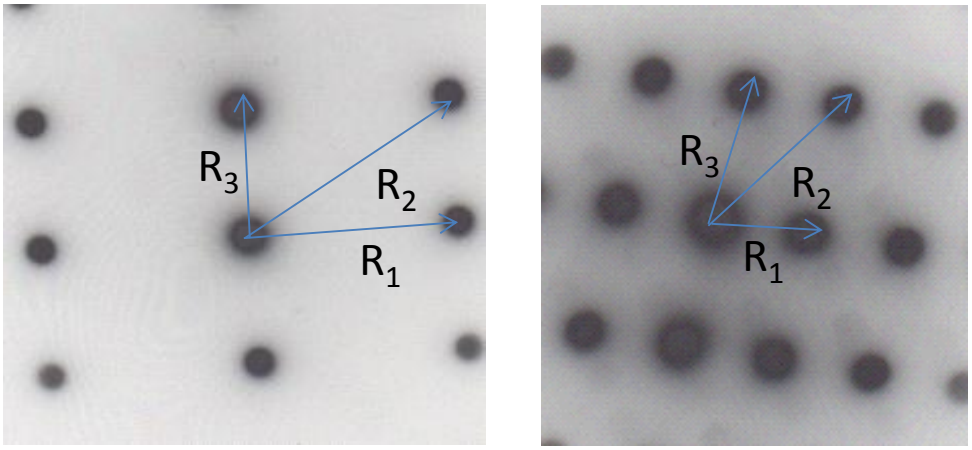
Figure 6.34: Indexed diffraction pattern of (a) the matrix [$\bar{1}1\bar{4}$] (compare with simulation Appendix D: Figure D4) and (b) precipitate D [$2\bar{1}\bar{1}2$] (compare with simulation Appendix D: Figure D7) in Figure 6.31.

The orientation between the matrix and the α-Al_2O_3 precipitate D was found to be:

zone axes: $[1\bar{1}4]_M$ // near ($\sim 4^o$) to $[2\bar{1}\bar{1}2]_P$

atom planes: $(13\bar{1})_M$ // close ($\sim 2^o$) to $(\bar{1}011)$; next nearest $(110)_M$ // near ($\sim 4^o$) to $(12\bar{3}0)_P$

In proximity to the precipitate D, but a little deeper into the sample, were precipitates C and E, Figure 6.31. The EDX spectrum from the two precipitates was similar to that of precipitate D in Figure 6.32, which indicated that the precipitates were also an aluminium oxide. The diffraction pattern obtained from the precipitate E, Figure 6.35, was of a different zone axis to precipitate D. The final indexing of the diffraction pattern of precipitate E, Table 6.12 and Figure 6.36, confirmed by the simulated diffraction pattern in Appendix D, indicated that precipitate C and E had the rhombohedral structure of α-Al_2O_3 of precipitate D. This identification was also confirmed from two other different zone axes patterns not shown here, and from simulated diffraction patterns of the α-Al_2O_3 structure.



a **b**

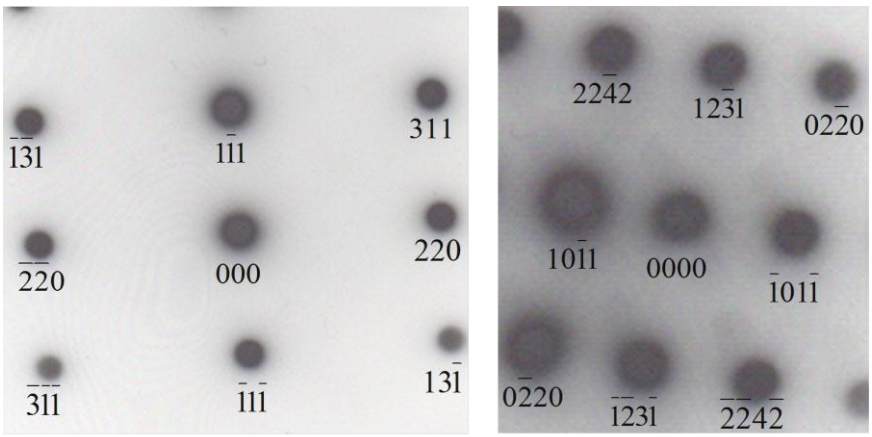
Figure 6.35: Electron diffraction patterns of (a) matrix (b) precipitate E in Figure 6.31.

Table 6.11: Values of spacing for (a) R, d_{hkl}, *hkl* and θ matrix in Figure 6.35(a).

	$r_{measured}$ (mm)	$r_{calculated}$ (mm)	d_{hkl} (Å)	*hkl*	$\theta_{measured}$	$\theta_{calculated}$
R_1	13.0	13.0	1.247	220	220^311 32°	220^311 32°
R_2	15.0	15.1	1.063	311		
R_3	8.0	7.9	2.037	$1\bar{1}1$	220^$1\bar{1}1$ 90°	220^$1\bar{1}1$ 90°

Table 6.12: Values of spacing R, d_{hkl}, *hkl* and θ for the precipitate E in Figure 6.35(b).

	$r_{measured}$ (mm)	$r_{calculated}$ (mm)	d_{hkl} (Å)	*hkil*	$\theta_{measured}$	$\theta_{calculated}$
R_1	4.7	4.6	3.479	$\bar{1}01\bar{1}$	$\bar{1}01\bar{1}$^$02\bar{2}0$ 50°	$\bar{1}01\bar{1}$^$02\bar{2}0$ 50°
R_2	8.3	8.2	1.964	$02\bar{2}0$		
R_3	6.4	6.3	2.551	$12\bar{3}1$	$02\bar{2}0$^$12\bar{3}1$ 34°	$02\bar{2}0$^$12\bar{3}1$ 34°



a **b**

Figure 6.36: Indexed diffraction pattern of (a) the matrix $[1\bar{1}\bar{2}]$ (compare with simulation Appendix D: Figure D5) and (b) precipitate E $[10\bar{1}\bar{1}]$ (compare with simulation Appendix D: Figure D8) in Figure 6.31.

The orientation relationship between the matrix and the α-Al_2O_3 precipitate E was found to be:

zone axes: $[1\bar{1}\bar{2}]_M$ // near ($\sim 5^o$) to $[10\bar{1}\bar{1}]_P$

atom planes: $(1\bar{5}3)_M$ // $(22\bar{4}2)_P$; next nearest being $(220)_M$ // near ($\sim 3^o$) to $(\bar{1}01\bar{1})_P$

Deeper into the material, about 45 µm from the surface of the external scale, the internal oxidation zone ended and the normal alloy two phase γ-γ' microstructure resumed as shown in Figure 6.37. The interfaces between the cuboidal γ'-precipitates and γ-matrix were straight indicating a small lattice mismatch between the two phases. As expected, the EDX spectrum from this region, Figure 6.38, showed the presence of elements Ni, Cr, Al, W, Ta, Mo and Co which represented, within the EDX detection limits, the elements constituting the alloy, Table 5.1. The carbon peak resulted from carbon contamination on the surface that had built up during the viewing and subsequent analysis.

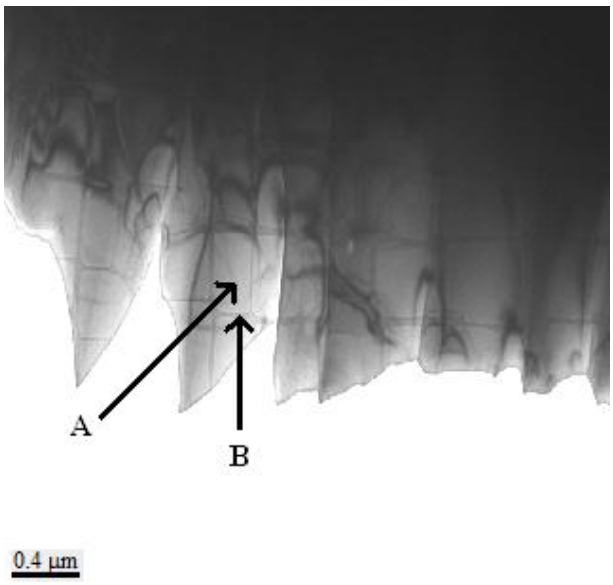


Figure 6.37: Bright field TEM micrograph showing the two phases: the γ′ phase labelled A, and the γ phase labelled B in the TMS-75 superalloy matrix after 100 h oxidation in air at 900^{o}C.

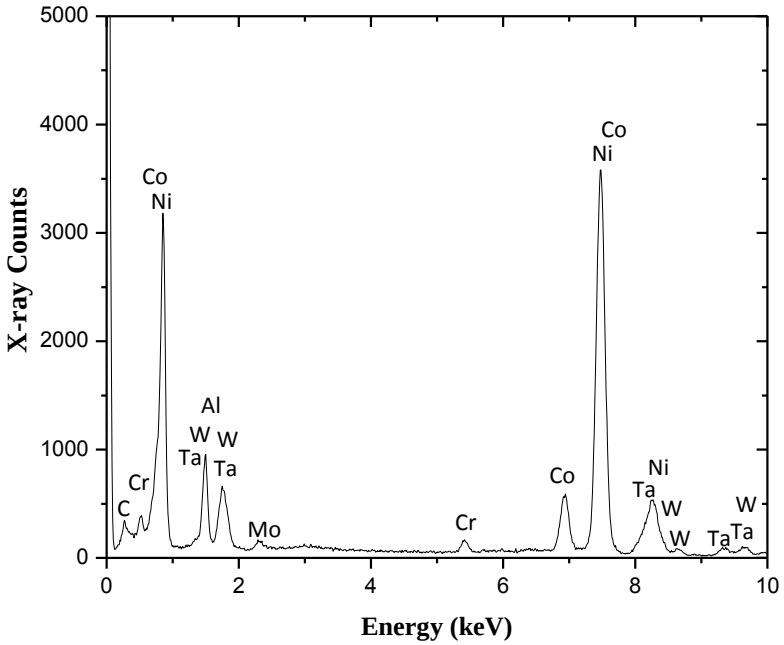


Figure 6.38: EDX spectrum from the γ-γ′ region in Figure 6.37.

6.3 Overview of the XRD and TEM results

The oxidized TMS-75 alloy exhibited an external oxide scale, about 20 μm thick, that generally completely covered the (001) face of the single crystal material, Figure 6.39. The scale consisted entirely of a mixed oxide (Ni,Co)O. The presence of Co has been found in the outer oxidation scale of the same surface orientation CMSX-10 [15], an alloy having only 25% of the concentration of Co of the present material. For both the TMS-75 and the CMSX-10 alloys heated for the same time and temperature in air, there was no evidence of any formation of Al_2O_3 or the spinel $Ni(Cr,Al)_2O_4$ within this scale, although both phases had been found in the oxidation product of earlier generations of superalloys [14].

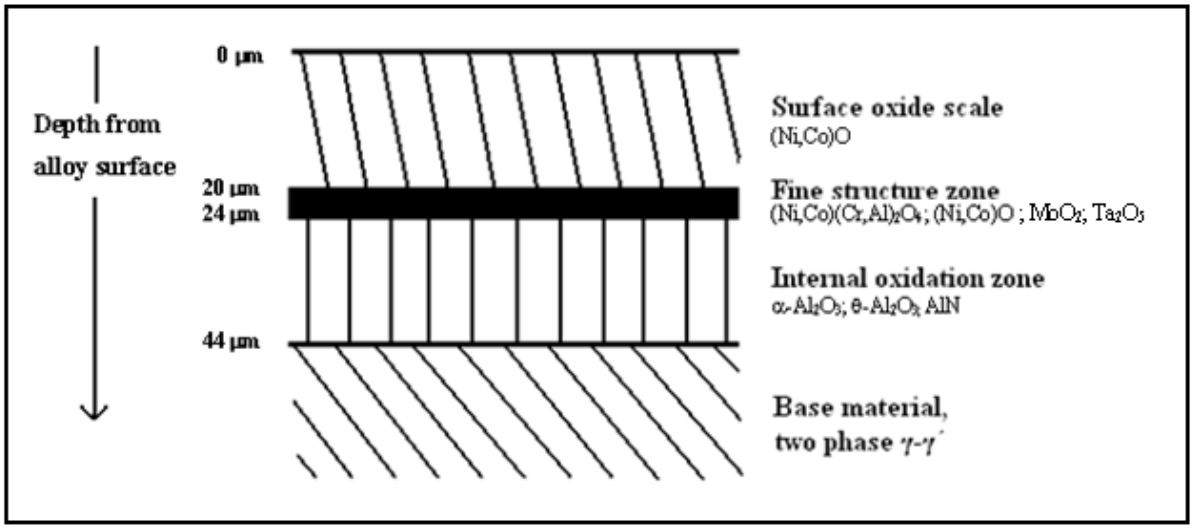


Figure 6.39: Schematic diagram of the oxidation zones.

The outer scale was found to be non-protective in that it allowed oxygen and nitrogen from the air to diffuse through it to the material below. Underneath the outer scale was a fine structure zone, around 4 μm thick, followed by an extensive internal reaction zone of thickness of around 20 μm. The reactive gas species diffusion resulted in the solubility limit being exceeded in the underlying zones, causing the formation of small grained oxides in the fine structure zone and in the formation of discrete precipitates within the internal reaction zone. In the latter zone, the alloy had lost its original γ-γ´ microstructure due to the oxidation depleting elements from the original matrix during the oxidation reaction. The precipitates formed within the internal reaction zone were analysed to be rhombohedral α-Al_2O_3 and hexagonal AlN. The finding of internally-formed nitrides in the present alloy is in agreement with previous work based on third and fourth generation nickel-based superalloys [15, 64, 99, 100] and Ni-Cr-Al model alloys [63, 101]. Chang [102] has shown that the nitrogen solubility

in Ni-based superalloys depends strongly on the Cr concentration. At lower Cr concentrations, the solubility rapidly decreases resulting in nitride precipitation. Typically, the nitride precipitates found in the present study were located below the oxide phases. Dong *et al*. [103] have reported that while the zone of internal nitridation is much deeper than that for oxidation, the diffusion coefficients for oxygen and nitrogen appear to have values of the same magnitude at 1000^{o}C [104, 105]. No oxynitrides were identified, in contrast to the SEM study by Pruessner and Harada [101]. While it is possible that small amounts oxygen may have been in the present nitrides, there was not enough to affect the nitride structure as determined by TEM diffraction and XRD. The precipitation of both the oxides and the nitrides, as well as the loss of the strengthening γ-γ′ microstructure would be expected to result in the internal oxidation zone being a mechanically weakened region.

The fine structure zone was composed mainly of mixed spinel oxides. The concentrations of Al and all the refractory elements (Cr, Ta, W, Mo and Re) were higher than their corresponding values in the base material. The concentration of the refractory elements was in fact highest in this region. The decrease in nickel content was most dramatic in spite of the fact that this element was present in significant amounts on either side of this zone. Such a fine grained, multi-spinel structured zone and with similar elemental compositions has been reported previously by Akhtar *et al*. [15] in oxidized CMSX-10. The elemental content of this zone was found to increase with respect to nickel, chromium and oxygen with depth. While the origin of this local compositional variation is unclear, it would indicate that small local variations in composition can have a marked effect on the oxidation process.

The apparent identification by XRD of the Ta_2O_5 phase in the fine structure zone was somewhat unexpected. From comparison with other similar alloys, one might have rather anticipated a (Ni,Co,Ta) oxide phase due to the solubility of Ni and Co in tantalum oxide as had been reported previously by Akhtar *et al*. [15]. These authors identified (Ni,Co)Ta_2O_6 in their alloy after a similar heat treatment to the current work. No data were found for either or both Ni or Co with (Ta_2O_5) from the scientific literature, the Bruker Diffrac plus Eva peak matching software, and the Inorganic Crystal Structure Database (ICSD) site [97]. Combinations with W and Cr also failed to fit the current XRD data. As such, the Ta_2O_5 identification was maintained in Figure 6.2. However, Kawagishi *et al*. [106] reported that not only can the tantalum oxide be stable within such an oxide layer, but it also acts to stabilize the oxide of rhenium which has a high vapour pressure at high temperatures.

The difference in oxidation behaviours between the first and second, and the later generation NBSAs results from the fact that both the third and fourth generation alloys were developed mainly with mechanical properties, such as creep at high temperatures, a priority. Third generation alloys thus have a high rhenium content compared to second generation alloys, ~1.7 at.% Re as against 1 at.% Re [64]. This higher Re content then requires a lower Cr/Co ratio to stabilize the microstructure and prevent the detrimental formation of topologically close-packed (TCP) phases, which would cause a decrease in the alloys' high temperature strength since they degrade the structural integrity of the material [107] and deplete the matrix of solid-solution strengtheners [108]. As a result of this balancing act, however, these alloys can become borderline in terms of their resistance to oxidation, since chromium is a requirement to ensure the formation of a protective alumina scale. A problem is that at lower temperatures, as found in the present investigation, the required protective outer scale is not formed, resulting in the reactive gas phase species diffusing into the alloy and producing an internal oxidation zone. For nickel-based superalloys, the solubility of nitrogen depends on the chromium concentration [102]. As the chromium concentration is reduced to lower values, the nitrogen solubility rapidly decreases resulting in nitride precipitation, as was confirmed in this study. It would appear then that a possible solution to this problem could be to increase the chromium concentration to a point before the deleterious formation of any TCP phases and also where a viable external, compact, adhering protective layer is in place. Thus, an increase in both chromium content and reactive elements should be able, in principle, to improve the overall oxidation performance for such third and fourth generation TMS alloys [100].

Typically spallation of the external scale was not observed. The only time some brittleness and spallation was noted during TEM preparation when it was occasionally necessary to reglue detached sample surfaces. While not an important effect at this temperature, unlike at higher temperatures for this alloy [100], such spallation could be prevented and hence better overall oxidation performance achieved by increasing the concentration of effective reactive elements in the alloy, adding other reactive elements to the alloy [41, 109, 110], lowering the rhenium content or increasing the tantalum content [106].

Unlike studies on surface oxidation films on some other nickel-based superalloys, for example CMSX-10 [15], no epitaxial relationship was found between the various phases and the surrounding matrix material within the internal reaction zone. This is in spite of a number of low index zone axes being investigated. Typically, the zone axis of a given precipitate and that of the surrounding matrix were within 1.5 - 5^{o} of each other. However, in spite of this

disparity, normally one to two planes of alignment or close alignment were indicated between the precipitate and matrix lattices. One might expect some alignment from the very obvious faceting of some of the precipitates, although at the magnifications available, there was no obvious kinking at the interfaces or interface dislocations.

All the aluminium nitrides were analysed to be of the stable wurtzite hexagonal phase, AlN. The orientation relationships found between the Ni - based solid solution matrix and the AlN were (exact if not stated):

$[013]_M$ // $[12\bar{3}0]_P$

$(200)_M$ // $(0002)_P$

$(0\bar{3}1)_M$ // $(2\bar{1}\bar{1}0)_P$

$[1\bar{1}0]_M$ // $[01\bar{1}0]_P$

$(220)_M$ // $(\bar{1}012)_P$ within 2^o

$[011]_M$ // $[01\bar{1}0]_P$

$(200)_M$ // $(0002)_P$

$(3\bar{1}1)_M$ // $(\bar{1}010)_P$

All the aluminium oxides were analysed to be of the stable rhombohedral phase, α-Al_2O_3. The orientation relationships found between the Ni - based solid solution matrix and the α-A l_2O_3 were (exact if not stated):

$[1\bar{1}4]_M$ // $[2\bar{1}\bar{1}2]_P$

$(1\bar{3}\bar{1})_M$ // $(\bar{1}011)_P$ within 2^o

$[1\bar{1}\bar{2}]_M$ // $[10\bar{1}\bar{1}]_P$

$(15\bar{3})_M$ // $(11\bar{2}1)_P$

This is the first reported orientation relationship between various precipitates and matrix in the internal reaction zone of a nickel-based superalloy. This is due to the fact that in the past

focus has been directed primarily towards the external oxide scale or coating, and to whether it was protective of the underlying material.

CHAPTER 7

Conclusions

An external 20 μm thick (Ni,Co)O scale was found to form on the polished surface of the third-generation TMS-75 alloy when heated at 900^{o}C for 100 hours in air. Beneath this layer was a composite thinner layer, around 4 μm thick, composed of the oxides (Ni,Co)O, $(Ni,Co)(Cr,Al)_2O_4$, MoO_2 and Ta_2O_5. Under this layer was a roughly 20 μm thick internal oxidation or reaction zone containing discrete precipitates of α-Al_2O_3 and AlN.

The spinel oxide, $(Ni,Co)(Cr,Al)_2O_4$, commonly observed in the internal oxidation zone of the first- and second-generation Ni-based superalloys was formed only in the fine structure zone immediately below the external oxidation scale of TMS-75. This is in contrast to the CMSX-10 alloy where it was not detected.

No epitaxial relationship was found between the matrix of the internal oxidation zone and any of the oxide or nitride precipitates within it, which is in contrast to typical external oxide scales and the underlying material. The zone axes of the matrix and precipitates typically were misoriented by 1.5 - 7^{o}. However, at specific orientations, certain planes of the matrix were identified to be parallel to precipitate planes. Such corresponding orientation relationships and accommodation were implied by the faceting of the precipitates, most of which exhibited a platelet-like shape, and the lack of interfacial dislocations. This is the first study of the orientation relationships between precipitates and the matrix in the internal oxidation zone of a nickel-based superalloy.

The low chromium content results in the extensive internal oxidation and nitridation at 900^{o}C.

The low concentration of reactive elements is not totally sufficient to prevent spallation at this temperature.

Possible future investigations

1) Study the order in which the various oxidation reactions occurred and how the oxidation products developed as a function of oxidation time. This could be undertaken using a Focused Ion Beam SEM to machine down into the sample from the surface as well as in cross section, yielding 3-dimensional volume images of the interior structure of the alloy. Software would then provide tools to fully analyse the volumes images collected, for example, image the volume from any direction, determine precipitate and oxide grain dimensions, morphologies and distributions etc. In parallel to the image collection, X-ray elemental maps could be collected providing the ability to study composition gradients as well as precipitate identification. For any region that was found to be particularly interesting, the microscope could machine out a thin slice for viewing in a TEM.

2) Simulate the atomic interface structure of the various precipitates with the matrix to investigate the accommodation and correspondence between the two structures for the orientation relationships determined in the present work and any further determined from suggested study 1) above. Investigate other likely faceting and habit planes.

3) Make new alloys having increased Cr and reactive element content [111] since clearly the alloy composition is not optimal at 900^{o}C, while recent published work [100] has shown that it is also not satisfactory at higher temperatures.

References

1. C.T. Sims, N.S. Stoloff and W.C. Hagel, *Superalloys II: High Temperature Materials for Aerospace and Industrial Power*, Wiley Inter-Science, New York (1987) p. 615.
2. W. E. Lee and K.P.D. Lagerlof, Structural and Electron Diffraction Data for Sapphire (α-Al_2O_3), *Journal of Electron Microscopy Technique* 2 (1985) 247-258.
3. C.S. Giggins and F.S. Petit, Oxidation of Ni-Cr-Al Alloys between 1000^{o}C and 1200^{o}C, *Journal of the Electrochemical Society* 118 (1971) 1782-1790.
4. H.E. Evans and M.P. Taylor, Proceedings of the Institution of Mechanical Engineers, Part G, *Journal of Aerospace Engineering* 220 (2006) 1-10.
5. T. Yokokawa, M. Osawa, K. Nishida, T. Kobayashi, Y. Koizumi and H. Harada, Partitioning Behaviour of Platinum Group Metals on the γ and γ' Phases of Ni-Base Superalloys at High Temperatures, *Scripta Materialia* 49 (2003) 1041-1046.
6. T. Wang, L.Q. Chen and Z.K. Liu, Lattice Parameters and Local Lattice Distortions in FCC-Ni Solutions, *Metallurgical and Materials Transactions* 38A (2007) 562-569.
7. R.L. Fleischer, Substitutional Solution Hardening, *Acta Metallurgica* 11 (1963) 203-210.
8. T. Wang, J.Z. Zhu, R.A. Mackay, L.Q. Chen and Z.K. Liu, Modeling of the Lattice Parameter in the Ni-Al System, *Metallurgical and Material Transactions* 35A (2004) 2313-2321.
9. D.J. Young, *High Temperature Oxidation and Corrosion of Metals*, Elsevier, Amsterdam (2009) p. 532.
10. N. Birks and G.H. Meier, *Introduction to High-Temperature Oxidation of Metals*, Cambridge University Press, UK (2006) p. 338.
11. G.R. Wallwork, The Oxidation of Alloys, *Reports on Progress in Physics* 39 (1976) 401-485.
12. D.R. Gaskell, *Introduction to Metallurgical Thermodynamics*, McGraw Hill, Washington D.C., USA (1981) p. 611.
13. C.M. Younes, G.C. Allen and J.A. Nicholson, High Temperature Oxidation Behaviour of Single Crystal Superalloys RR3OOO AND CMSX-4, *Corrosion Engineering, Science and Technology* (2007) 80-88.

14. M.H. Li, X.F. Sun, J.G. Li, Z.Y. Zhang, T. Jin and H.R. Guan, Oxidation Behavior of a Single-Crystal Ni-Base Superalloy in Air. I: At 800 and 900^{o}C, *Oxidation of Metals* 59 (2003) 591-605.
15. A. Akhtar, M.S. Hook and R.C. Reed, On the Oxidation of the Third-Generation Single-Crystal Superalloy CMSX-10, *Metallurgical and Materials Transactions* 36A (2005) 3001-3017.
16. F.H. Stott, G.C. Wood, D.P. Whittle, B.D. Bastow, Y. Shida and A. Martinez-Villafane, The Transport of Oxygen to the Advancing Internal Oxide Front during Internal Oxidation of Nickel-Base Alloys at High Temperature, *Solid State Ionics 12* (1984) 365-374.
17. A. Martinez-Villafane, F.H. Stott, J.G. Chacon-Nava and G.C. Wood, Enhanced Oxygen Diffusion along Internal-Oxide Metal Matrix Interfaces in Ni-Al Alloys during Internal Oxidation, *Oxidation of Metals* 57 (2002) 267-279.
18. P. Kofstad, *High Temperature Corrosion*, Elsevier, London (1988) p. 558.
19. F. Gesmundo and B. Gleeson, Oxidation of Multicomponent Two-Phase Alloys, *Oxidation of Metals* 44 (1995) 211-237.
20. F. Gesmundo, F. Viani, Y. Niu and D.L. Douglass, Further Aspects of the Oxidation of Binary Two-Phase Alloys, *Oxidation of Metals* 39 (1993) 197-209.
21. F. Gesmundo, F. Viani, Y. Niu and D.L. Douglass, The Transition from the Formation of Mixed Scales to the Selective Oxidation of the Most-Reactive Component in the Corrosion of Single and Two-Phase Binary Alloys, *Oxidation of Metals* 40 (1993) 373-393.
22. E. Schumman, G. Schontz, K.P. Trumble and M. Ruhle, Microstructural Observations on the Oxidation of γ'-Ni_3Al at Low Oxygen Partial Pressure, *Acta Metallurgica et Materialia* 40 (1992) 1311-1319.
23. I. Levin, L.A. Bendersky, D.G. Brandon and M. Ruhle, Cubic to Monoclinic Phase Transformations in Alumina, *Acta Materialia* 45 (1997) 3659-3669.
24. Y. Niu and F. Gesmundo, The Internal Oxidation of Ternary Alloys. VI: The Transition from Internal to External Oxidation of the Most-Reactive Component under Intermediate Oxidant Pressures, *Oxidation of Metals* 62 (2004) 391-410.
25. F. Gesmundo and Y. Niu, The Internal Oxidation of Ternary Alloys I: The Single Oxidation of the Most-Reactive Component under Low Oxidant Pressures, *Oxidation of Metals* 60 (2003) 347-370.
26. F.H. Stott, The Protective Action of Oxide Scales in Gaseous Environments at High Temperature, *Reports on Progress in Physics* 50 (1987) 861-913.

27. F.H. Stott, G.C. Wood and J. Stringer, The Influence of Alloying Elements on the Development and Maintenance of Protective Scales, *Oxidation of Metals* 44 (1995) 113-145.
28. G.C. Wood, High Temperature Oxidation of Alloys, *Oxidation of Metals* 2 (1970) 11-57.
29. F.H. Stott, G.C. Wood and M.G. Hobby, Comparison of the Oxidation Behaviour of Iron-Chromium-Aluminum, Nickel-Chromium-Aluminum, and Cobalt-Chromium-Aluminum Alloys, *Oxidation of Metals* 3 (1971) 103-113.
30. M.W. Brumm and H.J. Grabke, The Oxidation Behaviour of NiAl I. Phase Transformations in the Alumina Scale during Oxidation of NiAl and NiAl-Cr Alloys, *Corrosion Science* 33 (1992) 1677-1690.
31. H.P. Rooksby and J.M. Rooymans, The Formation and Structure of Delta Alumina, *The Mineralogical Society* (1961) 234-238.
32. B.C. Lippens and J.H. De Boer, Study of Phase Transformations during Calcination of Aluminum Hydroxides by Selected Area Electron Diffraction, *Acta Crystallographica* 17 (1964) 1312-1321.
33. M.H. Li, X.F. Sun, T. Jin, H.R. Guan and Z.Q. Hu, Oxidation Behavior of a Single-Crystal Ni-Base Superalloy in Air-II: At 1000, 1100, and 1150^{o}C, *Oxidation of Metals* 60 (2003) 195-210.
34. M.H. Li, X.F. Sun, T. Jin, H.R. Guan and Z.Q. Hu, Oxidation Kinetics and Scale Morphology of a Palladium-Modified-Aluminide Coating at High Temperature in Air, *Oxidation of Metals* 61 (2004) 91-104.
35. V. Jayaram and C.G. Levi, The Structure of δ-Alumina evolved from the Melt and the γ-δ Transformation, *Acta Metallurgica* 37 (1989) 569-578.
36. R. Prescott and M.J. Graham, The Formation of Aluminum Oxide Scales on High Temperature Alloys, *Oxidation of Metals* 38 (1992) 233-254.
37. D.P. Whittle and J. Stringer, Improvements in High Temperature Oxidation Resistance by Additions of Reactive Elements or Oxide Dispersions, *Philosophical Transactions Royal Society of London* 295 (1980) 309-329.
38. K.M. Carling and E.A. Carter, Effects of Segregating Elements on the Adhesive Strength and Structure of the α-Al_2O_3/β-NiAl Interface, *Acta Materialia* 55 (2007) 2791-2803.
39. E. Schumman, J.C. Yang, M. Ruhle and M.J. Graham, High Resolution SIMS and Analytical TEM Evaluation of Alumina Scales on a NiAl containing Zirconium or Yttrium, *Oxidation of Metals* 46 (1996) 37-49.

40. T. A. Ramanarayanan, M. Raghavan and R. Petkovic-Luton, Metallic Yttrium Additions to High Temperature Alloys: Influence on Al_2O_3 Scale Properties, *Oxidation of Metals* 22 (1984) 83-100.
41. B. Pint, Experimental Observations in Support of the Dynamic-Segregation Theory to Explain the Reactive-Element Effect, *Oxidation of Metals* 45 (1996) 1-37.
42. F.R. Feret, D. Roy and C. Boulanger, Determination of Alpha and Beta Alumina in Ceramic Alumina by X-Ray Diffraction, *Spectrochimica Acta* Part B55 (2000) 1051-1061.
43. M. O'Keeffe and B.G. Hyde, *Crystal Structures I. Patterns and Symmetry*, Mineralogical Society of America Monograph, BookCrafters Inc. (1996) p.453.
44. F.H. Stott and G.C. Wood, Growth and Adhesion of Oxide Scales on Al_2O_3-Forming Alloys and Coatings, *Materials Science and Engineering* A87 (1987) 267-274.
45. S.H. Cai, S.N. Rashkeev, S.T. Pantelides and K. Sohlberg, Phase Transformation Mechanism between γ- and θ-Alumina, *Physical Review* B67 (2003) 1-10.
46. H.J. Grabke, M.W. Brumm and B. Wagermann, The Oxidation of NiAl, *Materials and Corrosion* 47 (1996) 675-677.
47. G.F. Chen and H.Y. Lou, Predicting the Oxide Formation of Ni-Cr-Al Alloys with Nano-Sized Grain, *Materials Letters* 45 (2000) 286-291.
48. P. Perez, J.L. Gonzalez-Carrasco and P. Adeva, Oxidation Behaviour of a Ni_3Al PM Alloy, *Oxidation of Metals* 48 (1997) 143-170.
49. F. Qin, C. Jiang, J.W. Anderegg, C.J. Jenks, B. Gleeson, D.J. Sordelet and P.A. Thiel, Segregation of Pt at Clean Surfaces of $(Pt,Ni)_3Al$, *Surface Science* 601 (2007) 376-380.
50. C. Jiang and B. Gleeson, Surface Segregation of Pt in γ′-Ni_3Al: A First Principles Study, *Acta Materialia* 55 (2007) 1641-1647.
51. D.R. Lide, *Handbook of Chemistry and Physics*, 73rd Edn, CRC Press, Cleveland, Ohio, USA, (1992-1993).
52. W. Gao, Z. Li, Z. Wu, S. Li and Y. He, Oxidation Behaviour of Ni_3Al and FeAl Intermetallics under Low Oxygen Partial Pressures, *Intermetallics* 10 (2002) 263-270.
53. R. Franchy, J. Masuch and P. Gassman, The Oxidation of the NiAl(111) Surface, *Applied Surface Science* 93 (1996) 317-327.

54. J. Doychak, J.L. Smialek and T.E. Mitchell, Transient Oxidation of Single-Crystal β-NiAl, *Metallurgical Transactions* 20 (1989) 499-518.
55. J.D. Kuenzly and D.L. Douglas, The Oxidation Mechanism of Ni_3Al containing Yttrium, *Oxidation of Metals* 8 (1974) 139-178.
56. E. Schumman and M. Rühle, Microstructural Observation on the Oxidation of γ′-Ni_3Al at High Oxygen Partial Pressure, *Acta Metallurgica et Materialia* 42 (1994) 1481-1487.
57. G.C. Rybicki and J.L. Smialek, Effect of the θ - α-Al_2O_3 Transformation on the Oxidation Behaviour of β-NiAl+Zr, *Oxidation of Metals* 31 (1989) 275-304.
58. H.K.D.H. Bhadeshia, *Nickel Based Superalloys*, University of Cambridge, UK (2003), http://www.msm.cam.ac.uk/phase-tran/2003/Superalloys.html.
59. H.K.D.H. Bhadeshia, *1st, 2nd and 3rd Generation Single-Crystal Nickel Based Superalloys*, University of Cambridge (2008) file://E:\1st, 2nd and 3rd Generation.htm.
60. B. Pieraggi and F. Dabosi, High-Temperature Oxidation of a Single Crystal Ni-Base Superalloy, *Werkstoffe and Korrosion* 38 (1987) 584-590.
61. F. Gesmundo and F. Viani, Transition from Internal to External Oxidation for Binary Alloys in the Presence of an Outer Scale, *Oxidation of Metals* 25 (1986) 269-282.
62. J.L. Meijering, *Advances in Materials Research*, 5th Edn, H. Herman, Ed, Wiley-Interscience, New York (1971) p. 235.
63. S. Han and D.J. Young, Simultaneous Internal Oxidation and Nitridation of Ni-Cr-Al Alloys, *Oxidation of Metals* 55 (2001) 223-242.
64. I.M. Edmonds, H.E. Evans, C.N. Jones and R.W. Broomfield, Intermediate Temperature Internal Oxidation in Fourth Generation Ru-Bearing Single-Crystal Ni-Base Superalloys, *Oxidation of Metals* 69 (2008) 95-108.
65. J.C. Yang, E. Schumman, I. Levin and M. Ruhle, Transient Oxidation of NiAl, *Acta Materialia* 46 (1998) 2195-2201.
66. M. Haerig and S. Hofman, Mechanisms of Ni_3Al Oxidation between 500°C and 700°C, *Applied Surface Science* 125 (1998) 99-114.
67. C. Wagner, Reaktionstypen bei der Oxydation von Legierungen, *Z. Elektrochem* 63 (1959) 772-790.
68. H.-J. Christ, S.-Y. Chang and U. Krupp, Thermodynamic Characteristics and Numerical Modeling of Internal Nitridation of Nickel Base Alloys, *Materials and Corrosion* 54 (2003) 887-894.

69. U. Krupp and H.-J. Christ, Internal Nitridation of Nickel-Base Alloys. Part II. Behaviour of Quaternary Ni-Cr-Al-Ti Alloys and Computer-Based Description, *Oxidation of Metals* 52 (1999) 299-320.
70. U. Krupp and H.-J. Christ, Internal Nitridation of Nickel-Base Alloys. Part I. Behaviour of Binary and Ternary Alloys of the Ni-Cr-Al-Ti System, *Oxidation of Metals* 52 (1999) 277-298.
71. S.J. Wilson, Phase Transformations and Development of Microstructure in Boehmite-Derived Transition Aluminas, *Proceedings of the British Ceramic Society* 28 (1979) p.281.
72. J.W.S. Hearle, J.T. Sparrow and P.M. Cross, *The Use of the Scanning Electron Microscope*, Pergamon Press, Oxford, UK (1972) p. 278.
73. M.T. Postek, K. Howard, A.H. Johnson and K.L. McMichael, *Scanning Electron Microscopy: A Students Handbook*, Ladd Research Industries, Inc., USA (1980) (a) p. 305.
74. D.B. Wittry, Proceedings of the 4th International Conference on X-ray Optics and Microanalysis, Ed. R. Castaing, P. Deschamps and J Philibert, Hermann, Paris (1966) p.168.
75. K.F.J. Heinrich, Proceedings of the 4th International Conference on X-ray Optics and Microanalysis, ed. R. Castaing, P. Deschamps and J Philibert, Hermann, Paris (1966) p.159.
76. J.I. Goldstein, D.E. Newbury, P. Echlin, D.C. Joy, A.D. Romig, Jr., C.E. Lyman, C. Fiori and E. Lifshin, *Scanning Electron Microscopy and Microanalysis*, 2nd Edn. Plenum Press, New York (1992) (a) p.819.
77. J L. Reimer, *Transmission Electron Microscopy*, Springer Series in Optical Series, vol. 36, Ed. P.W. Hawkes, 3rd Edn. Springer-Verlag, Berlin (1993) p. 115.
78. P.E. Champness, *Electron Diffraction in the Transmission Electron Microscope*, Bios Scientific Publishers Ltd, UK (2001) p. 184.
79. B.E.P. Beeston, R.W. Horne and R. Markham, *Practical Methods in Electron Microscopy, Part II. Electron Diffraction and Optical Diffraction Techniques*, Ed. A.M. Glauert, North-Holland Publishing Company, Amsterdam (1972) p.224.
80. S. Mogck, *Transmission Electron Microscopy Studies of Interfaces in Multi-Component Systems*, PhD Thesis, Rijksuniversiteit Groningen (2004) p. 131.
81. L.A. Bendersky and F.W. Gayle, Electron Diffraction using Transmission Electron Microscopy, *Journal of Research of the National Institute of Standards and Technology*, 106 (2001) 997-1012.

82. D.B. Williams, *Transmission Electron Microscopy: A Textbook for Materials Science*, Plenum Press, New York (1996) p. 729.
83. D.C. Joy, A.D. Romig Jr and J.I. Goldstein, *Principles of Analytical Electron Microscopy*, Plenum Press, New York (1986) p. 448.
84. B. Reznik and S. Kalhőfer, Cross-Section Preparation for Transmission Electron Microscopy of Phases and Interfaces in C/BN Heterostructures, *Micron* 33 (2002) 105-109.
85. B. Fultz and J.M. Howe, *Transmission Electron Microscopy and Diffractometry of Materials*, Springer, Berlin (2008) (a) p. 758.
86. R.D. Tarey, R.S. Rastogi and K.L. Chopra, Characterization of Thin Films by Grazing Incidence X-Ray Diffraction, *The Rigaku Journal* 4 (1987) 11-15.
87. A. Strecker, U. Salberger and J. Mayer, Specimen Preparation for Transmission Electron Microscopy: Reliable Method for Cross-Sections and Brittle Materials, *Praktikal Metallography* 30 (1993) 482-495.
88. A. Strecker, J. Mayer, B. Baretzky, E. Eigenthaler, Th. Gemming, R. Schweinfest and M. Ruhle, Optimization of TEM Specimen Preparation by Double-Sided Ion Beam Thinning under Low Angles, *Journal of Electron Microscopy* 48 (1999) 235-244.
89. Y. Liu, R. Wang, X. Guo and J. Dai, A Cross-Sectional TEM Sample Preparation Method for Films Deposited on Metallic Substrates, *Materials Characterization* 58 (2007) 666-669.
90. J.M. Zuo and J.C. Mabon, Web-Based Electron Microscopy Application Software: Web-EMAPS, *Microscopy and Microanalysis* 10 (Supplement 2) (2004). URL: http://emaps.mrl.uiuc.edu/.
91. L. Yang and R.B. McLellan, An Observation of Structural Transformation in Hydrogenated Ni_3Al, *Acta Materialia* 4 (1996) 621-624.
92. G. Renaud, Oxide Surfaces and Metal/Oxide Interfaces Studied by Grazing Incidence X-Ray Scattering, *Surface Science Reports* 32 (1998) 1-90.
93. J.T. Richardson, R. Scates and M.V. Twigg, X-Ray Diffraction Study of Nickel Oxide Reduction by Hydrogen, *Applied Catalysis A: General* 246 (2003) 137-150.
94. A. Babier, G. Renaud and O. Robach, Growth, Annealing and Oxidation of the Ni/MgO (001) Interface studied by Grazing Incidence X-Ray Scattering, *Journal of Applied Physics* 84 (1998) 4259-4267.

95. R.F. Wilde and N.J. Grant, Aging in Complex Commercial Ni-Cr Alloy Hardened with Titanium and Aluminum, *Journal of Metals* 9 (1957) 865-873.
96. T.J. Nijdam, N.M. van der Pers and W.G. Sloof, Oxide Phase Development upon High Temperature Oxidation of γ-NiCrAl Alloys, *Materials and Corrosion* 57 (2006) 269-275.
97. http://www.fiz-karlsruhe.de/icsd
98. R.W.G. Wycoff, *Crystal Structures*, 2nd edn., vol 1 and 2, Interscience, New York, USA (1963).
99. J.X. Dong, K. Sawada, K. Yokokawa and F. Abe, Internal Nitridation Behaviour during Long-Term Creep in a Nickel-Base Superalloy, *Scripta Materialia* 44 (2001) 2641-2646.
100. K. Pruessner and H. Harada, Microstructural Observations on Oxidized Ni-based Superalloy TMS-75 and PGM-Doped Derivatives, *Journal of the Electrochemical Society*, 157 (2010) 95-98.
101. S. Han and D.J. Young, Oxidation – Nitridation of Ni-Cr-Al Alloys, *Materials Research* 7 (2004) 11-16.
102. S.Y. Chang, PhD thesis, University of Siegen, Germany (2001).
103. J.X. Dong, K Sawada, K. Yokokawa and F. Abe, Internal Nitridation Behaviour in Long-Term Creep in a Nickel-Base Superalloy, *Scripta Materialia*, 44 (2001) 2641-2646.
104. H.J. Grabke and E.M. Petersen, Diffusivity of Nitrogen in Iron-Nickel Alloys, *Scripta Metallurgica*, 12 (1978) 1111-1114.
105. J. Takada, S. Uamamoto, S. Kikuchi and M. Adachi, Determination of Diffusion Coefficient of Oxygen in Gamma-Iron from Measurements of Internal Oxidation in Fe-Al alloys. *Metallurgical Transactions* A 17 (1986) 221-229.
106. K. Kawagishi, H. Harada, A. Sato, A. Sato and T. Kobayashi, The Oxidation Properties of Fourth Generation Single-Crystal Nickel-Based Superalloys, *Journal of Metals*, 58 (2006) 43-46.
107. A. Sato, H. Harada, T. Yokokawa, T. Murakumo, Y. Koizumi, T. Kobayashi and H. Imai, The Effects of Ruthenium on the Phase Stability of Fourth Generation Ni-Base Single Crystal Superalloys, *Scripta Materialia*, 54 (2006) 1679-1684.
108. A.C. Yeh and S. Tin, Effects of Ru and Re Additions on the High Temperature Flow Stresses of Ni-Base Single Crystal Superalloys, *Scripta Materialia*, 52 (2005) 519-524.

109. B.A. Pint, K.L. More and I.G. Wright, The Use of Two Reactive Elements to Optimize Oxidation Performance of Alumina-Forming Alloys, *Materials at High Temperatures*, 20 (2003) 375-386.
110. K. Pruessner, P.Y. Hou, B.A. Pint, K.B. Alexander and P.F. Tortorelli, Engineering the Interfacial Chemistry in Metal/Oxide Systems, in Interfacial Engineering for Optimized Properties II, *MRS Proceedings*, Materials Research Society, 586 (2000) 133-138.
111. B.A. Pint, K.L. More and I.G. Wright, The Use of Reactive Elements to Optimize Oxidation Performance of Alumina Forming Alloys, *Materials at High Temperatures* 20 (2003) 375-386.
112. B.D. Cullity, *Elements of X-ray Diffraction*, Addison-Wesley Publishing Company Inc., Reading, Mass., USA (1967).

Appendices

Appendix A: Conference abstract published during the course of this project

54TH ANNUAL CONFERENCE OF THE SOUTH AFRICAN INSTITUTE OF PHYSICS

Scientific Programme: 7 – 10 July 2009

Including the Winter Schools on

"Southern Skies"

and

"Quantum Information Processing and Communication"

6 July 2009

Hosted by

UNIVERSITY OF KWAZULU-NATAL

School of Physics

University of KwaZulu-Natal

[4]Effect of Preparation on the Surface Quality of Ni-Based and Pt-Based Superalloys

O.M. Bill[1,2,3], J.K. Odusote[1,2,3], K. Pruessner[1,2,3]

[1]*School of Physics,* [2]*DST/NRF Centre of Excellence in Strong Materials (CoE-SM) and* [3]*Materials Physics Research Institute (MPRI),*
University of the Witwatersrand, Wits 2050, Johannesburg, South Africa.

Ni-based superalloys are used in the hot section of turbines. Critical properties are mechanical properties and environmental stability at high temperatures. Turbine efficiency could be improved by increasing the operating temperature. Since currently used materials have reached their temperature limit, new alloys have to be developed. One approach is to develop Pt-based analogues with microstructures similar to Ni-based superalloys [1]. Another approach is to alloy Ni-based superalloys with platinum-group metals [2]. In order to study the high-temperature oxidation resistance of these alloys, high quality surfaces need to be prepared. We have examined the effect of different polishing treatments on the surface quality of Ni-based superalloys CMSX-4 and TMS-75 and a novel Pt-based superalloy ($Pt_{84}Al_{11}Cr_3Ru_2$).

For the Ni-based superalloys, samples of 1 mm thickness were cut from single-crystal metal rods using a diamond wafering blade on a slow-speed saw. Samples of Pt-based alloys were cut from a polycrystalline ingot using EDM. All samples were subsequently ground manually using 600, 1000 and 1200 grade SiC paper on a rotating disk. Surface polishing was performed manually on a Mastertex polishing cloth from Buehler using 6µm, 3µm, 1µm and 0.25µm diamond paste and Metadi polishing fluid for lubrication. Pt-based samples received a surface finish using OPS. Alloy surfaces were characterized after the 1µm, 0.25µm and OPS polishing steps using optical microscopy, Scanning Electron Microscopy and Atomic Force Microscopy. It could be shown that for Ni-based superalloy TMS-75, surface roughness decreased from 50 nm for the 1µm diamond paste to 3 nm for the 0.25µm diamond paste. Improved surface smoothness with fewer scratches was observed on Pt-based alloy after polishing with 0.25µm diamond paste, with little or no improvement with the use of OPS. The presence of deeper scratches on the surfaces became more prominent after using 0.25µm and OPS though.

[1] L.A. Comish, B. Fischer, R. Völkl (2003), MRS Bulletin 9, 632.
[2] T. Kobayashi, Y. Koizumi, S. Nakazawa, T. Yamagata, H. Harada (1997), in: Proc. Fourth Int. Charles Parsons Turbine Conf., The Inst. of Materials, 766.

[163]Surface Brillouin and Raman scattering study of boron-doped epitaxial polysilicon films.

B.A. Mathe[1,2], J.D. Comins[1,2],

[1] Materials Physics Research Institute, University of the Witwatersrand
[2]DST/Centre of Excellence in Strong Materials, University of the Witwatersrand

Polycrystalline silicon is common in micro-electro-mechanical systems (MEMS) and integrated circuits. The rapidly growing application of thin polysilicon films in MEMS requires an accurate evaluation of mechanical properties by means of equally micro-mechanical or optical testing techniques due to the scales involved. Surface Brillouin Scattering (SBS) offers the possibility to determine the Young's modulus for the polysilicon films without need for making assumptions regarding the Poisson's ratio, and the recent advances in high temperature SBS make it feasible to measure variation of the elastic constants with temperature. In this study Raman spectroscopy was also used to investigate the effect of different thermal annealing cycles on the average intrinsic stress of the boron-doped polysilicon film, study thermally induced boron activation effects on the strength of the material and correlate this behaviour with the SBS results of Young's modulus, E and bulk modulus, B measured at equivalent temperatures. Previously, Raman scattering studies have been conducted for similar dopant concentrations (10^{18} - 10^{19} cm^3) in thin Si membranes doped with Sb or B, where it was shown that the Fano-dip due to an optical phonon disappears in the spectrum when the holes are missing in the acceptor sites either by an increase of the sample temperature or by doping compensation. This observation was confirmed in this experiment at about 510°C; however, the unexpected full recovery of the Fano-line asymmetry on cooling down after the annealing process draws attention to the role of the boron which will be discussed in this work in order to explain the steep increase in moduli observed.

[302]Valence reduction of V_2O_5 sol-gel to form VO_2 Nano-structures

H. M. Cele[1, 2], M. Maaza[1], O.M. Ndwandwe[2], and J.B. Kana Kana[1]

[1]*Nanoscience and Nanotechnology Laboratory, Material Research Group, iThemba LABS,P.O. Box 722, Somerset West, 7129, South Africa.*
[2] *Department of Physics & Engineering, University of Zululand, P/Bag X1001, KwaDlangezwa, 3886, South Africa*

In this work, the V_2O_5 sol-gel was used as a precursor for producing thermochromic vanadium dioxide (VO_2) thin films. In order for V_2O_5 film deposition, the normal glass and silicon (111) substrates were ultrasonically cleaned. The method used in film synthesis is soft chemistry, which is well-known as *valence reduction method.* During valence reduction, vanadium (V) oxide forms different vanadium oxides before vanadium (IV) oxide such as: V_2O_5; V_3O_7; V_4O_9; V_6O_{13}; VO_2 [1]. The two gases 10% *hydrogen (H_2)* mixed with 90% of argon (Ar) [2]; 50% *carbon monoxide (CO)* mixed with 50% of carbon dioxide (CO_2) were used for valence reduction of V_2O_5 film [3].

The produced V_2O_5 films were studied under atomic force microscope (AFM) and scanning electron microscope (SEM) techniques to see the surface morphology and compare roughness, the changes of the pure V_2O_5 crystals with VO_2 crystals. The optical properties were characterized using FTIR and UV-Visible.

[1] Y. Ningyi, L. Jinhua, L. Chenglu: *Valence reduction process from sol-gel V_2O_5 to VO_2 thin films.* 191 (2002) 176-18

[2] V. Keppens, D. Mandrus, L.A. Boatner. *Chemical and Sonochemical Approaches to the formation of VO_2 and VO_2-impregnated materials. xxx* (1997) 1-9

[3] A. Block-Bolten, J. M. Bertrand, S. N. Flengas. *Oxidation of CO to CO_2 in Melts Containing V_2O_5 and Alkali Oxides.* 52 (1974) 2068

Appendix B: Formulae for calculation of the *d* spacings of different structures [112]

Cubic structure: $$\frac{1}{d^2} = \frac{h^2 + k^2 + l^2}{a^2}$$

Tetragonal structure: $$\frac{1}{d^2} = \frac{h^2 + k^2}{a^2} + \frac{l^2}{c^2}$$

Hexagonal structure: $$\frac{1}{d^2} = \frac{4}{3}\left(\frac{h^2 + hk + k^2}{a^2}\right) + \frac{l^2}{c^2}$$

Rhombohedral structure:

$$\frac{1}{d^2} = \frac{\left(h^2 + k^2 + l^2\right)\sin^2\alpha + 2\left(hk + kl + hl\right)\left(\cos^2\alpha - \cos\alpha\right)}{a^2\left(1 - 3\cos^2\alpha + 2\cos^3\alpha\right)}$$

Monoclinic structure: $$\frac{1}{d^2} = \frac{1}{\sin^2\beta}\left(\frac{h^2}{a^2} + \frac{k^2\sin^2\beta}{b^2} + \frac{l^2}{c^2} - \frac{2hl\cos\beta}{ac}\right)$$

Appendix C: Formulae for calculation of the angle ϕ between the plane ($h_1k_1l_1$), of spacing d_1 and the plane ($h_2k_2l_2$), of spacing d_2 for the different structures, as well as the zone axis formula [112]

Cubic:
$$\cos\phi = \frac{h_1h_2 + k_1k_2 + l_1l_2}{\sqrt{\left(h_1^2 + k_1^2 + l_1^2\right)\left(h_2^2 + k_2^2 + l_2^2\right)}}$$

Tetragonal:
$$\cos\phi = \frac{\dfrac{h_1h_2 + k_1k_2}{a^2} + \dfrac{l_1l_2}{c^2}}{\sqrt{\left(\dfrac{h_1^2 + k_1^2}{a^2} + \dfrac{l_1^2}{c^2}\right)\left(\dfrac{h_2^2 + k_2^2}{a^2} + \dfrac{l_2^2}{c^2}\right)}}$$

Hexagonal:
$$\cos\phi = \frac{h_1h_2 + k_1k_2 + \dfrac{1}{2}\left(h_1k_2 + h_2k_1\right) + \dfrac{3a^2}{4c^2}l_1l_2}{\sqrt{\left(h_1^2 + k_1^2 + h_1k_1 + \dfrac{3a^2}{4c^2}l_1^2\right)\left(h_2^2 + k_2^2 + h_2k_2 + \dfrac{3a^2}{4c^2}l_2^2\right)}}$$

Rhombohedral:
$$\cos\phi = \frac{a^4d_1d_2}{V^2}\left[\begin{array}{l}\sin^2\alpha\left(h_1h_2 + k_1k_2 + l_1l_2\right) \\ + \left(\cos^2\alpha - \cos\alpha\right)\left(k_1l_2 + k_2l_1 + l_1h_2 + l_2h_1 + h_1k_2 + h_2k_1\right)\end{array}\right]$$

where $V = a^3\sqrt{1 - 3\cos^2\alpha + 2\cos^3\alpha}$

Monoclinic:
$$\cos\phi = \frac{d_1d_2}{\sin^2\beta}\left[\frac{h_1h_2}{a^2} + \frac{k_1k_2\sin^2\beta}{b^2} + \frac{l_1l_2}{c^2} - \frac{\left(l_1h_2 + l_2h_1\right)\cos\beta}{ac}\right]$$

Points h_1, k_1, l_1 and h_2, k_2, l_2 will lie on the reciprocal lattice plane (uvw) given by

$$(uvw) \equiv \left(\begin{vmatrix} k_1 & l_1 \\ k_2 & l_2 \end{vmatrix}, \begin{vmatrix} l_1 & h_1 \\ l_2 & h_2 \end{vmatrix}, \begin{vmatrix} h_1 & k_1 \\ h_2 & k_2 \end{vmatrix}\right)$$

$$= \left(k_1l_2 - l_1k_2, l_1h_2 - h_1l_2, h_1k_2 - k_1h_2\right)$$

This gives the crystal direction or zone axis [uvw] which is parallel to the electron beam.

Appendix D: Simulated diffraction patterns from the WebEMAPS software package [90].

Please note, for the hexagonal, monoclinic and rhombohedral structures the simulation software gives the only the *hkl* values. For *hkil* values, $i = -(h+k)$.

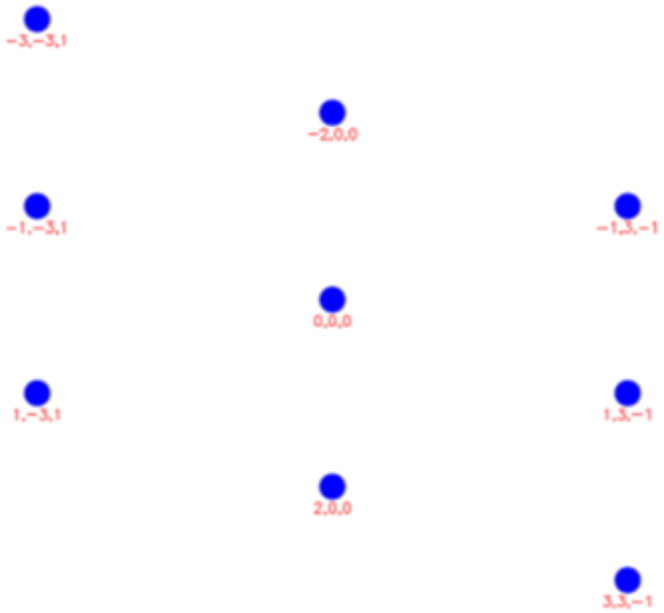


Figure D1: Ni – solid solution and Ni – based solid solution (face centred cubic) [013]

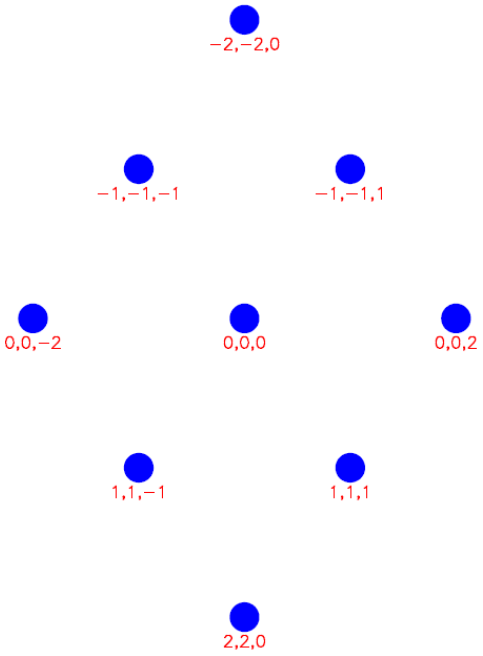


Figure D2: Ni – solid solution and Ni – based solid solution (face centred cubic) [$\bar{1}10$]

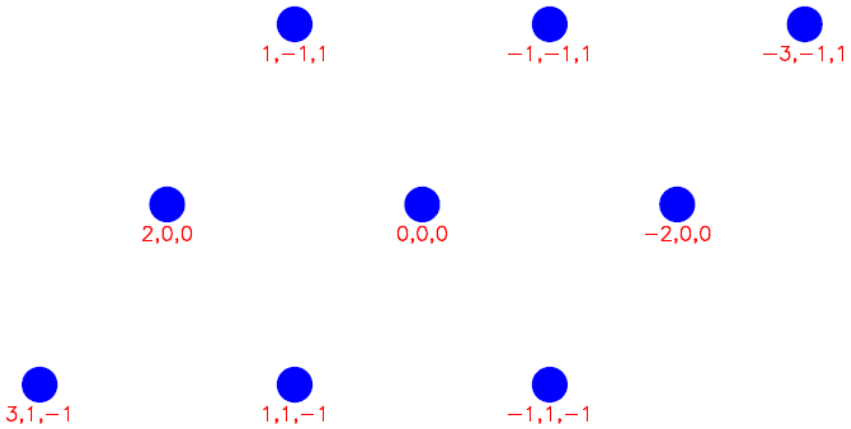


Figure D3: Ni – solid solution and Ni – based solid solution (face centred cubic) [$1\bar{1}4$]

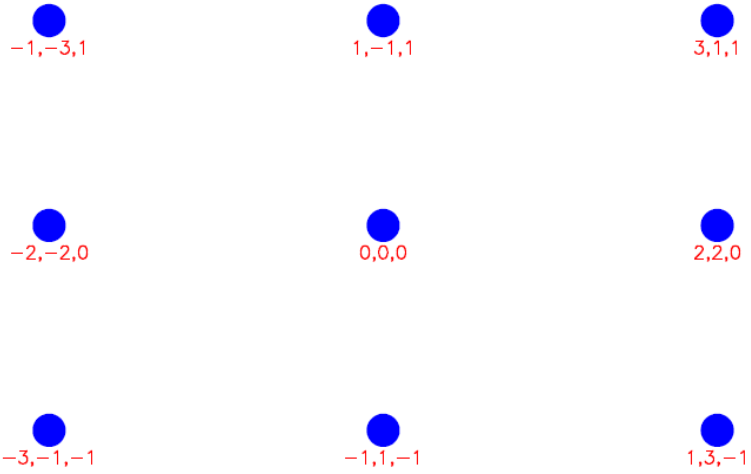


Figure D4: Ni – solid solution and Ni – based solid solution (face centred cubic) [$1\bar{1}\bar{2}$]

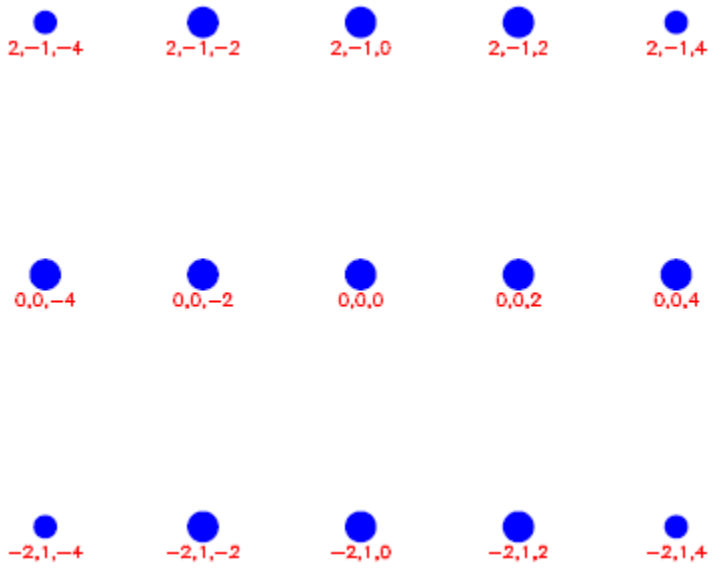


Figure D5: AlN (hexagonal) [$12\bar{3}0$]

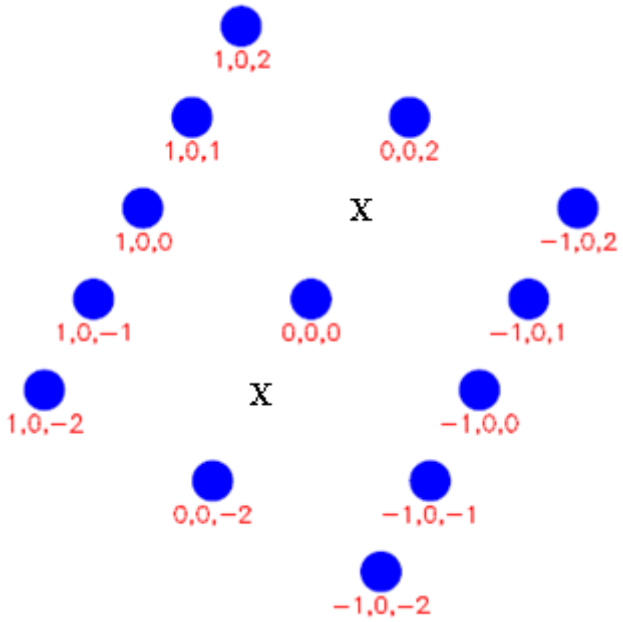


Figure D6: AlN (hexagonal) [$01\bar{1}0$]. The crosses indicate the positions of reflections forbidden by the structure factor, but occurring in the pattern by double diffraction.

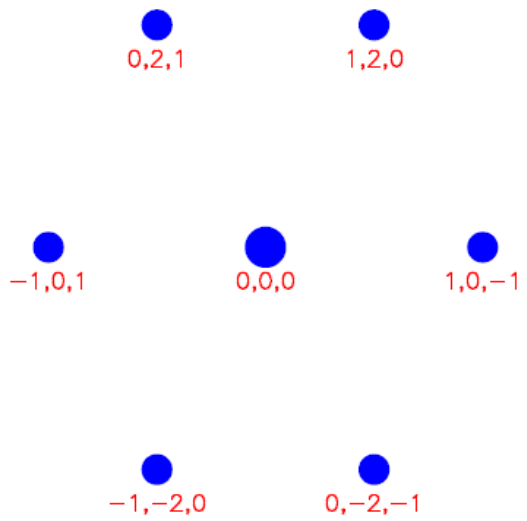


Figure D7: α-Al_2O_3 (rhombohedral) [$2\bar{1}\bar{1}2$]

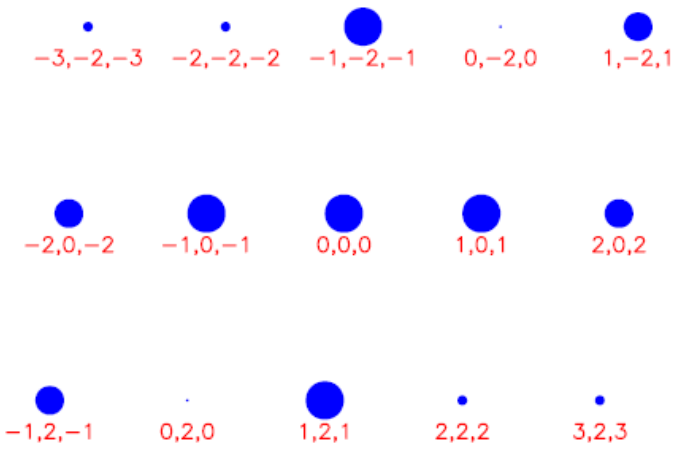


Figure D8: α-Al_2O_3 (rhombohedral) [$10\bar{1}\bar{1}$].